UNIVERSIDADE ESTADUAL DE CAMPINAS
Faculdade de Engenharia Elétrica e de Computação

Jaime Junior Luque Quispe

# Pulse shaping of OFDM-based waveforms for the 5G air interface

# Conformação de pulso de formas de onda OFDM para a interface aérea 5G

**Campinas**

**2016**

UNIVERSIDADE ESTADUAL DE CAMPINAS
Faculdade de Engenharia Elétrica e de Computação

Jaime Junior Luque Quispe

# Pulse shaping of OFDM-based waveforms for the 5G air interface
# Conformação de pulso de formas de onda OFDM para a interface aérea 5G

Dissertação apresentada à Faculdade de Engenharia Elétrica e de Computação da Universidade Estadual de Campinas como parte dos requisitos exigidos para a obtenção do título de Mestre em Engenharia Elétrica, na Área de Telecomunicações e Telemática

Supervisor: Prof. Dr. Luís Geraldo Pedroso Meloni

Este exemplar corresponde à versão final da tese defendida pelo aluno Jaime Junior Luque Quispe, e orientada pelo Prof. Dr. Luís Geraldo Pedroso Meloni

Campinas

2016

**Agência(s) de fomento e nº(s) de processo(s):** CAPES, NÃO POSSUI NÚMERO DE PROCESSO
**ORCID:** 0000-0002-4856-3537

Ficha catalográfica
Universidade Estadual de Campinas
Biblioteca da Área de Engenharia e Arquitetura
Luciana Pietrosanto Milla - CRB 8/8129

Luque Quispe, Jaime Junior, 1987-
L974p Pulse shaping of OFDM-based waveforms for the 5G air interface / Jaime Junior Luque Quispe. – Campinas, SP : [s.n.], 2016.

Orientador: Luís Geraldo Pedroso Meloni.
Dissertação (mestrado) – Universidade Estadual de Campinas, Faculdade de Engenharia Elétrica e de Computação.

1. OFDM. 2. Filtros digitais. 3. Comunicações móveis. 4. Modulação digital. 5. Processamento digital de sinais. I. Meloni, Luís Geraldo Pedroso, 1958-. II. Universidade Estadual de Campinas. Faculdade de Engenharia Elétrica e de Computação. III. Título.

Informações para Biblioteca Digital

**Título em outro idioma:** Conformação de pulso de formas de onda OFDM para a interface aérea 5G
**Palavras-chave em inglês:**
OFDM
Digital filters
Mobile communications
Digital modulation
Digital signal processing
**Área de concentração:** Telecomunicações e Telemática
**Titulação:** Mestre em Engenharia Elétrica
**Banca examinadora:**
Luís Geraldo Pedroso Meloni [Orientador]
Cristiano Akamine
Renato da Rocha Lopes
**Data de defesa:** 19-08-2016
**Programa de Pós-Graduação:** Engenharia Elétrica

**COMISSÃO JULGADORA - DISSERTAÇÃO DE MESTRADO**

**Candidato**: Jaime Junior Luque Quispe RA: 144411

**Data da Defesa**: 19 de agosto de 2016

**Título da Tese**: "Pulse shaping of OFDM-based waveforms for the 5G air interface (Conformação de Pulso de Formas de Onda OFDM para a Interface Aérea 5G)"

Prof. Dr. Luís Geraldo Pedroso Meloni (Presidente, FEEC/UNICAMP)
Prof. Dr. Cristiano Akamine (Universidade Presbiteriana Mackenzie)
Prof. Dr. Renato da Rocha Lopes (FEEC/UNICAMP)

A ata da defesa, com as respectivas assinaturas dos membros da Comissão Julgadora, encontra-se no processo de vida acadêmica do aluno.

*To my parents Jaime Luque Arapa and Marcelina Quispe Condori,*
*and in loving memory of my grandmother Agustina Arapa,*
*to whom I owe everything.*

# Acknowledgements

I would like to thank my advisor, Prof. Dr. Luís Meloni, for all the support and academic guidance that he has extended to me throughout this thesis. He always gave me useful suggestions and has taught me how to carry out research during my time at the Real-Time Digital Signal Processing (RT-DSP) research laboratory at UNICAMP. I also had the opportunity to work with him in a research project on the design of a digital up-down converter which was supported by El Dorado Research Institute. Working with Dr. Meloni helped sharpen my thinking and he has been an example and continuous source of encouragement to me.

To the Coordination for the Improvement of Higher Education Personnel (CAPES) for supporting this work.

To my preliminary examiners, Prof. Dr. Yuzo Iano and Prof. Dr. Paulo Cardieri. Their rigorous feedback has greatly improved the structure of this manuscript.

To my committee members Prof. Dr. Cristiano Akamine and Prof. Dr. Renato Lopes, for agreeing to review this work and provide me valuable feedback and new ideas for my research.

To the professors of the Department of Communications (DECOM) of the School of Electrical and Computer Engineering, especially Prof. Dr. Max Costa, Prof. Dr. José Cândido, Prof. Dr. Renato Lopes and Prof. Dr. Celso Almeida who added valuable knowledge on wireless communications, information theory and digital signal processing to my professional background. It was a privilege to learn from them.

My gratitude also goes to my colleagues, especially to Fernando Moura, Dick Carrillo, Henry Merino, José Hinostroza, Jackelyn Tume and Daniel Tavares, for the stimulating discussions and friendship.

# Abstract

Orthogonal frequency division multiplexing (OFDM) waveforms have been used successfully in the 3GPP Long Term Evolution (LTE) air interface to overcome the channel selectivity and to provide good spectrum efficiency and high transmission data rates. The forthcoming 5G communication system aims to support more services than its predecessor, such as enhanced mobile broadband, machine-type communications and low latency communications, and considers many other application scenarios such as the fragmented spectrum use. This diversity of services with different requirements cannot be supported by conventional OFDM since OFDM configures the entire bandwidth with parameters attending one service in particular. Also, substantial intercarrier interference (ICI) can occur when conventional OFDM is used with asynchronous multiuser multiplexing and this is due to the high out-of-band (OOB) emissions of the subcarriers and the violation of the signal orthogonality constraint. Therefore, to meet the requirements of future 5G wireless applications, the development of an innovative air interface with new capabilities becomes necessary, in particular, a new waveform more spectrally agile than OFDM capable of supporting multiple configurations, suppressing the inter-user interference effectively, and with straightforward integration with the upper layers.

This work focuses on two pulse shaping techniques to reduce the OOB emission and improve the in-band and OOB performances of OFDM-based waveforms. Pulse shaping can enable the use of multiple parameterizations within the waveform and abandon the strict paradigms of orthogonality and synchronism with relatively low performance degradation caused by intersymbol interference (ISI) and ICI.

The first part addresses a pulse shaping method based on per-subcarrier filtering to reduce both OOB emission in the transmitter and adjacent channel interference (ACI) in the receiver. It can be implemented using window functions and some window formats are presented in this part. The first uses the existing cyclic prefix (CP) of OFDM symbols to smooth abrupt transitions of the signal, thus the large *sinc* spectral sidelobes caused by the rectangular filters. This guarantees backwards compatibility in systems using conventional cyclic prefixed OFDM (CP-OFDM). The second window format extends the CP length to retain the waveform ability to combat channel delay spread. The effects on performance of ISI and ICI are studied in terms of the signal to interference ratio (SIR) and bit error rate (BER) using LTE waveforms in a multi-user fragmented spectrum scenario.

The second part of this work addresses the design and analysis of a filters for flexible spectral containment in subband-based filtering transceivers. This filter, called here semi-equiripple, exhibits better stopband attenuation to reduce the inter-subband interferences than equiripple and windowed truncated *sinc* filters and also has good impulse response characteristics to reduce ISI. The design is based on the Parks-McClellan algorithm to

obtain different stopband decay rates and meet arbitrary spectrum emission masks (SEM) specifications with low in-band distortion. Therefore, it can be useful to achieve low OOB emission and configure subbands with independent parameters since the asynchronous interference is contained by the filters. Three ISI distortions in the filter are studied: symbol spreading related to the filter causality, symbol echoes due to in-band ripples, and ISI amplification due to outlier samples in the tails of its impulse response. The performance of the filter is assessed in terms of the power spectrum density (PSD) and compliance with tight SEMs, modulation error rate (MER) and operation in a multi-service asynchronous scheme using a single waveform. The SIR and the effect of filtering on the modulation accuracy are evaluated using OFDM ISDB-T and LTE waveforms. Flexible hardware structures are also proposed for actual implementations.

The results show that these pulse shaping methods enable the waveform to exploit the available spectrum fragments and support multiple services without significant performance penalty, which can allow a more flexible air interface.

**Keywords**: OFDM, pulse shaping, digital filters, 5G waveforms, air interface.

# Resumo

As formas de onda com multiplexação ortogonal por divisão de freqüência (OFDM) foram utilizadas com sucesso na interface aérea 3GPP LTE para superar a seletividade do canal e proporcionar uma boa eficiência espectral e altas taxas de transmissão de dados. O próximo sistema de comunicações 5G tem como objetivo oferecer suporte a mais serviços do que o antecessor, como comunicações de banda larga móveis, comunicações de tipo máquina e comunicações de baixa latência, e considera muitos outros cenários de aplicação, como o uso de espectro fragmentado. Esta diversidade de serviços com diferentes requisitos não pode ser suportada pela OFDM convencional, pois OFDM configura toda a largura de banda com parâmetros que atendem a um serviço em particular. Além disso, pode ocorrer interferência interportadora (ICI) quando a OFDM convencional é usada com multiplexação assíncrona de múltiplos usuários e isso é devido às altas emissões fora de banda (OOB) das subportadoras e à violação da condição de ortogonalidade do sinal. Portanto, para atender aos requisitos das futuras aplicações sem fio 5G, o desenvolvimento de uma interface aérea inovadora com novas capacidades torna-se necessário, em particular, uma nova forma de onda mais espectralmente ágil do que OFDM capaz de suportar múltiplas configurações, suprimindo efetivamente a interferência entre usuários, e com integração direta com as camadas superiores.

Este trabalho centra-se em duas técnicas de conformação de pulsos para reduzir a emissões fora de banda e melhorar o desempenho de formas de onda baseadas em OFDM. A conformação de pulsos pode permitir o uso de parametrizações múltiplas dentro da forma de onda e abandonar os paradigmas rígidos de ortogonalidade e sincronismo com uma degradação de desempenho causada por interferência intersymbol (ISI) e ICI relativamente baixa.

A primeira parte aborda um método de modelagem de pulso baseado na filtragem por subportadora para reduzir a emissão fora de banda no transmissor e interferência de canal adjacente (ACI) no receptor. Ele pode ser implementado usando funções de janela e alguns formatos de janela são apresentados nesta parte. O primeiro usa o prefixo cíclico (CP) existente dos símbolos para suavizar as transições abruptas do sinal, portanto, os grandes lóbulos espectrais *sinc* causados pelos filtros retangulares. Isso garante a compatibilidade retroativa em sistemas que usam OFDM com prefixo cíclico (CP-OFDM). O formato da segunda janela estende o comprimento do CP para reter a capacidade da forma de onda para combater a propagação do atraso do canal. Os efeitos no desempenho do ISI e ICI são estudados em termos de relação de sinal para interferência (SIR) e taxa de erro de bit (BER) usando formas de onda LTE em um cenário de espectro fragmentado multi-usuário.

A segunda parte deste trabalho aborda o desenho e análise de filtros para a contenção espectral flexível em transceptores com filtragem baseada em sub-banda. Este filtro, cha-

mado aqui *semi-equiripple*, exibe melhor atenuação na banda de rejeição para reduzir as interferências entre subbandas do que os filtros equiripple e filtros *sinc* baseados em janelamento e também possui boas características de resposta ao impulso para reduzir o ISI. O projeto de filtros baseia-se no algoritmo Parks-McClellan para obter diferentes taxas de decaimento da banda de parada e atende a especificações arbitrárias de máscaras de emissão de espectro (SEM) com baixa distorção dentro da banda. Portanto, pode ser útil para obter baixas emissões fora da banda e configurar sub-bandas com parâmetros independentes, uma vez que a interferência assíncrona é contida pelos filtros. São estudadas três distorções de ISI no filtro: espalhamento de símbolos relacionado à causalidade do filtro, ecos de símbolos devido a ondulações na banda e amplificação de ISI devido a amostras de valores anômalas nas caudas de sua resposta de impulso. O desempenho do filtro é avaliado em termos de densidade de espectro de potência (PSD) e conformidade com SEMs, taxa de erro de modulação (MER) e operação em um esquema assíncrono multi-serviço usando uma única forma de onda. O SIR e o efeito da filtragem na precisão da modulação são avaliados usando formas de onda OFDM ISDB-T e LTE. Estruturas de hardware flexíveis também são propostas para implementações reais.

Os resultados mostram que esses métodos de conformação de pulso permitem que a forma de onda explore os fragmentos de espectro disponíveis e ofereça suporte a múltiplos serviços sem uma penalidade de desempenho significativa, o que pode permitir uma interface aérea mais flexível.

**Palavras-chaves**: OFDM, conformação de pulso, filtros digitais, forma de onda 5G, interface aérea.

# List of Figures

# List of Tables

# Acronyms

3GPP Third generation partnership project

4G Fourth-generation mobile communications system

5G Fifth-generation mobile communications system

ACI Adjacent channel interference

AWGN Additive white Gaussian noise

BER Bit error rate

CFO Carrier frequency offset

CP Cyclic prefix

CP-OFDM Cyclic prefixed OFDM

DFT Discrete Fourier transform

EVA Extended vehicular A

EVM Error vector magnitude

F-OFDM Filtered OFDM

FB-F-OFDM Full-band filtered OFDM

FBMC Filter bank multicarrier

FFT Fast Fourier transform

FPGA Field programmable gate array

GFDM generalized frequency division multiplexing

ICI Intercarrier interference

IFFT Inverse fast Fourier transform

IoT Internet of things

ISBI Inter-subband interference

ISDB-T Integrated Services Digital Broadcasting Terrestrial

ISI Intersymbol interference

LTE Long Term Evolution

MTC Machine-type communications

OFDM Orthogonal frequency division multiplexing

OOB Out-of-band

OOBE Out-of-band emission

PAPR Peak-to-average power ratio

PHY Physical layer

PSD Power spectral density

PSD Power spectrum density

QAM Quadrature amplitude modulation

QPSK Quadrature phase shift keying

RB Resource block

RC Raised cosine

SDR Software-defined radio

SEM Spectrum emission mask

SIR Signal to interference ratio

UFMC Universal filtered multicarrier

V2V Vehicle-to-vehicle

W-OFDM Windowed OFDM

# Contents

# 1 Introduction

## 1.1 Motivation and background

Over the past years, the development of wireless communications technology has been largely influenced by the increasing traffic demand. Nowadays, emergent applications requiring low latency, higher connection density and ubiquitous gigabit connectivity impose new technical requirements which are motivating an intense research work on the components of the forthcoming fifth generation (5G) of mobile communication systems. However, the wide variety of these requirements such as the support for heterogeneous services using a single waveform and flexible spectrum use can not be met by the current LTE air interface. The LTE physical layer (PHY) uses orthogonal frequency division multiplexing (OFDM) to overcome the channel selectivity problem, achieve high data rates and boost the spectrum efficiency, but since LTE OFDM waveforms have been designed with strict orthogonality and synchronism constraints and embedded in a frame structure not able to accommodate different services, a more flexible air interface requires the redesign of the conventional OFDM waveform.

Emerging applications requiring high bit rates (e.g. UHD video) can demand large bandwidths. However, since contiguous spectrum is not always available, the simultaneous access to non-contiguous blocks of unused spectrum or underused ones becomes necessary. The use of OFDM for fragmented spectrum access is not satisfactory because of the potential adjacent channel interference (ACI) arising from the out-of-band (OOB) spectral leakage which in turn is due to the discontinuity between adjacent OFDM symbols. This problem has been addressed by several current systems such as LTE, ISDB-T and IEEE 802.11 by using guard bands to meet spectrum emission mask (SEM) requirements but sacrificing spectrum efficiency (e.g. in LTE the guard band constitutes 10% of the allocated bandwidth). Thus, methods to reduce the out-of-band emission (OOBE) are necessary to use OFDM in new communication scenarios and constitute an important research topic.

The rectangular pulses for subcarrier modulation in conventional OFDM generate undesired spectral *sinc* sidelobes out of the useful bandwidth. Some techniques in the time and frequency domains for OOBE reduction have been studied in several works. One of these techniques is the polynomial cancellation coding [1] which is based on obtaining a better frequency domain representation for OFDM. Each data symbol (e.g. QAM symbol) is represented by a group of symbols which are then multiplied by the coefficients of a polynomial. At the receiver side, the sidelobes of one subcarrier are reduced by the sidelobes of the other subcarriers in the group. Another technique is the cancellation car-

rier method which consists in inserting optimized subcarriers at both sides of the active spectrum such that the sidelobes of the inserted subcarriers and the sidelobes of the signal cancel each other within a desired frequency range [2]. The subcarrier weighting method proposed in [3] is based on the multiplication of the data symbols with real numbers (weights) such that the powers of the sidelobes are minimized. However, the weighting factors are constrained in magnitude to ensure that each data symbol remains within its original decision region so that they can be detected by the receiver without having prior knowledge of the weights. The dynamic deactivation of edge subcarriers offers a flexible way to shape the spectrum [4], however the use of guard bands wastes spectrum frequencies. The cancellation carrier and polynomial cancellation coding methods also suffer this penalty in spectrum efficiency. Another option to reduce the OOBE is filtering, however for a fragmented spectrum scenario, filtering can be expensive to implement since separate filters have to be used for each fragment. Another alternative is to smooth the symbol transitions by windowing the edges of each symbol with an appropriate function [4, 5]. The idea behind this method is to filter each subcarrier to contain the OOBE. A transceiver architecture using digital subcarrier filters was presented in [6]. However, the analysis of the in-band performance when some CP samples are used for windowing has been not analyzed in these works. The characteristics of this per-subcarrier filtered waveform, also known as windowed OFDM (W-OFDM) and the analysis of the trade-offs between the OOB and in-band performances are addressed in Chapter 2.

On the other hand, guaranteeing orthogonality and synchronism in OFDM, and thus avoiding intercarrier interference (ICI), might require significant control signaling, creating severe network congestion. A single configuration applied to the entire OFDM bandwidth in LTE prevents in-band support of different applications simultaneously whether they are synchronous or asynchronous, as for instance, vehicle-to-vehicle (V2V) communications could require not only short frames for low latency but also wider subcarrier spacing for robustness against Doppler shift or a custom CP size should be necessary for service coverage in different cell areas. Thus, in order to multiplex different parameters on the same OFDM waveform, the orthogonality constraint needs to be removed or relaxed.

Several non-orthogonal waveforms have been proposed aiming to retain the advantages of OFDM and to overcome its related drawbacks. These waveforms are based on splitting and filtering the overall bandwidth on either a per-subcarrier basis such as the generalized frequency division multiplexing (GFDM) [7] and filter bank multicarrier (FBMC) [8, 9] waveforms or a per-subband basis such as the universal filtered multicarrier (UFMC) [10] and filtered-OFDM (F-OFDM) [11, 12] waveforms. Filters are key components in these waveforms to reduce the OOBE and, in case of subband-based filtering transceivers, to reduce the inter-subband interference (ISBI) [11, 13, 14]. UFMC is seen as a generalization of the full-band filtered OFDM (FB-F-OFDM) and FBMC modulations. FB-F-OFDM filters the entire band and FBMC filters individual subcarriers, while UFMC filters sub-

bands. Since UFMC is an intermediary case between subcarrier filtering and full-band filtering, it is taken as a reference in this part of the work. UFMC collects the advantages of both schemes while avoiding their disadvantages (e.g. UFMC uses shorter filters lengths in comparison to FBMC and has reduced OOBE than OFDM). Also, UFMC subbands can be allocated to different services which allows UFMC to be a highly adaptive waveform [14].

A block diagram of a subband-based filtering transceiver based on the idea of UFMC is shown in Fig. 1. As can be seen, the available bandwidth can be divided in a number of subbands ($K$), each with a different number of subcarriers and modulation schemes (e.g. QPSK, M-QAM) and some subbands can be deactivated for a given transmission. Then, the complex data symbols of each subband are transformed into time domain signals using inverse fast Fourier transform (IFFT) computations. An arbitrary CP is appended to each subband signal which is then filtered to reduce the spectral sidelobes. All the filtered signals are summed to generate the transmit baseband signal. Each subband can be allocated to a service or user (multiple or single carrier) in particular with arbitrary sets of parameters (e.g. subcarrier spacing, shaping filter, FFT order, CP length). UFMC considers the filter length is in the order of the CP size to prevent ISI, and the same filter Dolph-Chebyshev of constant sidelobe level is used for all the sub-bands [15]. However, short filter lengths can be insufficient to achieve adequate stopband attenuation for low interference between adjacent subbands. In Chapter 3, this work introduces an alternative filter, called semi-equiripple, which exhibits better stopband attenuation for reduction of the ISBI than equiripple and windowed *sinc* filters and also better impulse response characteristics for reduction of the ISI. The results indicate that a filter order greater than the CP size can be employed to improve the spectrum containment and the orthogonality within the subband can be sacrificed with low performance penalties (e.g. low BER degradation and ISI distortion) for the benefit of a reduction of the OOBE. Also, filters with narrow transition regions can reduce the number of guard bands and allow more efficient use of the available bandwidth.

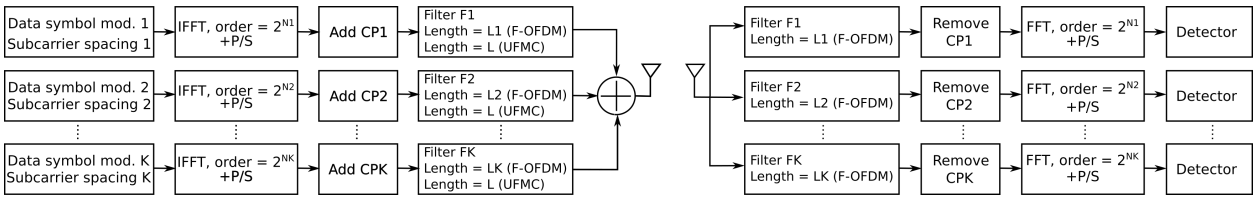


Figure 1 – Block diagram of an enhanced UFMC transceiver

The generation of the waveform and pulse shaping filters can be performed flexibly using software-defined radio (SDR) techniques. From the point of view of hardware implementation, suitable filter architectures for fixed-point realizations are required to minimize the finite word-length effects. These effects are analyzed at the end of Chapter 3.

## 1.2 Outline

The purpose of this work is to analyze two flexible pulse shaping techniques to reduce the OOBE and ACI of OFDM-based waveforms. The filters here studied can be applied to enable the use of non-contiguous spectrum blocks for transmission and the relaxation of the OFDM orthogonality and synchronism constraints in order to multiplex different services or users in a single waveform, where each can have an arbitrary set of parameters.

This work addresses the window-based pulse shaping to reduce the OOBE in the transmitter and ACI in the receiver. As a matter of flexibility, the use of raised cosine (RC) filters for all the OFDM subcarriers has been considered and efficient realizations in the time domain are obtained. The effects of the window roll-off length on the in-band performance is analyzed mathematically in terms of ISI/ICI and expressed as SIR variations. The reduction of the OOBE is analyzed by simulations of power spectrum density (PSD) of LTE waveforms. Link-level simulations are performed for a fragmented spectrum scenario to analyze the effectiveness of pulse shaping to reduce the ACI and exploit the spectrum holes.

This work addresses the design of pulse shaping filters with small stopband sidelobes for subband filtering. They are designed using the conventional Parks-McClellan algorithm for equiripple filters with a customization of the weighting function to obtain configurable frequency responses able to meet arbitrary SEMs. They have been called semi-equiripple because of its equiripple passband and non-equiripple stopband characteristics. As an example, compliance with ISDB-T and LTE SEM specifications is analyzed.

The ISI caused by symbol dispersion related to the group delay, symbol echoes due to the passband ripples and ISI amplification due to the outlier samples in the tails of the impulse response are analyzed mathematically and simulated using test signals. The tail samples of semi-equiripple filters are successively attenuated which might act as a protection against ISI. Then, a comparison of the impulse responses of semi-equiripple filters with those of windowed truncated *sinc* and equiripple filters is performed. Through simulations of SIR and statistical error vector magnitude (EVM) for several filters, it is observed the relationship and trade-offs between the ISI and ICI levels and the filter order, passband ripple magnitudes and CP length.

This work proposes filter structures for actual implementations for low complexity and operation at high speed. Modular structures based on cascade filters as well as methods for datapath scaling to minimize the round-off noise and overflow occurrences are presented. The reduction of round-off noise is analyzed by simulation considering the effect of section sequencing. It is also presented an implementation proposal of the filter using a systolic structure and dedicated DSP blocks of a field programmable gate array (FPGA).

The remainder of this work is structured as follows:

Chapter 2 adresses the per-subcarrier pulse shaping method based on windowing. A mathematical model of OFDM is presented in section 2.2 as background to analyze the spectral leakage. In section 2.3, two window formats are presented and the suppression of OOBE is analyzed. Section 2.4 focuses on analytic derivations of constraints to limit the ISI and ICI contributions when some samples of CP are used for windowing, and an expression for the SIR is obtained. Section 2.5 analyzes a window format for receive pulse shaping for reduction of ACI and section 2.6 presents numerical simulations of in-band and OOB performances. These results have been partially published in [16].

Chapter 3 addresses the design and performance analysis of filters for subband-based pulse shaping. Section 3.2 presents the design of semi-equiripple filters. Section 3.3 analyzes the ISI caused by the in-band ripple distortion to study appropriate design trade-offs between the filter characteristics and the waveform performance. Section 3.4 presents architectures and considerations for fixed-point implementations. Section 3.5 is devoted to performance analysis in terms of the PSD, modulation performance and support of asynchronous transmissions in multiple subbands of a single waveform. The effects of section scaling and section sequencing are analyzed at the end of this section.

Finally, this work is concluded and future works are proposed.

# 2 Window-based OFDM Pulse Shaping

## 2.1 Introduction

The challenges imposed by the requirements of the forthcoming 5G cellular technology make the development of waveforms with better frequency localization than OFDM and new transmission techniques of paramount importance [17, 18].

OFDM is the modulation method adopted in 4G LTE cellular technology and the idea behind it is the subdivision of a high rate serial data stream in a high number of low rate parallel data streams which modulate a group of baseband overlapped orthogonal subcarriers. As a consequence, a wideband frequency selective channel is reduced to various narrowband flat fading channels which makes OFDM robust against multipath fading and enables the use of low-complexity equalizers to compensate the channel response. Further, OFDM offers high immunity to channel delay spread and ISI using symbols with cyclic prefix, it can be implemented very efficiently using FFT and inverse FFT algorithms, and it supports adaptive data modulation.

However, OFDM is not free from constraints and drawbacks. Its poor spectral containment (large OOBE around active subcarriers) limits its ability to provide multiple heterogeneous services within the waveform, as well as its use in shared and fragmented spectrum scenarios. In OFDM, a rectangular pulse shape is used to modulate each subcarrier which results in high spectral sidelobes and eventually in OOBE. Carrier frequency offset (CFO) may cause loss of orthogonality between subcarriers (i.e., ICI) originating the high sensitivity of the waveform to frequency synchronization errors [19]. ISI and ICI are introduced into a received signal when CP is not sufficient to contain the time dispersion of previous symbols. Additionally, OFDM suffers from high peak-to-average power ratio (PAPR). Thus, given these drawbacks and the strict synchronization and orthogonality paradigms, the use of OFDM in 5G systems is not taken for granted [18, 13].

This chapter addresses a pulse shaping method to reduce the OOBE and adjacent channel interference (ACI) of OFDM waveforms on the transmitter and receiver respectively whilst the benefits of OFDM are preserved. A mathematical model of OFDM is developed below that includes the pulse shaping operation as part of waveform formulation.

## 2.2 System model

A baseband continuous-time OFDM signal with $N$ subcarriers and arbitrary pulse shaping function can be expressed as

$$x(t) = \sum_{l=-\infty}^{\infty} \sum_{k=0}^{N-1} S_{k,l} p(t - lT) e^{j2\pi f_k (t - lT)}, \tag{2.1}$$

where $j = \sqrt{-1}$, $N$ is the inverse FFT length, $f_k$ is the frequency of the $k$-th subcarrier, $p\,(t)$ is the time-limited pulse shaping function, $T$ is the total symbol duration, and $S_{k,l}$ is the input data symbol sequence transmitted on the $k$-th subcarrier during the $l$-th OFDM symbol where $k = 0, 1, ..., N-1$. It is assumed that $S_{k,l} \in \{S_{0,l}, S_{1,l}, ..., S_{N-1,l}\}$ is zero mean i.i.d. and also that a frequency spacing between two consecutive subcarriers is defined as $\Delta f = 1/T_N$ to keep orthogonality between all subcarriers over the useful symbol period $T_N$. Hence, the frequency separation between two arbitrary subcarrier is given by

$$f_{k_1} - f_{k_2} = \frac{k_1 - k_2}{T_N} = (k_1 - k_2)\Delta f, \tag{2.2}$$

where $k_1$ and $k_2$ denotes the position of the $k_1$-th and $k_2$-th subcarrier respectively.

CP samples can be included at the beginning of the symbol to absorb channel delay spreads and in this case, $T_N$ is extended by $T_{CP}$ such that the total symbol duration is $T = T_{CP} + T_N$. Sampling $x(t)$ at $t = nT_N/N$, the discrete-time OFDM signal can be expressed by

$$x[n] = \sum_{l=-\infty}^{\infty} \sum_{k=0}^{N-1} S_{k,l} p[n - lN_T] e^{j2\pi k(n - lN_T)/N}, \tag{2.3}$$

where $n \in Z$ is the sample index, $N_{CP}$ and $N_T$ are the number of samples of the CP and the OFDM symbol respectively, i.e., $N_T = N_{CP} + N$.

The spectral content of an OFDM signal with cyclic prefix (CP-OFDM) and arbitrary pulse shaping is described using its power spectral density (PSD) given by

$$PSD_x(f) = \frac{1}{T} \sum_{k=0}^{N-1} E\left[|S_{k,l}|^2\right] \left| P\left(f - \frac{k}{T_N}\right) \right|^2, \tag{2.4}$$

where $P(f)$ is the Fourier transform of $p(t)$.

In conventional CP-OFDM, $p[n]$ is defined as a rectangular function causing fast transitions between consecutive symbols resulting in high spectral sidelobes around active subcarriers which in turn can cause ACI and interference among in-band subcarriers (i.e., ICI). The PSD of this rectangular function is given by

$$PSD_{x,rect} = T \sum_{k=0}^{N-1} E\left[|S_{k,l}|^2\right] \left| sinc\left[T\left(f - \frac{k}{T_N}\right)\right] \right|^2, \tag{2.5}$$

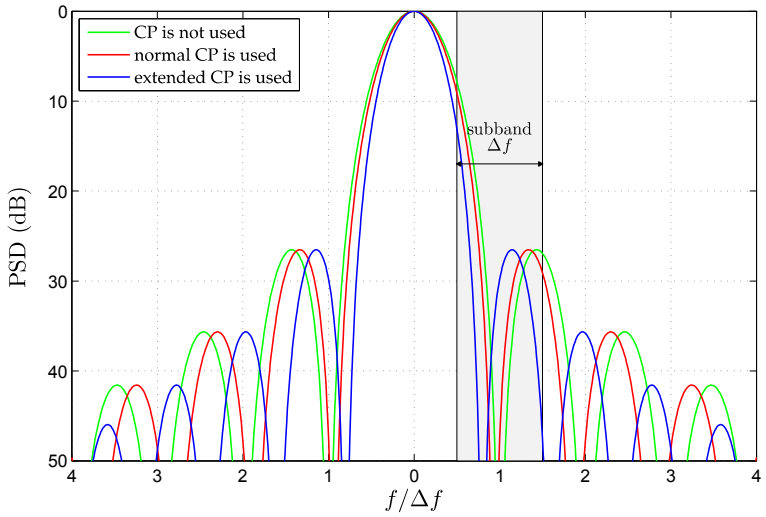


Figure 2 – PSD of a single LTE 5-MHz OFDM subcarrier.

and it is depicted in Fig. 2 for a LTE subcarrier. Significant OOBE is generated beyond the active subcarrier. Additionally its seen that zero intersections and sidelobe peaks of the *sincs* are shifted in frequency when different CP lengths are appended to the symbols [20, 4], however it does not cause synchronization errors since the CP is discarded at the receiver.

## 2.3 Transmit pulse shaping for reduction of out-of-band emission

From Eq. (2.3), it is clear that an optimized filter (e.g., better than a rectangular function) could be used per each subcarrier (i.e.,$S_{k,l}$) to attenuate the power of the sidelobes and thus reducing the waveform spectral leakage. Considering the same filter $p[n]$ for all the subcarriers, it can be extracted from the Eq. (2.3) and be implemented as a single windowing operation over the complete CP-OFDM symbol, i.e., each CP-OFDM symbol and an appropriate window can be multiplied element by element such that the fast transitions at the edges of the symbols are smoothed and thus generating low spectral sidelobes. This waveform format is named windowed OFDM here.

The raised cosine (RC) window is used here because it allows to choose the number of samples in the transition region, however any other window could be employed. It is expressed by

$$p[n] = \begin{cases} \frac{1}{2} + \frac{1}{2}\cos\left[\pi\left(1 + \frac{n}{\beta\tilde{N}_T}\right)\right], & 0 \leqslant n < \beta\tilde{N}_T \\ 1, & \beta\tilde{N}_T \leqslant n < \tilde{N}_T \\ \frac{1}{2} + \frac{1}{2}\cos\left[\frac{\pi(n-\tilde{N}_T)}{\beta\tilde{N}_T}\right], & \tilde{N}_T \leqslant n < \tilde{N}_T(1+\beta) \end{cases} \tag{2.6}$$

where $\beta$ is the roll-off factor and $\tilde{N}_T$ is the transmission period of a OFDM symbol.

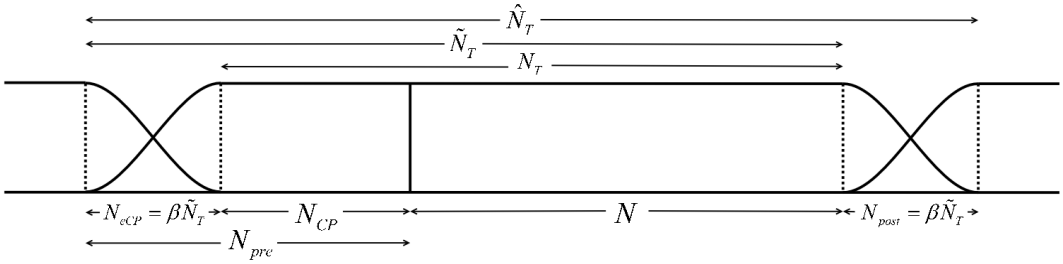


(a) format 1

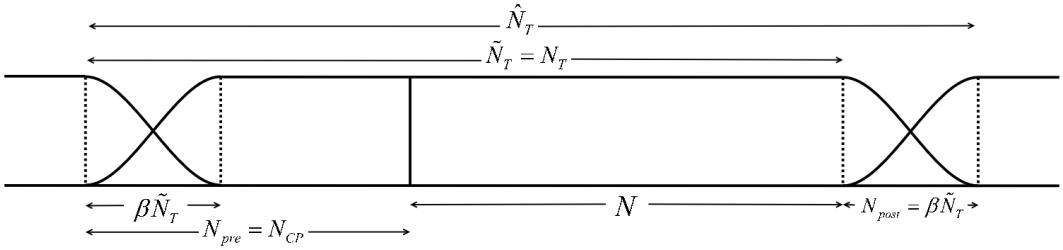


(b) format 2

Figure 3 – Transmit pulse shaping formats.

Two window formats are shown in Fig. 3. The first one (Fig. 3a) extends the symbol duration from $N_T$ to $\tilde{N}_T$ samples in order not to distort the original $N_{CP}$ samples when the symbol is reshaped. This format preserves the ISI immunity of conventional CP-OFDM and avoids the need for extra processing at the receiver. The resulting prefix denoted by $N_{pre}$ is the CP extended by $N_{eCP} = \beta\tilde{N}_T$ samples such that $N_{pre} = N_{CP} + N_{eCP}$. A cyclic postfix with $N_{post} = \beta\tilde{N}_T$ samples is also appended at the tail end of the symbol such that the total window length is $N_{pre} + N + N_{post}$ which is represented by $\hat{N}_T$. In order to reduce the degradation of the spectral efficiency caused by wastage of time and energy in the transmission of the cyclic prefix, consecutive OFDM symbols are allowed to partially overlap in the roll-off regions $N_{eCP}$ and $N_{post}$.

The second format in Fig. 3b could be used when it is not possible to extend the CP. The OFDM total transmission period is only $N_T$ samples. As it will be shown below, in this case, some samples of the CP could be used for the transition region without significant BER degradation.

The effect of $\beta$ on the reduction of OOBE can be evaluated in terms of the mean relative interference power ($\bar{P}_{leak}$) of a single subcarrier into a subband with bandwidth $\Delta f$ located $n$ subcarrier positions away. $\bar{P}_{leak}$ is given by [4]

$$\bar{P}_{leak}(n) = \frac{1}{P_{tot}} \int_{(n-0.5)\Delta f}^{(n+0.5)\Delta f} PSD_x(f)df \tag{2.7}$$

where $PSD_x(f)$ is the PSD of the waveform given by (2.4) and $P(f)$ can be replaced by

the Fourier transform of the raised cosine pulse expressed as

$$|P_{rc}(f)| = \left| T_w \frac{\sin(\pi f \tilde{T})}{\pi f \tilde{T}} \frac{\cos(\pi \beta f \tilde{T})}{1 - (2\beta f \tilde{T})^2} \right| \tag{2.8}$$

where $\tilde{T}$ is the equivalent continuous time of the transmission period $\tilde{N}_T$. Table 1 presents this parameter for some values of $n$

Table 1 – Mean relative interference power of a pulse shaped OFDM subcarrier into adjacent subcarriers. LTE subcarrier spacing $\Delta f = 15$ KHz, RC window format 2

| n | 1 | 2 | 3 | 4 |
|---|---|---|---|---|
| Normal CP Mode (144 $T_{su}$) | | | | |
| $\beta = 0$ | 6.9722 | 1.2165 | 0.5049 | 0.2763 |
| $\beta = 0.15$ | 6.9993 | 1.0391 | 0.3277 | 0.1214 |
| $\beta = 0.5$ | 5.6142 | 0.1531 | 0.002 | 0.0006 |
| $\beta = 0.75$ | 4.2365 | 0.0129 | 0.0007 | 0.0001 |
| Extended CP Mode (512 $T_{su}$) | | | | |
| $\beta = 0$ | 4.9222 | 0.8475 | 0.4832 | 0.3059 |
| $\beta = 0.15$ | 4.8466 | 0.6779 | 0.2844 | 0.1066 |
| $\beta = 0.5$ | 3.2540 | 0.0271 | 0.0019 | 0.0003 |
| $\beta = 0.75$ | 2.0561 | 0.0042 | 0.0002 | 0.0001 |

$T_{su} = 1/30720000$ sec

The PSD for some values of $\beta$ is shown in Fig. 4. It can be seen that the power of the sidelobes decreases as $\beta$ increases, e.g. for $\beta = 0$, 0.15, 0.5, and 0.75, the sidelobe levels at frequency $f/\Delta f = 1$ are attenuated by -29.8 dB, -30.4 dB, -36.5 dB, and -46.1 dB respectively.

In Fig. 3(b), samples of CP are smoothed by the window roll-off region which in order it not to distort the $N$ useful samples, $\beta$ can be extended to a maximum value of $N_{CP}/\tilde{N}_T$. For example, in an additive white Gaussian noise (AWGN) channel, LTE 5-MHz OFDM symbols with extended CP (CP length = 128 samples, $N_T = 640$ samples) could be specified with a maximum value of $\beta$ of 0.2 with no BER degradation. Fig. 5 shows the reduction of the OOBE for some values of $\beta$.

## 2.4 ISI and ICI analysis

ISI and ICI are analyzed in this section for the case when a portion of the CP is reshaped by the windowing roll-off region and the remaining CP is not sufficient to compensate the

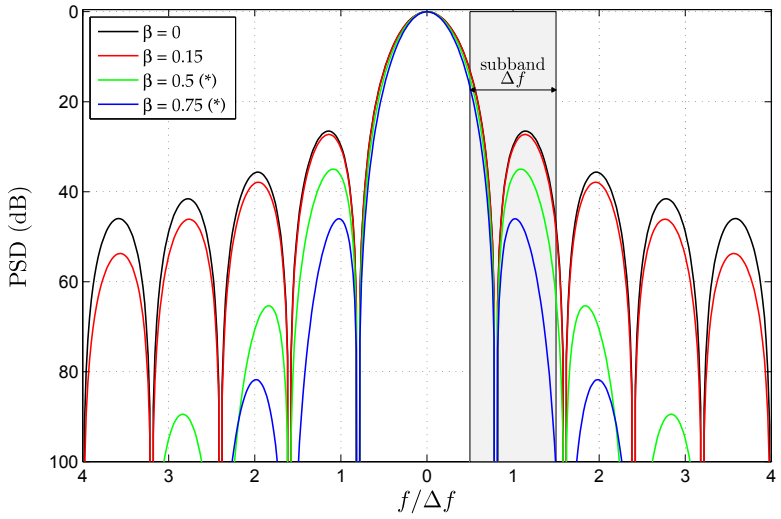


Figure 4 – Effect of $\beta$ on the reduction of OOBE of a single subcarrier. W-OFDM LTE subcarrier, $\Delta f = 15$ KHz, RC window format 2, extended CP, *some samples of the useful period $T_N$ are used for the windowing roll-off region

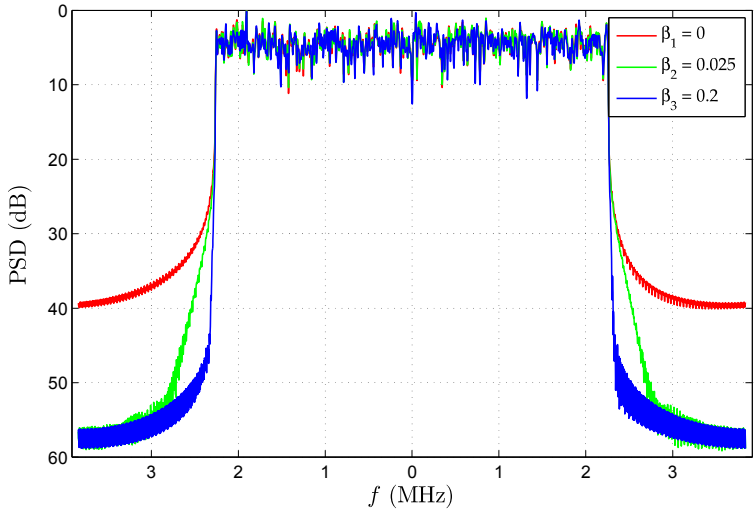


Figure 5 – Effect of $\beta$ on the reduction of the OOBE of the entire OFDM bandwidth. W-OFDM LTE waveform, bandwidth 5-MHz, extended CP, RC window format 2, $\beta$ is constrained to its maximum value $N_{CP}/\tilde{N}_T = 0.2$

distortion due to channel delay spread. If two consecutive symbols are allowed to partially overlap, the transmitted $l$-th W-OFDM symbol can be described by

$$x^l[n] = \sum_{k=0}^{N-1} S_{k,l} p[n] e^{j2\pi kn/N} + \sum_{k=0}^{N-1} S_{k,l-1} p[n+\tilde{N}_T] e^{j2\pi k(n+\tilde{N}_T)/N} \tag{2.9}$$

where $n = -N_{pre}, ..., 0, ..., N-1$ is the sample index, $\tilde{N}_T = N + N_{pre}$ is the transmission period of a symbol, $S_{k,l}$ and $S_{k,l-1}$ represent the data symbols in the $l$-th and $(l-1)$-th W-OFDM symbols respectively and since the window function is time-limited, the second summation term is non-zero only in $n = -N_{pre}, ..., -N_{pre} + N_{post} - 1$. To simplify the analysis, matrix representations are used hereafter so Eq. (2.9) can be re-expressed as

$$\mathbf{X}^l = \mathbf{T}(\mathbf{PGF}^H \mathbf{S}_{k,l} + \mathbf{EPGF}^H \mathbf{S}_{k,l-1}) \tag{2.10}$$

where $k = 0, 1, ..., N-1$, $\mathbf{X}^l \in \mathbb{C}^{\tilde{N}_T}$ is the vector containing samples of the $l$-th W-OFDM symbol overlapped with the previous one; $\mathbf{S}_{k,l}$ and $\mathbf{S}_{k,l-1} \in \mathbb{C}^N$ are vectors of data of the $l$-th and $(l-1)$-th symbols respectively; $\mathbf{F} \in \mathbb{C}^{N \times N}$ is the N-point discrete Fourier transform (DFT) matrix whose elements are $[F]_{r,c} = e^{-j2\pi rc/N}$ being $r$ and $c \in \{0, 1, ..., N-1\}$; $\mathbf{P} \in \mathbb{N}^{\hat{N}_T \times \hat{N}_T}$ is a diagonal matrix such that $\mathbf{P} = diag(p[n])$; and $\mathbf{G}$, $\mathbf{E}$ and $\mathbf{T}$ are defined by Eq. (2.11), (2.12) and (2.13) respectively.

$$\mathbf{G} = \begin{bmatrix} 0_{Npre \text{ x } (N-Npre)} & I_{Npre} \\ I_N & \\ I_{Npost} & 0_{Npost \text{ x } (N-Npost)} \end{bmatrix} \tag{2.11}$$

$$\mathbf{E} = \begin{bmatrix} 0_{Npost \text{ x } \tilde{N}_T} & I_{Npost} \\ 0_{\tilde{N}_T \text{x} \hat{N}_T} & \end{bmatrix} \tag{2.12}$$

$$\mathbf{T} = \begin{bmatrix} I_{\tilde{N}_T} & 0_{\tilde{N}_T \text{x} Npost} \end{bmatrix} \tag{2.13}$$

$\mathbf{G} \in \mathbb{R}^{\hat{N}_T \times N}$ appends a prefix and postfix of $N_{pre}$ and $N_{post}$ samples respectively to both symbol tails; $\mathbf{E} \in \mathbb{N}^{\hat{N}_T \times \hat{N}_T}$ selects the last $N_{post}$ samples of the $(l-1)$-th symbol to be added (overlapped) to the first $\beta\tilde{N}_T$ samples of the $l$-th symbol and therefore $N_{post} = \beta\tilde{N}_T$; and $\mathbf{T} \in \mathbb{N}^{\tilde{N}_T \times \hat{N}_T}$ selects the first $\tilde{N}_T$ samples for transmission.

The discrete-time model of the multipath channel during the $l$-th symbol can be expressed by

$$h^l[n] = \sum_{m=0}^{L-1} \alpha^l[m] \delta[n-m] \tag{2.14}$$

where $L$ is the number of paths, $\alpha[m]$ and $m$ represents the complex amplitudes and propagation delays respectively. If $L < \tilde{N}_T$, then possible ISI on $l$-th symbol would occur

only from the time spreading of the $(l-1)$-th symbol. Convolution in the time domain for the received signal corresponds to multiplication of $\mathbf{X}^l$ with the channel:

$$\mathbf{Y}^l = \mathbf{H}^{(0)}\mathbf{X}^l + \mathbf{H}^{(1)}\mathbf{X}^{l-1} \tag{2.15}$$

where $\mathbf{H}^0$ and $\mathbf{H}^1$ are the channel matrices defined by

$$H^{(0)} = \begin{bmatrix} h_0 & 0 & \cdots & \cdots & \cdots & \cdots & 0 \\ h_1 & h_0 & \ddots & \ddots & \ddots & \ddots & \vdots \\ \vdots & \ddots & \ddots & \ddots & \ddots & \ddots & \vdots \\ h_{L-1} & \cdots & \cdots & h_0 & 0 & \ddots & \vdots \\ 0 & h_{L-1} & \cdots & \cdots & h_0 & \ddots & \vdots \\ \vdots & \ddots & \ddots & \ddots & \ddots & \ddots & 0 \\ 0 & \cdots & 0 & h_{L-1} & \cdots & \cdots & h_0 \end{bmatrix}_{\tilde{N}_T \times \tilde{N}_T} \tag{2.16}$$

$$H^{(1)} = \begin{bmatrix} 0 & \cdots & \cdots & 0 & h_{L-1} & \cdots & h_1 \\ \vdots & \ddots & \ddots & \ddots & \ddots & \ddots & \vdots \\ \vdots & \ddots & \ddots & \ddots & \ddots & 0 & h_{L-1} \\ \vdots & \ddots & \ddots & \ddots & \ddots & \ddots & 0 \\ \vdots & \ddots & \ddots & \ddots & \ddots & \ddots & \vdots \\ \vdots & \ddots & \ddots & \ddots & \ddots & \ddots & \vdots \\ 0 & \cdots & \cdots & \cdots & \cdots & \cdots & 0 \end{bmatrix}_{\tilde{N}_T \times \tilde{N}_T} \tag{2.17}$$

The first term in (2.15) is the convolution between the channel and $l$-th symbol which has some samples self distorted due to symbol overlapping and the second term is the ISI from the $(l-1)$-th symbol. OFDM waveforms can be designed with a CP longer than the maximum channel delay spread that is discarded at the receiver as

$$\tilde{\mathbf{Y}}^l = \mathbf{R}\mathbf{Y}^l \tag{2.18}$$

where $\tilde{\mathbf{Y}}^l \in \mathbb{C}^N$ is the received OFDM symbol after $N_{PRE}$ first samples are discarded and $\mathbf{R} \in \mathbb{N}^{N \times \tilde{N}_T}$ is defined as

$$\mathbf{R} \triangleq \begin{bmatrix} 0_{N \times Npre} & I_N \end{bmatrix} \tag{2.19}$$

Therefore, the $N$ received subcarriers after FFT operation can be expressed as

$$\mathbf{Y}^l_{FFT} = \mathbf{F}\mathbf{R}\mathbf{H}^{(0)}\mathbf{T}\mathbf{P}\mathbf{G}\mathbf{F}^H\mathbf{S}_{k,l} + \mathbf{F}\mathbf{R}\mathbf{H}^{(0)}\mathbf{T}\mathbf{E}\mathbf{P}\mathbf{G}\mathbf{F}^H\mathbf{S}_{k,l-1} \tag{2.20}$$

Because some samples of CP are used for windowing, the self introduced ISI may not be absorbed by the remaining guard interval, which in frequency domain results in ICI. This

distortion can be measured using the SIR parameter on a per-subcarrier basis. If $\mathbf{S}_{k,l}$ and $\mathbf{S}_{k,l-1}$ are i.i.d., the SIR on an arbitrary received $k'$ subcarrier can be expressed as

$$SIR_{k'} = \frac{\mu_{l,k=k'}}{\mu_{l,k\neq k'} + \lambda_{l-1,k}} \tag{2.21}$$

where

$$\mu_{l,k=k'} = \left|\mathbf{F}_{k'}\mathbf{R}\mathbf{H}^{(0)}\mathbf{T}\mathbf{P}\mathbf{G}\mathbf{U}_1\mathbf{F}^H\mathbf{S}_{k,l}\right|^2 \tag{2.22}$$

$$\mu_{l,k\neq k'} = \left|\mathbf{F}_{k'}\mathbf{R}\mathbf{H}^{(0)}\mathbf{T}\mathbf{P}\mathbf{G}\mathbf{U}_2\mathbf{F}^H\mathbf{S}_{k,l}\right|^2 \tag{2.23}$$

$$\lambda_{l-1,k} = \left|\mathbf{F}_{k'}\mathbf{R}\mathbf{H}^{(0)}\mathbf{T}\mathbf{E}\mathbf{P}\mathbf{G}\mathbf{F}^H\mathbf{S}_{k,l-1}\right|^2 \tag{2.24}$$

$k$ and $k' \in \{0, 1, ..., N-1\}$, $\mathbf{F}_{k'}$ is the FFT $k'$-th component, $U_1$ and $U_2 \in \mathbb{N}^N$ are defined by

$$U_1[k] = \delta(k - k') \tag{2.25}$$

$$U_2[k] = 1 - \delta(k - k') \tag{2.26}$$

$\mu_{l,k=k'}$ represents the received power on $k'$ subcarrier in the $l$-th symbol, $\mu_{l,k\neq k'}$ is the contribution of the other subcarriers in the same symbol, and $\lambda_{l-1,k}$ is the ICI from the $(l-1)$ symbol. $\tilde{\mathbf{Y}}^l$ can still contain ISI from the symbol $\mathbf{X}^{l-1}$ if the dispersion of the first $\beta\tilde{N}_T$ samples of $\mathbf{X}^l$ in (2.10) is not absorbed by the remaining non-distorted CP. Considering a roll-off region with $\beta\widetilde{N}_T$ samples, the dispersion of the transmitted overlapped samples is

$$N_{spread} = \beta\widetilde{N}_T + L - 1 \tag{2.27}$$

Hence, if $N_{pre} - \beta\widetilde{N}_T \geqslant L - 1$ neither ISI nor ICI ocurrs, otherwise the number of useful samples that are distorted by ISI will be

$$N_{isi} = \beta\widetilde{N}_T + L - 1 - N_{PRE} \tag{2.28}$$

which corresponds to samples that were not absorbed by the CP and so it will cause orthogonality loss between received subcarriers.

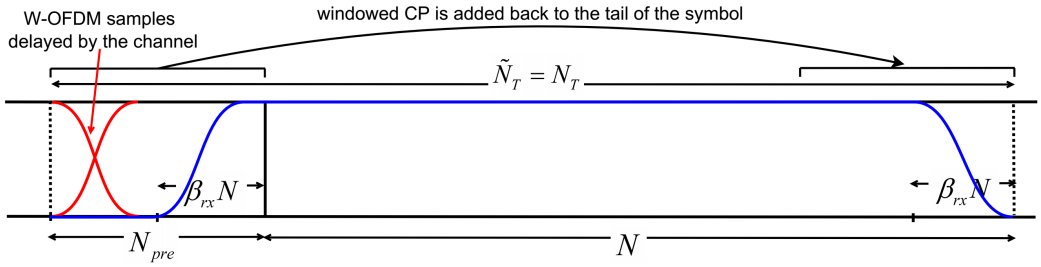


Figure 6 – Receiver pulse shaping format.

## 2.5 Receive pulse shaping for reduction of adjacent channel interference

Since the CP is removed in the receiver before the FFT using a rectangular function (Eq. (2.19)), this creates signal discontinuity and therefore large sidelobes which can amplify ACI in a target channel even if the adjacent one has low spectrum leakage. This effect becomes particularly important in fragmented spectrum scenarios as discussed in the next section. A appropriate window function can be used at the receiver side to overcome this problem. A RC window for receiver pulse shaping can be expressed as

$$p_{rx}[n] = \begin{cases} 0, & 0 \leqslant n < N_{pre} - \beta_{rx}N, \\ \frac{1}{2} + \frac{1}{2}\cos\left[\pi\left(1 + \frac{n}{\beta N}\right)\right], & N_{pre} - \beta_{rx}N \leqslant n < N_{pre}, \\ 1, & N_{pre} \leqslant n < N + N_{pre} - \beta_{rx}N, \\ \frac{1}{2} + \frac{1}{2}\cos\left[\frac{\pi(n-N)}{\beta N}\right], & N + N_{pre} - \beta_{rx}N \leqslant n < N + N_{pre}. \end{cases} \tag{2.29}$$

where $\beta_{rx}$ is the receiver roll-off factor. The receiver window is applied over the entire symbol and in order to achieve low levels of ACI, the roll-off portion could cover the entire CP portion. However, ISI would be introduced if the transmitted W-OFDM samples delayed by the channel are covered as well. This is indicated by the blue and red lines in the receiver window format shown in Fig. 6. The windowed CP portion is added to the symbol tail end and the following condition must be satisfied to keep orthogonality in the symbol:

$$p_{rx}[n] + p_{rx}[n+N] = constant,\ N_{pre} - \beta_{rx}N \leqslant n < N_{pre} \tag{2.30}$$

So the Eq. (2.19) can be expressed as

$$\mathbf{R} \triangleq \begin{bmatrix} 0_{(N-Npre)\times Npre} & I_N \\ I_{Npre} & \end{bmatrix} \mathbf{P}_{rx} \tag{2.31}$$

where $\mathbf{P}_{rx} \in \mathbb{N}^{N_T \times N_T}$ is a diagonal matrix such that $\mathbf{P}_{rx} = diag(p_{rx}[n])$.

## 2.6 Numerical results

By windowing the OFDM waveform in the transmitter improves its spectral containment, but the tolerance to channel spread is reduced if the window is applied over the CP. This effect is evaluated below in terms of the SIR parameter previously obtained and BER. An LTE link-level simulation model has been implemented in Matlab to evaluate the performance of the pulse shaping at both transmitter and receiver sides. A brief description of the numerology employed is as follows: the sampling frequency is 7.68 MHz and the FFT size is 512 points. The useful bandwidth is 4.5 MHz that consists of 300 subcarriers arranged in 25 resource blocks (RBs) with each RB being composed of 12 subcarriers. A 0.25 MHz guard band is set at both sides of the spectrum. The subcarrier frequency spacing is 15 KHz and the useful symbol duration $T_N$ is 66.7 $\mu$s. The OFDM frame is divided into 20 slots of 0.5 ms each and the number of symbols per slot depends of the CP mode. Two CP modes are defined in LTE, the normal CP of 4.7 $\mu$s (36 samples) and the extended CP of 16.7 $\mu$s (128 samples) where each slot contains 7 and 6 symbols respectively. In normal CP mode, the duration of the first symbol is 5.2 $\mu$s (40 samples). The channel is considered to be Extended Vehicular A (EVA) with Doppler frequency 70 Hz [21] and AWGN.

### 2.6.1 Signal-to-interference ratio

The channel coefficients are considered constant over a coherence time assumed to be equal to the duration of an OFDM frame (10 ms). The SIR in (2.21) has been evaluated along the frame transmission and averaged in each active subcarrier. The number of samples in the roll-off region $\beta\tilde{N}_T$ is represented by $\alpha$ and four values of $\alpha$ have been chosen in the analysis: 95, 96, 97, 124, and 350. Since the length of the considered channel impulse response is 35, thus given (2.28), there will be 1, 2, 3, 30 and 256 samples of ISI for each $\alpha$, respectively. For $\alpha < 95$, the ISI is absorbed by the remaining CP and so those cases are omitted from the figure.

The SIR in the 300 active subcarriers is shown in Fig. 7 and as can be seen, as $\beta$ increases, the spectral containment is improved but the SIR is degraded, e.g. for two and three ISI samples the SIR loss is approximately 15 and 30 dB with respect to the case where there is only one ISI sample.

Even when ISI occurs, its effect could be limited because the power of the OFDM symbols arriving from longer delay paths are smaller than those arriving first and the power contribution of the last $N_{post}$ (delayed) samples of the $(l-1)$-th symbol are attenuated by the window tail. This can be seen by disabling the window function and enabling only the symbol overlapping (Fig. 8) which results in a difference of approximately 80 dB.

In order to obtain a single indicator to evaluate the SIR performance for different values

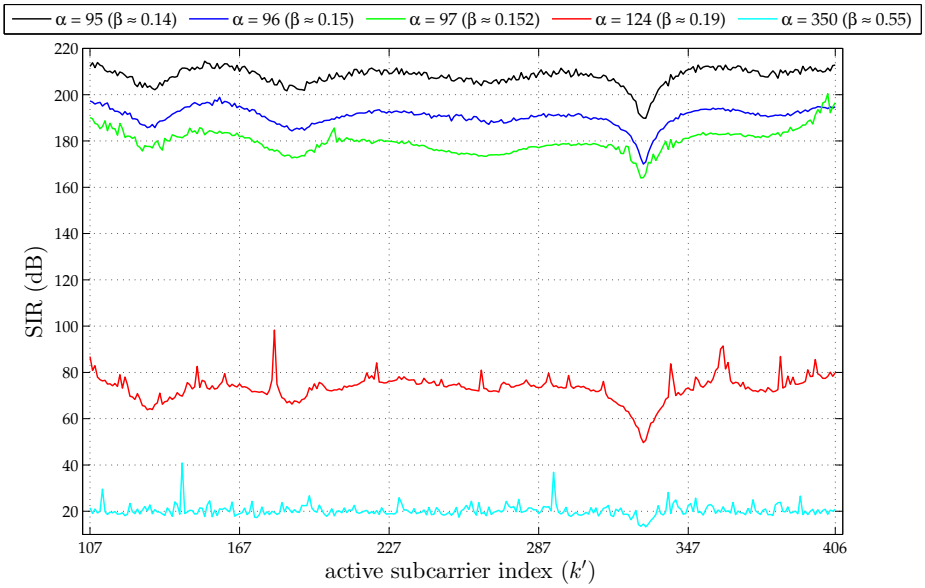


Figure 7 – Average SIR on active subcarriers for different windowing roll-off lengths. RC window format 2 is enabled, W-OFDM LTE 5-MHz waveform, extended CP, averaging of 1200 W-OFDM symbols.

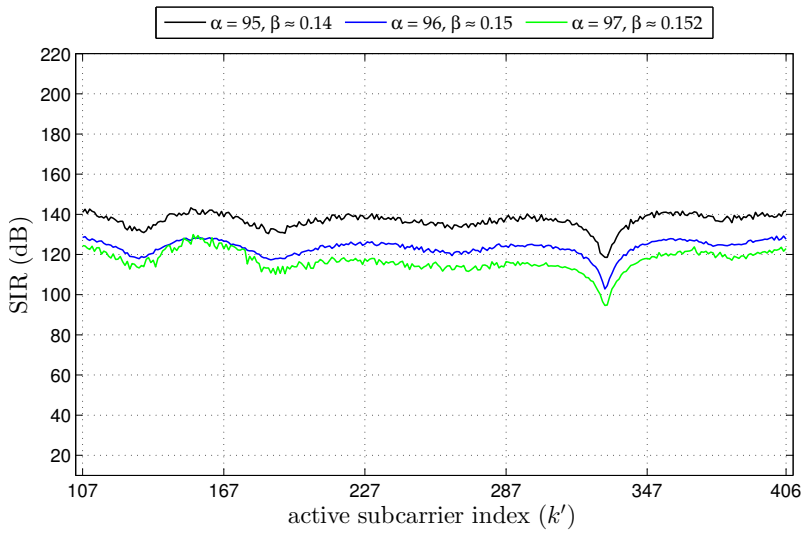


Figure 8 – Degradation of SIR performance when pulse shaping is disabled.

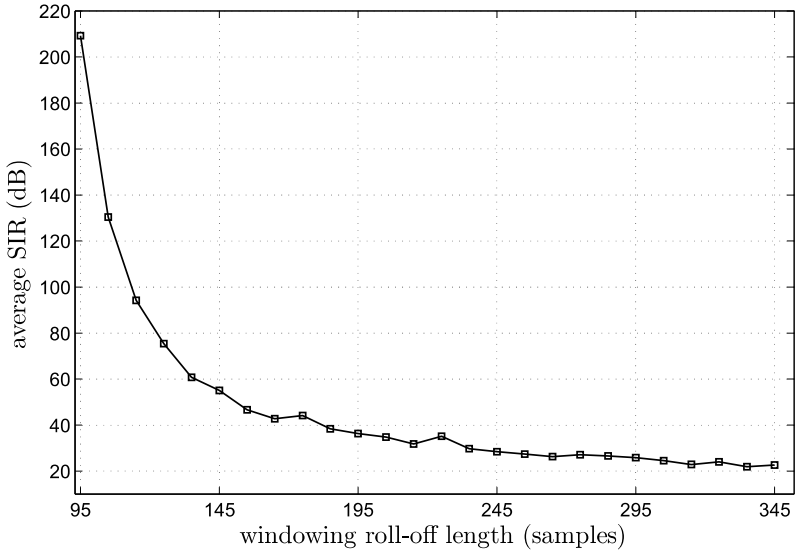


Figure 9 – Average SIR calculated over all active subcarriers for different windowing roll-off lengths. RC window format 2, W-OFDM LTE 5-MHz waveform, extended CP, averaging of 1200 W-OFDM symbols.

of the roll-off factor the SIR can be averaged over all subcarriers in the symbol as is shown in Fig. 9. The SIR performance experiments an exponential decay as $\beta$ increases so the value of $\beta$ must be chosen short enough to achieve the required low OOBE.

### 2.6.2 In-band BER performance of transmit pulse shaping filter

The in-band performance of W-OFDM is evaluated and compared to the conventional CP-OFDM. The receiver is formed by a one-tap equalizer with ideal channel estimation, CP removal stage, FFT and subcarrier demodulator. The simulation is carried out over ten LTE downlink frames (1200 symbols with extended CP) per run and 50 runs are realized. Only results for window format 2 are shown because the BER performance of window format 1 is equivalent to CP-OFDM. As can be seen in Fig. 10 BER results are consistent with the SIR in Fig. 7 and short values of $\alpha$ result in performance similar to CP-OFDM even if they originate ISI.

### 2.6.3 OOB BER performance of transmit and receive pulse shaping filter

In order to evaluate the ability of pulse shaped waveforms for leveraging spectral holes for transmission, it is considered an scheme with two independent links, one of a primary user (PU) and other of a secondary user (SU) which is allocated in a adjacent band to the first. The SU signal (interference) is shaped in the transmitter to reduce its OOBE thus the ACI caused in the PU receiver (desired transmission).

The analysis has been performed accounting the LTE 5-MHz parametrization aforementioned and the non-contiguous (fragmented) spectrum scenario shown in Fig. 11. The RB

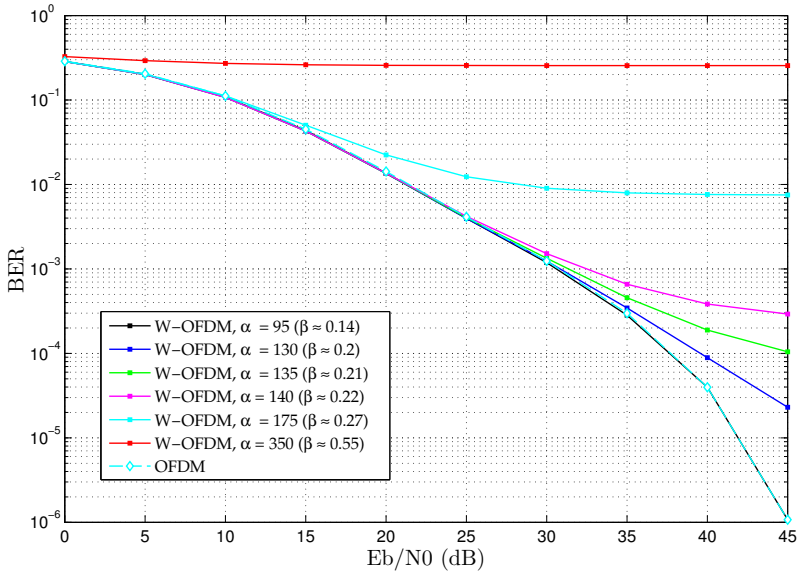


Figure 10 – BER performance of W-OFDM and CP-OFDM. 64-QAM subcarrier modulation, extended CP (128 samples), RC window format 2 with $\alpha > 94$ to include the ISI effect in the BER, channel response length = 35, simulation using 1200 OFDM symbols per run and 50 runs.

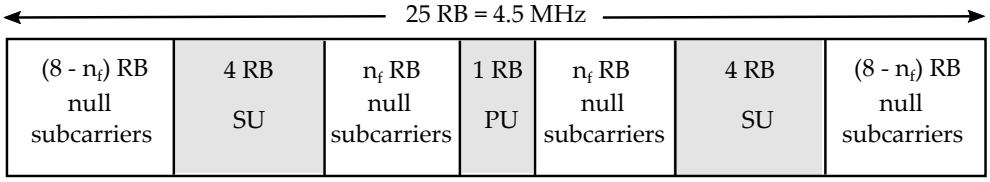


Figure 11 – 5-MHz non-contiguous spectrum band.

are distributed as follows: one RB is allocated to the PU at the center of the band, 8 RBs to the SU at both sides of the PU and the $n_f$ RBs between them are loaded with null subcarriers. The PU signal is conventional CP-OFDM whereas the SU signal is W-OFDM with power 10 dB higher and both are set with extended cyclic prefix (128 samples). To simulate an asynchronous transmission, frequency and time offsets are configured between the waveforms.

The BER results are shown in Fig. 12 for two different window roll-off lengths in the SU signal. The cases when there is no suppression of the OOBE and SU is not present are also included for comparison. As can be seen, the BER in the PU receiver improves when SU transmitted spectrum is better localized by the pulse shaping (Fig. 13a), however this benefit is limited due to the rectangular function in the PU receiver which amplify the SU OOBE that is then introduced as ACI to the PU (Fig. 13b).

The performance of the PU link is improved when the received symbols are shaped with a better window function (section 2.5) as can be seen in Fig. 14. The simulation was performed with $\beta_{rx}$ =20 and it was observed that by using longer values of it the BER can be improved obtaining the almost the same performance as the case when there is no

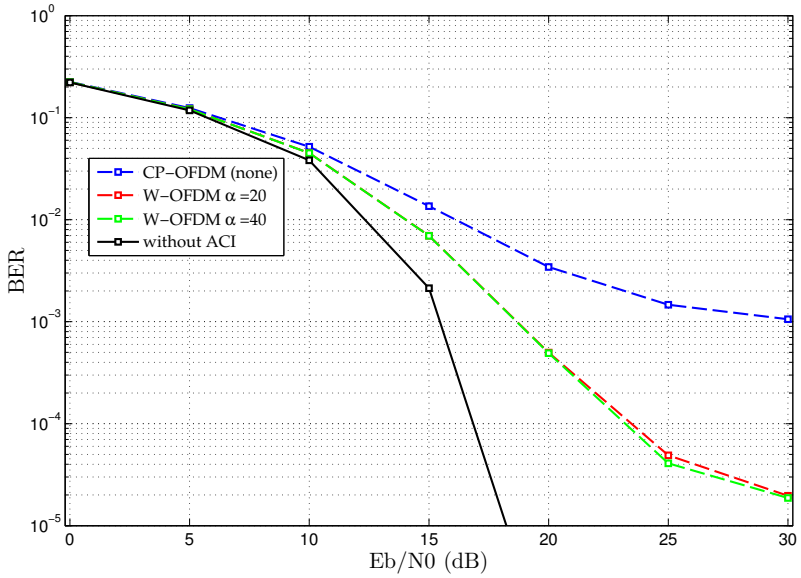


Figure 12 – BER of the PU receiver affected by ACI of a SU signal with supression of OOBE in the transmitter. Simulation using 100 OFDM frames per run and 100 runs are performed. SU and PU with 64-QAM data modulation and separated by $n_f = 2$ RBs. SU transmitted signal with power 10 dB higher than that of the PU, time offset = 150 and frequency offset = 7.5 KHz. AWGN channel.

interference even if more ISI samples are added to the payload. However, too long values of $\beta_{rx}$ could cause the ISI effect dominates the performance. Thus, a trade-off must be made between the permissible ISI level and the ACI attenuation level.

## 2.7 Summary

In this chapter, a pulse shaping method based on windowing for OOBE reduction and ACI rejection was presented.

An arbitrary pulse shaping function has been introduced in the OFDM formulation as a per-subcarrier filter and it is found that the filters can be implemented as a single element-wise multiplication in the case that all subcarriers are shaped by the same function. The use of different filters on a per-subcarrier or per-subband basis could be also possible. The RC function was taken as an example because of the flexibility to control the number of samples in the roll-off region. However, other functions with small spectral sidelobes could be also applied.

Mathematical expressions were developed to evaluate the effect of windowing on ISI when some CP samples are shaped by the roll-off region.

The SIR is a closed-form equation to measure the ICI and the results obtained are congruent with BER measurements. This metric can be used to analyze constellation accuracy.

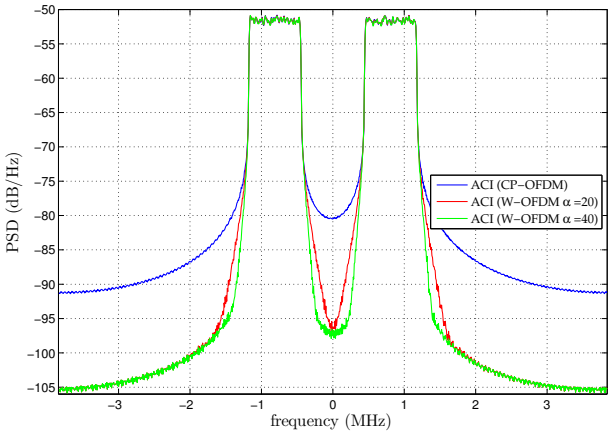


(a) before pulse shaping and CP removal

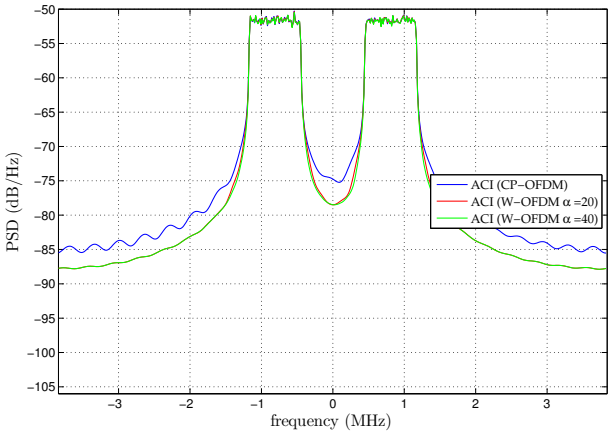


(b) after rectangular pulse shaping

Figure 13 – PSD of the received SU signal. Estimated average PSD taken over 100 OFDM symbols with different transmit roll-off factors.

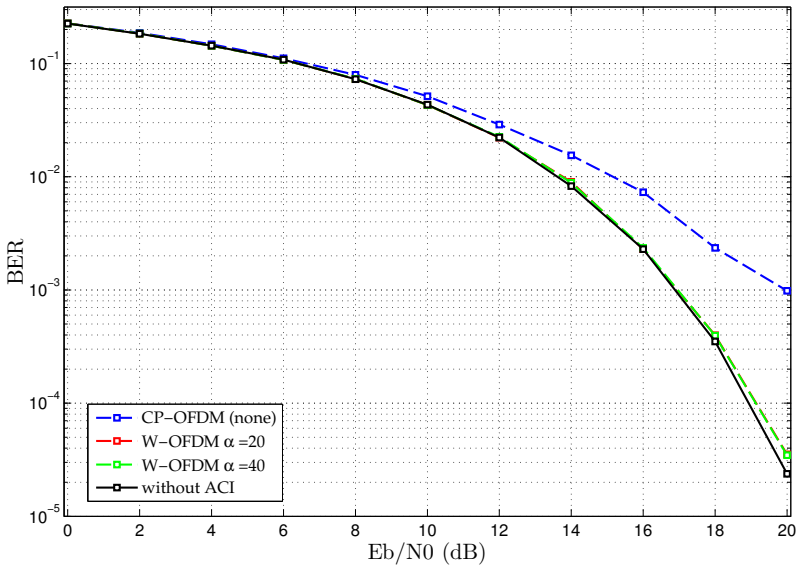


Figure 14 – BER performance of the PU receiver using a RC window for ACI rejection. Simulation with different window roll-off lengths in the SU transmitter (0, 20 and 40 samples) and a fixed roll-off in the PU receiver (20 samples), 64-QAM data modulation, EVA channel with AWGN

As more CP samples are used for the roll-off region, the OOBE gets more attenuated in the transmitter. No significant degradation on BER was observed for moderate roll-off lengths (up to $\beta \approx 0.2$), however because of self-ISI due by symbol overlapping, $\beta$ needs to be as short as possible. The SIR performance decreases fast when payload samples are shaped. At the receiver side, ACI is more rejected as $\beta_{rx}$ increases. However, as $\beta_{rx}$ increases, more ISI samples are added to the payload samples, therefore there is a trade-off between ACI and ISI.

In the following chapter, the focus will be redirected towards the use of pulse shaping filters for subband-based filtering waveforms.

# 3 Subband-based OFDM Pulse Shaping

## 3.1 Introduction

This chapter addresses the design and analysis of filters for pulse shaping of OFDM waveforms and extend the previous results in that these filters can be designed to meet tight SEM specifications to reduce the inter-subband interference in subband filtering based transceivers. The design is based on the Parks-McClellan algorithm to generate finite impulse response (FIR) filters with decaying stopband attenuation for better spectrum containment. Since the ISBI can be contained by the filters, the requirements of synchronism and orthogonality applied over the entire bandwidth are relaxed and therefore different services or users can coexist in different subbands of a single waveform as shown in Fig. 1.

These filters have been called semi-equiripple here because of its equiripple in-band and non-equiripple stopband characteristics. There are also analyzed three sources of ISI: the symbol dispersion (related to group delay), the symbol echoes (related to passband ripples) and the tail samples of the impulse response (related to ISI amplification). It is found that long impulse responses can be used for better spectral containment with a slight BER penalty due to the ISI when the filter order is longer than the length of the CP.

There are also proposed flexible structures for actual implementations to reduce the complexity and enable operation at high speed, as well as, methods for datapath scaling and section sequencing to deal with fixed-point issues (round-off noise, overflows and quantization sensitivity).

This part focuses on FIR filters because their linear-phase response characteristic causes OFDM subcarriers to experience the same delays thus avoiding ICI during demodulation, unlike infinite impulse response (IIR) filters, whose linearity is very sensitive to the effects of finite word-length. The locations of the zeros in FIR filters have less sensivity to coefficient quantization than the zeros and poles in IIR filters [22]. Also, small FIR passband ripples reduce the distortion of the amplitude of the subcarriers and prevent large excursions of the waveform envelope and thus the increase of the peak-to-average power ratio (PAPR).

In the window-based subcarrier filtering presented in the previous chapter, the filter response was defined only by the type of window used. Then, the filter can be optimized for low OOBE retaining the good in-band performance by setting the transition bandwidth, ripple amplitudes or filter order as needed. A brief description of the optimal filter design

method is given below followed by a procedure to shape the stopband with a decaying attenuation.

## 3.2 Filter design

### 3.2.1 Optimal design method

This method computes the set of coefficients of a FIR using the Chebyshev approximation and the Remez algorithm. It approximates the actual response $H(e^{j\omega})$ of a filter as close as possible to a desired ideal response $T(e^{j\omega})$. A frequency-domain weighted error function that measures the deviation between those responses is defined as

$$E(e^{j\omega}) = W(e^{j\omega})\left[H(e^{j\omega}) - T(e^{j\omega})\right], \tag{3.1}$$

where $W(e^{j\omega})$ is a weighting function. Thus, the set of coefficients is one that minimizes the maximum error given by the Chebyshev norm [22]

$$\left\|E(e^{j\omega})\right\|_{\infty} = \max_{\omega\in[0,\pi]} \left|W(e^{j\omega})\left[H(e^{j\omega}) - T(e^{j\omega})\right]\right|. \tag{3.2}$$

For a low-pass FIR, $T(e^{j\omega})$ and $W(e^{j\omega})$ can be defined as

$$T(e^{j\omega}) = \begin{cases} 1 & 0 < \omega < \omega_c \\ 0 & \omega_c < \omega < \pi \end{cases}, \tag{3.3}$$

$$W(e^{j\omega}) = \begin{cases} k_p & 0 \leqslant \omega \leqslant \omega_p \\ 0 & \omega_p < \omega < \omega_s \\ k_s & \omega_s \leqslant \omega \leqslant \pi \end{cases}, \tag{3.4}$$

where $\omega_c$ is the cutoff frequency, $\omega_p$ is the passband edge frequency and $\omega_s$ is the stopband edge frequency. In order to obtain the best solution for a type I FIR filter of order $2M$ whose impulse response $h[n]$ is given by

$$h[n] = \begin{cases} h_n & n = 0, 1, 2, ..., (2M) \\ 0 & \text{otherwise} \end{cases}, \tag{3.5}$$

and from the alternation theorem [22], the weighted error $E(e^{j\omega})$ alternates sign and has maximum absolute values on at least $M + 2$ frequency points $\omega_k$ with $0 \leqslant \omega_1 < ... < \omega_{M+2} \leqslant \pi$, therefore

$$E(e^{j\omega_k}) = (-1)^k \left\|E(e^{j\omega})\right\|_{\infty}, \tag{3.6}$$

where $k \in \{1, 2, ..., (M+2)\}$. By replacing (3.1) in (3.6) and letting $\delta = \|E(e^{j\omega})\|_\infty$,Eq. (3.6) can be expressed as the system of $M+2$ linear equations

$$H(e^{j\omega_k}) - \frac{(-1)^k \delta}{W(e^{j\omega_k})} = T(e^{j\omega_k}), \tag{3.7}$$

where $H(e^{j\omega})$ is defined by only $M+1$ coefficients of the filter. To obtain the solution set of coefficients of (3.7), first the best set of frequencies $\omega_k$ has to be determined. Eq. (3.7) is first solved for an initial set of $M+2$ frequency points uniformly spaced between 0 and $\pi$. Then, this set is updated in such a way that the error alternates sign in the new set of references and that the local maximum values of the error obtained from (3.2) exceeds the current value of $|\delta|$. These steps are performed $m$ times until the following inequality is satisfied

$$\frac{\|E_i(e^{j\omega})\|_\infty - |\delta_i|}{\|E_i(e^{j\omega})\|_\infty} < \varepsilon \approx 10^{-6}, \tag{3.8}$$

indicating that the Chebyshev error has been minimized.

### 3.2.2 Decaying stopband attenuation

Wireless standards commonly define SEMs to limit ACI [21, 23] and similar specifications could be also beneficial to reduce the ISBI in subband-based filtering waveforms. RF channel filters are usually employed to meet SEM requirements and also digital filters can be used in the baseband section [24, 25]. In single-carrier standards, the transmit shaping filter performs the spectral masking and prevents the occurrence of ISI since it is matched with the receive filter, so that each received symbol is located at the zero-crossings of the other symbols, e.g. UMTS specifies a baseband root-raised cosine (RRC) filter with roll-off factor 0.22 [26]. However, some current OFDM-based systems such as LTE, do not define transmit and receiver filters which opens the possibility to design the filter making adequate trade-offs between the characteristics of the filter (e.g. order) and the required performance (e.g. SEM, ACI). Also, the SEM can be performed in different stages of the transmission chain.

A possibility to realize such trade-offs is to employ semi-equiripple FIR filters. The function $W(e^{j\omega})$ in Eq. (3.4), which leads to a stopband decaying in 0 dB/octave, can be replaced by a non-decreasing frequency dependent function defined as

$$W(e^{j\omega}) = \begin{cases} k_p & 0 \leqslant \omega \leqslant \omega_p \\ 0 & \omega_p < \omega < \omega_s \\ k_s & \omega = \omega_s \\ k(\omega) & \omega_s < \omega \leqslant \pi \end{cases}, \tag{3.9}$$

such that (3.7) converges with lower errors at the frequencies $\omega_k$ of higher weights, where $k_s$ is the weight to obtain the desired attenuation at the stopband edge and $k(\omega)$ is an

increasing function weighting (shaping) the attenuation in the stopband and it can be defined as piece-wise continuous (Fig. 15) to obtain different levels of attenuation.

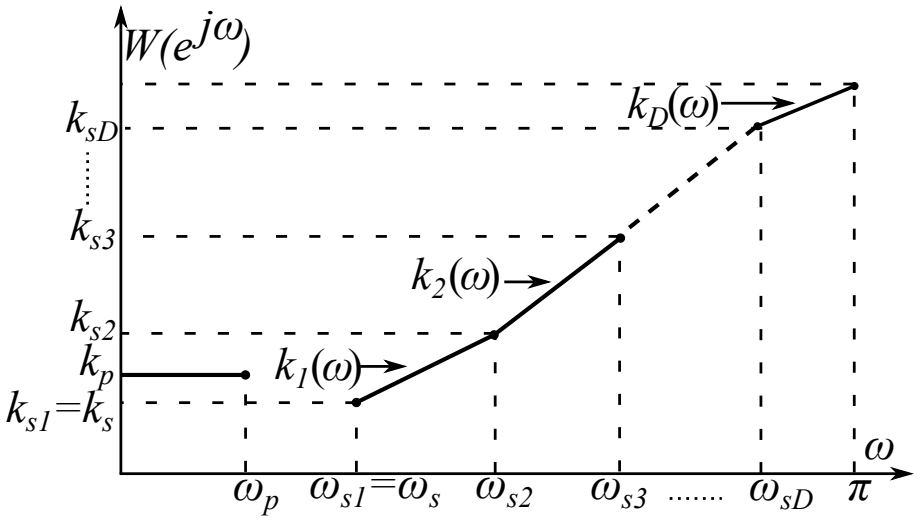


Figure 15 – Frequency-dependent weighting function

The stopband is divided into $D$ subbands each one with an arbitrary weighting function $k_i(\omega)$, where $i = 1, 2, 3, ..., D$, and the frequencies $\omega_{si}$ are the reference stopband frequencies of a given SEM whose weights are denoted by $k_{si}$. A function $k_i(\omega)$ can be obtained by interpolation of the weights at $\omega_{si}$ and $\omega_{si+1}$ and by using linear interpolation, it can be defined as

$$k_i(\omega) = k_{si} + m_i \cdot (\omega - \omega_{si}), \tag{3.10}$$

where $m_i = (k_{si+1} - k_{si})/(\omega_{si+1} - \omega_{si})$.

It is also possible to obtain a stopband with exponential decaying ($1/f^\gamma$ or $6\gamma$/octave) by defining $k(\omega)$ as

$$k(\omega) = k_s \left( \frac{\omega}{\omega_s} \right)^\gamma \tag{3.11}$$

Several filters have been designed solving Eq. (3.7) considering different $k(\omega)$ functions and the parameters listed in table 2. Their frequency responses are shown in Fig. 39.

## 3.3 Analysis of ISI caused by filter passband ripples

Pulse shaping filters with narrow transition bands are useful for good spectral containment. However, for the case of an equiripple filter, if the order and transition band are fixed, a specification of a higher stopband attenuation is exchanged by a higher level of passband ripple (in-band distortion). On the other hand, it was observed that the above mentioned weighting functions for equiripple filters do not lead to significant increasing of passband ripples (Table 3).

Table 2 – Filter specifications for different types of stopband attenuation. For all the filters: order = 130, in-band ripple $\delta_p = 0.01$ (0.17 dB), passband edge $\omega_p = 0.48$, stopband edge $\omega_{s1} = 0.52$, $k_p = 1$. Filter 4: $\gamma$ is obtained by letting $\omega_{s1}$ and $\omega_{s2}$ be in the domain of $k(w)$

| filter | type | stopband attenuation | $k_{s1}$ | $k_{s2}$ | $k_{s3}$ | $k(\omega)$ |
|---|---|---|---|---|---|---|
| 1 | equiripple | 0 dB/octave | 10 | - | - | $k_{s1}$, constant for $\omega \geqslant \omega_{s1}$ |
| 2 | semi-equiripple | staircase | 10 | 100 | 1000 | $(k_{s1}$, for $\omega_{s1} \leqslant \omega < \omega_{s2}) \cup$ $(k_{s2}$, for $\omega_{s2} \leqslant \omega \leqslant \pi)$ |
| 3 | semi-equiripple | linear | 10 | 100 | 1000 | composed of two linear functions |
| 4 | semi-equiripple | $1/f^{\gamma}$ | 10 | 100 | 1000 | exponential, $\gamma \approx 5.35$ |

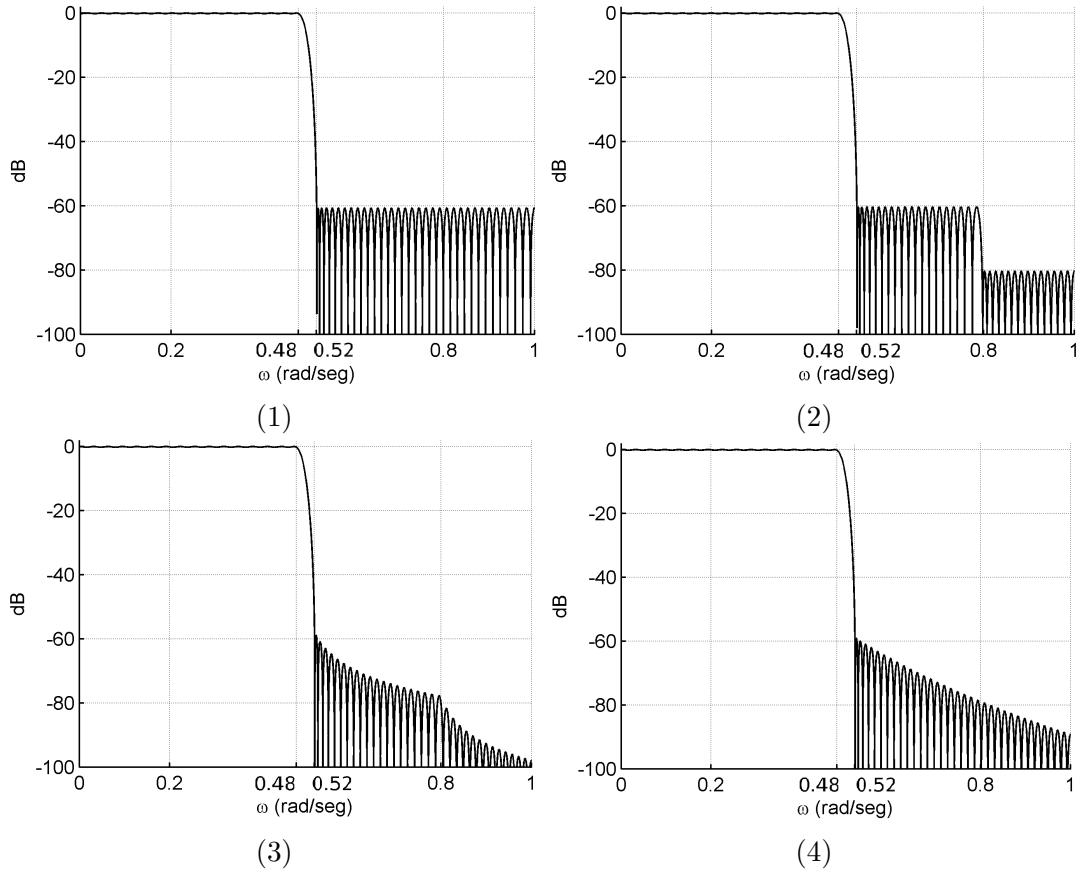


Figure 16 – Four optimal filters with different $k(\omega)$ weighting functions

The signal distortion caused by these ripples could lead to the occurrence of ISI as presented below. Let the filter response $H(e^{j\omega})$ be expressed as

$$H(e^{i\omega}) = \left|H(e^{i\omega})\right| e^{i \arg\left\{H(e^{i\omega})\right\}} = \left|H(e^{i\omega})\right| e^{-j\omega \cdot n_d}, \tag{3.12}$$

where $n_d$ is the filter group delay; $\left|H(e^{i\omega})\right|$ is the magnitude response and $\arg\{H(e^{i\omega})\}$ is the the phase response. After the convergence of Eq. (3.7), the ripple peaks are approx-

Table 3 – passband ripples for different weighting functions

| Filter | # of iterations | $\delta$ | $\|E(e^{j\omega})\|_\infty$ |
|---|---|---|---|
| 1 | 11 | 0.00844060401 | 0.00844060401 |
| 2 | 13 | 0.0086394292 | 0.0086394292 |
| 3 | 11 | 0.0117381235 | 0.0117381235 |
| 4 | 10 | 0.0110966284 | 0.0110966284 |

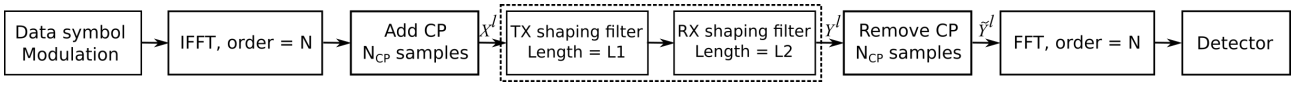


Figure 17 – Block diagram to analyse the ISI caused by shaping filters

imately uniformly spaced [27]. Therefore, the passband ripples can be modeled as a sine function as

$$H(e^{i\omega}) = [1 + |\delta|\cos(\varphi\omega)]e^{-j\omega n_d}, \text{ for } 0 \leqslant \omega \leqslant \omega_p \tag{3.13}$$

with $|\delta|$ is the maximum ripple magnitude and $\varphi$ is the frequency of such ripples expressed by

$$\varphi = \frac{2\pi \cdot n_p}{\omega_p} \tag{3.14}$$

being $n_p$ the number of cycles of ripple in the positive passband.

Let $x[n]$ be the filter input signal and $X(e^{j\omega})$ its Fourier transform. The output spectrum $Y(e^{j\omega})$, can be obtained as

$$\begin{aligned} Y\left(e^{i\omega}\right) &= H(e^{i\omega})X(e^{i\omega}) \\ &= [1 + \sigma\cos(\varphi\omega)]e^{-j\omega\cdot n_d} \cdot X(e^{j\omega}) \\ &= \left[1 + \frac{\sigma}{2}(e^{j\varphi\omega} + e^{-j\varphi\omega})\right] e^{-j\omega n_d}X(e^{j\omega}) \\ &= \frac{\sigma}{2}X(e^{j\omega})e^{-j\omega(n_d-\varphi)} + X(e^{j\omega})e^{-j\omega n_d} + \frac{\sigma}{2}X(e^{j\omega})e^{-j\omega(n_d+\varphi)}, \end{aligned}$$

that in time domain can be written as

$$y[n] = \underbrace{\frac{\sigma}{2}x[n-(n_d-\varphi)]}_{pre\ echo} + \underbrace{x[n-nd]}_{delayed\ input} + \underbrace{\frac{\sigma}{2}x[n-(n_d+\varphi)]}_{post\ echo}, \tag{3.15}$$

where $y[n]$ is composed of a main component and two echoes shifted by $\pm\varphi$ at both sides which generate interference back and forth between the symbols, i.e. ISI. The effect of filtering on the waveform can be studied by using the system shown in Fig. 17 for the transmitter and receiver connected directly without propagation channel or transmitter/receiver impairments (only one path of the transceiver in Fig. 1).

The vectors $\mathbf{X}^l$ and $\mathbf{Y}^l$ represent the filter input and output, respectively, and for analysis purposes, the transmitter and receiver filters can be considered as a single equivalent of

length $L = 2L_1 - 1$. The received $l-$th symbol is therefore given by

$$\mathbf{Y}^l = \mathbf{H}^{(0)}\mathbf{X}^l + \mathbf{H}^{(1)}\mathbf{X}^{l-1}, \tag{3.16}$$

where $\mathbf{H}^{(0)}$ and $\mathbf{H}^{(1)}$ are the Toeplitz matrices whose elements are the coefficients of the equivalent filter. Considering that the filter length is less than the OFDM symbol duration ($N_T$), ISI on the received $l$-th symbol can be due only to the $(l-1)$-th symbol and therefore, after the CP removal the $l$-th symbol can be expressed as

$$\tilde{\mathbf{Y}}^l = \begin{bmatrix} \mathbf{0}_{N\times N_{CP}} & \mathbf{I}_{N\times N} \end{bmatrix} \mathbf{H}^0\mathbf{X}^l + \begin{bmatrix} \mathbf{0}_{N\times N_{CP}} & \mathbf{I}_{N\times N} \end{bmatrix} \mathbf{H}^1\mathbf{X}^{l-1} \tag{3.17}$$

where the first term contains the three components in (3.15) and the second term is the ISI from the previous symbol. To eliminate the second term, the CP length needs to be greater than the filter order ($N_{CP} > L-1$), otherwise ISI occurs and from (3.13), minimal ISI distortions are introduced if the filter is of low order, has low frequency $\varphi$ and has small ripple amplitude $|\delta|$.

## 3.4 Filter structures and analysis of finite word length effects

This section presents filter structures of low complexity and able to manage the effects of the fixed-point quantization of both the coefficients and the internal signals.

### 3.4.1 Cascade filter

As narrower the transition band (for spectral containment), $H(z)$ will exhibit zeros highly clustered located very close to the passband edge. The quantization of the coefficients will make these zeros to experience large shifts which alters the frequency response of the filter. In addition, as more clustered zeros, the greater the quantization sensitivity of a given structure [22].

FPGAs are widely used for different signal processing tasks such as filtering and although state-of-the-art devices can support long and variable word-length datapaths, finite word-length effects can be important in filters with tight SEM specifications and long impulse responses. For this reason, it is investigated an suitable architecture for an actual implementation in these devices.

The distribution of the zeros of FIR filters in the $z$-plane is such that each complex zero out of the unit circle is part of a group of four zeros which are conjugated and reciprocal; the zeros in the unit circle occur in conjugated pairs and real zeros (on the real axis) occur in reciprocal pairs. Some proposed structures consider to distribute the zeros along multiple sections along the filter to decrease the consequent errors introduced by quantization [28]. This is the case of cascade filters which implement group of zeros in independent filter

sections, thus confining the quantization errors within each section. Further, in addition to cascade structures enable modular implementations, they can distribute the overall filter gain along the sections to control the word-length growth in the filter datapath in contrast to direct-form structures, where the gain is scaled by one single factor thus requiring more bits to prevent overflows.

### 3.4.2 Sections structures

Let the filter system function be expressed by

$$H(z) = \sum_{n=0}^{L-1} h\left[n\right] z^{-n}, \tag{3.18}$$

where $L$ is the filter length. For a type I FIR and $L = 2M + 1$, $H(z)$ can be factorized in $N_s$ $2^{nd}-$order sections as

$$H(z) = \sum_{n=0}^{2M} h\left[n\right] z^{-n} = \prod_{k=1}^{N_s} H_k(z), \tag{3.19}$$

where $H_k(z) = b_{0k} + b_{1k}z^{-1} + b_{2k}z^{-2}$ represents the $k$-th $2^{nd}$-order section with real coefficients $b_{ok}$, $b_{1k}$ and $b_{2k}$, and $N_s = \left\lfloor \frac{filter\ order}{2} \right\rfloor = M$. For a type II FIR, the factorization in Eq. (3.19) will have a single factor $H_k(z) = 1 + z^{-1}$ with a zero at $z = -1$. Type III and IV FIRs are not able to implement low-pass filter responses. Henceforth, the study is focused only in type I FIR. If this filter has a zero at $z = -1$, it always occurs with an even multiplicity and could be implemented by a $2^{nd}$-order section or by two cascaded $1^{st}$-order sections as

$$H_k(z) = (1 + z^{-1}). \tag{3.20}$$

Each section can be realized as a low-order polynomial whose roots are groups of conjugated and/or reciprocal zero pairs of $H(z)$. Some possibilities are described as follows: two complex conjugated zeros at $z_k = r_k e^{j\theta_k}$ and $z_k = r_k e^{j\theta_k}$ can be implemented by the $2^{nd}$-order section:

$$H_k(z) = (1 - r_k e^{j\theta_k} z^{-1})(1 - r_k e^{-j\theta_k} z^{-1}) = 1 - 2r_k cos\left(\theta_k\right) z^{-1} + r_k^2 z^{-2}, \tag{3.21}$$

and if these zeros are inside the unit circle, their reciprocal pair (outside the unit circle) needs to be implemented in a section using the same coefficients in order to preserve the linear phase property after quantization:

$$H_k(z) = (1 - {r_k}^{-1} e^{-j\theta_k} z^{-1})(1 - {r_k}^{-1} e^{j\theta_k} z^{-1}) = {r_k}^{-2}\left({r_k}^2 - 2r_k cos\left(\theta_k\right) z^{-1} + z^{-2}\right). \tag{3.22}$$

A pair of zeros located on the unit circle ($r_k = 1$) can be implemented by

$$H_k(z) = 1 - 2cos\left(\theta_k\right) z^{-1} + z^{-2}, \tag{3.23}$$

and reciprocal real zeros at $z_k = r_k$ and $z_k^{-1} = r_k^{-1}$ by

$$H_k(z) = (1 - r_k z^{-1})(1 - r_k^{-1} z^{-1}) = 1 - (r_k + r_k^{-1}) z^{-1} + z^{-2} \tag{3.24}$$

By implementing pairs of $2^{nd}$-order reciprocal sections in a single $4^{th}$-order section, the filter would require lesser computational resources compared to implementing them individually. In fact, other groupings can be made to reduce the computational cost [22]. Let $z_k = r_k e^{j\theta_k}$, $z_k^* = r_k e^{-j\theta_k}$, $z_k^{-1} = r_k^{-1} e^{-j\theta_k}$ and $z_k^{*^{-1}} = r_k^{-1} e^{j\theta_k}$ be a group of four conjugated reciprocal zeros (passband zeros), then the section can be given by

$$\begin{aligned} H_k &= (1 - r_k e^{j\theta_k} z^{-1})(1 - r_k e^{-j\theta_k} z^{-1})(1 - r_k^{-1} e^{-j\theta_k} z^{-1})(1 - r_k^{-1} e^{j\theta_k} z^{-1}) \\ &= 1 - 2(r_k + {r_k}^{-1}) cos(\theta_k) z^{-1} + (4cos^2(\theta_k) + {r_k}^2 + {r_k}^{-2}) z^{-2} \\ &\quad - 2(r_k + {r_k}^{-1}) cos(\theta_k) z^{-3} + z^{-4}, \end{aligned} \tag{3.25}$$

which will require three coefficients (assuming a folded-symmetric structure) instead of the sections in Eq. (3.21) and Eq. (3.22) which will require five coefficients. The above presented sections will preserve the linearity of the filter since they are symmetric.

### 3.4.3 Round-off noise analysis

Waveform samples can also experience distortions because of the quantization of internal signals (adders, multipliers and internal registers). This quantization generates round-off noise thus decreasing the SNR. The following analysis shows that this noise depends on both the quantization level applied to the signal and the above mentioned section structures. Let a sample $w$ be expressed by a two-complement number of $(1 + B_1)$ bits as

$$w = b_0 \cdot b_1 b_2 ... b_{B_1} = -b_0 + \sum_{k=1}^{B_1} b_k 2^{-k}, \tag{3.26}$$

where $\cdot$ represents the binary point, $b_0$ is the sign bit and $b_k$ are the fractional bits. If $w$ is quantized to $(1 + B)$ bits as

$$\hat{w} = Q_B\left[w\right] = b_0 \cdot b_1 b_2 ... b_B, \tag{3.27}$$

where $Q[\ ]$ represents a non-linear operation of quantization, then the error $e_w$ ($e_w = \hat{w} - w$) is such that $-\frac{\Delta}{2} < e_w \leqslant \frac{\Delta}{2}$, being $\Delta$ the quantization step expressed by

$$\Delta = 2^{-B} \tag{3.28}$$

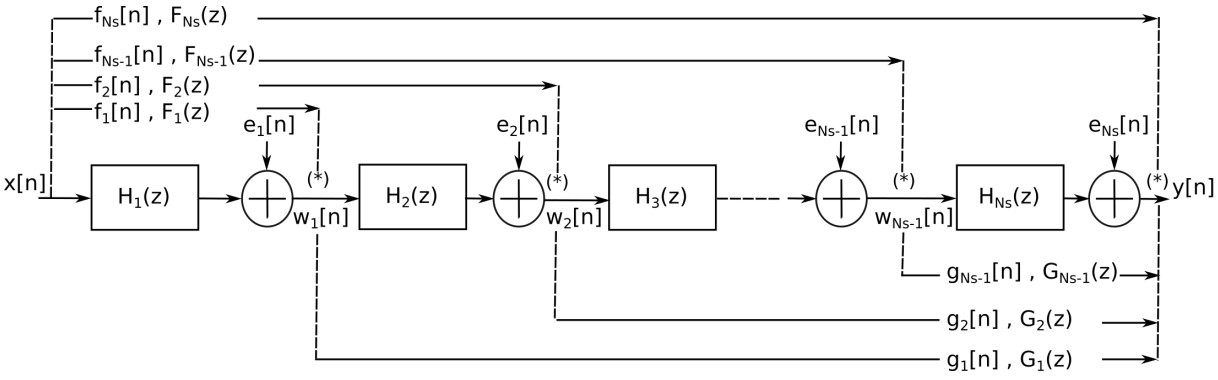


Figure 18 – Lineal model of a cascade FIR filter

If each quantization error is represented by a wide-sense stationary white-noise with uniform distribution over $\Delta$ and is independent of the input, its statistics can be expressed by:

$$\text{mean: } m_e = 0 \tag{3.29a}$$

$$\text{variance:} {\sigma_e}^2 = \frac{\Delta^2}{12} \tag{3.29b}$$

$$\text{autocorrelation: } \phi_{ee}[m] = {\sigma_e}^2 \delta[m] \text{ , with m} \in \mathbb{Z} \tag{3.29c}$$

$$\text{power spectrum density: } \Phi_{ee}(e^{j\omega}) = \sum_{m=-\infty}^{\infty} \phi_{ee}[m] e^{-j\omega m}$$

$$= {\sigma_e}^2 \text{ , for } |\omega| \leqslant \pi \tag{3.29d}$$

However, the effect of quantization $Q[\,]$ (truncation or rounding) of any internal sample can be linearized by replacing $Q[\,]$ by the sum between the original sample and the error (noise) that is produced [28]. Thus, a cascade structure of $N_s$ sections can be represented by the linearized model shown in Fig. 18, where $H_k(z)$ is the $Z-$transform of the impulse response $h_k[n]$ of the section $k$; and $f_k[n]$ and $g_k[n]$ are the impulse responses of the equivalent filters indicated in the figure, such that $f_k[n] = h_1[n] * h_2[n] ... * h_k[n]$ and $g_k[n] = h_{k+1}[n] * h_{k+2}[n] ... * h_{Ns}[n]$ whose respective transforms are denoted as $F_k(z)$ and $G_k(z)$. The equivalent filter $G_k$ can be expressed as

$$G_k(z) = \begin{cases} \prod_{i=k+1}^{N_s} H_i(z) & 0 \leqslant k \leqslant N_s - 1 \\ 1 & k = N_s \end{cases} \tag{3.30a}$$

$$G_k(z) = \sum_n g_k[n] z^{-n}. \tag{3.30b}$$

.

In Fig. 18, it has been considered that the noise sources in each section were summed. This sum is represented by an equivalent noise $e_k$ and injected to the respective section

output (nodes marked with asterisk). Thus, the variance of $e_k$ is given by

$$\sigma_k{}^2 = \mathrm{VAR}(e_k[n]) = M_k \frac{\Delta^2}{12} \text{ , for } k = 1, 2, ..., Ns, \tag{3.31}$$

where $M_k$ is the number of noise sources in section $k$. Each noise $e_k$ is filtered by a filter $g_k$ resulting in an output noise $e_{ok}$ expressed by

$$e_{ok}[n] = \sum_{m=-\infty}^{\infty} e_k\left[n-m\right] g_k[m], \tag{3.32}$$

whose variance is therefore

$$\sigma_{ok}{}^2 = \mathrm{VAR}(e_{ok}[n]) = \sigma_k{}^2 \sum_{n=-\infty}^{\infty} \left(g_k{}^2[n]\right). \tag{3.33}$$

Since the system model is linear, the total output round-off noise ($e_o$) can be expressed as

$$e_o[n] = \sum_{k=1}^{N_s} \left(e_{ok}[n]\right) = \sum_{k=1}^{N_s} \sum_{m=-\infty}^{\infty} \left(e_k\left[n-m\right] g_k\left[m\right]\right) \tag{3.34}$$

and its variance ($\sigma_o{}^2$) as

$$\begin{aligned} \sigma_o{}^2 = VAR(e_o[n]) &= \sum_{k=1}^{N_s} \sigma_{ok}{}^2 = \sum_{k=1}^{N_s} \sigma_k{}^2 \sum_{n=-\infty}^{\infty} \left(g_k{}^2[n]\right) \\ &= \frac{2^{-2B}}{12} \sum_{k=1}^{N_s} M_k \sum_{n=-\infty}^{\infty} \left(g_k{}^2[n]\right). \end{aligned} \tag{3.35}$$

From Eq. (3.35), the output noise could be reduced : 1) by using a symmetric folded configuration in each section which halves $M_k$ and therefore the noise power; 2) by ordering properly the sections of filters $g_k$ since different orderings produce different filter responses to filter $e_k$; 3) by increasing the internal word length of the sections in accordance with a required SNR.

### 3.4.4 Section scaling

The round-off noise in an actual filter implementation needs to be constrained in order to meet a required SNR. And also, it is necessary to scale in some way the internal operations results to avoid overflows. However it needs to be done without affecting the signal dynamic range. Some methods for scaling IIR and FIR cascade structures constrained to a fixed dynamic range were initially studied in [29, 28]. From these works, optimal scale factors can be obtained as follows.

The scaling operation can be introduced by expressing the filter in Eq. (3.19) in terms of its component sections as

$$H(z) = \prod_{k=1}^{Ns} s_k H_k(z), \tag{3.36}$$

where $s_k$ are the scaling factors inserted along the structure such that

$$\prod_{k=1}^{Ns} s_k = 1 \tag{3.37}$$

in order to preserve the filter overall gain. From Fig. 18, the equivalent filter between the first and $k-$th sections is denoted by $F_k(z)$ given by

$$\text{non-scaled form:} \quad F_k(z) = \prod_{i=1}^{k} H_i(z) = \sum_n f_k\,(n) z^{-n} \quad \text{and,} \tag{3.38}$$

$$\text{scaled form:} \quad \bar{F}_k(z) = \prod_{i=1}^{k} s_i H_i(z) = \sum_n \bar{f}_k\,(n) z^{-n}, \tag{3.39}$$

where $f_k\,(n)$ and $\bar{f}_k\,(n)$ are their respective impulse responses relating each other by

$$\bar{f}_k(n) = f_k(n) \cdot \prod_{i=1}^{k} s_i \tag{3.40}$$

In order to avoid overflows, the section outputs $(w_k)$ should be such that

$$|w_k[n]| \leqslant 1 \text{ for } k = 1, 2, ..., (N_s - 1), \tag{3.41}$$

also, since $w_k[n] = x[n] * \bar{f}_k[n]$, then

$$|w_k[n]| \leqslant \sum_m |x[n-m]|\,\left|\bar{f}_k(m)\right|. \tag{3.42}$$

and for an input signal $x[n]$ with $|x[n]| \leqslant 1$ (worst non-overflow condition), Eq. (3.41) implies that:

$$\sum_n \left|\bar{f}_k(n)\right| \leqslant 1. \tag{3.43}$$

So, if the maximum value of $\bar{f}_k(n)$ in Eq. (3.43) is chosen (to maximize $\prod_{i=1}^{k} s_i$ and consequently the dynamic range) and from Eq. (3.40), the scaling factors, which are named sum scaling factors here, are given by

$$\prod_{i=1}^{k} s_i = \left[\sum_n |f_k[n]|\right]^{-1}, \tag{3.44}$$

or equivalently by

$$s_k = \begin{cases} 1/c_1 & k = 1 \\ 1 \Big/ \prod_{i=1}^{k-1} s_i c_k & k = 2, 3, ..., (N_s - 1) \\ 1 \Big/ \prod_{i=1}^{k-1} s_i & k = N_s \\ 1 \Big/ \prod_{i=1}^{k-1} s_i c_k & k = N_s\,(\dagger)\,, \end{cases} \tag{3.45}$$

where $c_k = \sum_n |f_k[n]|$ for $k = 1, 2, ..., Ns$ and $\dagger$ represents the case when the last factor ($s_{Ns}$) scales the overall gain to avoid overflows at the filter output (i.e. to meet the condition $|y[n]| \leqslant 1$). These scaling factors (except $\dagger$) do not modify the overall filter gain but distribute it to the sections to avoid internal overflows and maximize the dynamic range in each section.

In addition, if $w_k$ is expressed by its frequency response, we have

$$\begin{aligned} |w_k\,[n]| &= \left| \frac{1}{2\pi} \int_{-\pi}^{\pi} X\left(e^{j\omega}\right) \bar{F}_k\left(e^{j\omega}\right) e^{j\omega n} d\omega \right| \\ &\leqslant \frac{1}{2\pi} \int_{-\pi}^{\pi} \left|X\left(e^{j\omega}\right)\right| \cdot \left|\bar{F}_k\left(e^{j\omega}\right)\right| d\omega = \left\|X\left(e^{j\omega}\right) \bar{F}_k\left(e^{j\omega}\right)\right\|_1 \\ &\leqslant \left\|X\left(e^{j\omega}\right)\right\|_p \left\|\bar{F}_k\left(e^{j\omega}\right)\right\|_q \;\text{ if }\; p, q \geqslant 1 \text{ and } \frac{1}{p} + \frac{1}{q} = 1, \end{aligned} \tag{3.46}$$

Thus, for an input signal $x[n]$ such that $\|X(e^{j\omega})\|_p \leqslant 1$, i.e.

$$\left[\frac{1}{2\pi} \int_{-\pi}^{\pi} \left|X\left(e^{j\omega}\right)\right|^p d\omega\right]^{1/p} \leqslant 1 \quad \text{for } 1 \leqslant p \leqslant \infty, \tag{3.47}$$

overflows will not occur (Eq. (3.41)) if

$$\left\|\bar{F}_k(e^{j\omega})\right\|_q \leqslant 1 \tag{3.48}$$

Assuming the maximum value of $\bar{F}_k(e^{j\omega})$ in Eq. (3.48) (worst case), and from Eq. (3.40), a second set of scaling factors (norm scaling factors) is obtained and given by

$$\prod_{i=1}^{k} s_i = \left\|F_k\left(e^{j\omega}\right)\right\|_q^{-1} \;\text{ where, }\; q = \frac{p}{p-1}. \tag{3.49}$$

Thus, for $p = 1$, Eq. (3.49) can be expressed in terms of the $L_\infty-$norm of $F_k\left(e^{j\omega}\right)$ as

$$\begin{aligned} \prod_{i=1}^{k} s_i &= \left\|F_k\left(e^{j\omega}\right)\right\|_\infty^{-1} \\ &= \left[\max_{-\pi \leqslant \omega \leqslant \pi} \left|F_k(e^{j\omega})\right|\right]^{-1}, \end{aligned} \tag{3.50}$$

so the scaling factors are given by Eq. (3.45) with $c_k = \max_{-\pi \leqslant \omega \leqslant \pi} |F_k(e^{j\omega})|$.

And for $p = 2$, Eq. (3.49) can be expressed in terms of the $L_2-$norm of $F_k\left(e^{j\omega}\right)$ as

$$\begin{aligned} \prod_{i=1}^{k} s_i &= \left\| F_k\left(e^{j\omega}\right) \right\|_2^{-1} \\ &= \left[ \frac{1}{2\pi} \int_{-\pi}^{\pi} {F_k}^2(e^{j\omega}) d\omega \right]^{-1/2} \\ &= \left[ \sum_n {f_k}^2[n] \right]^{-1/2}, \end{aligned} \tag{3.51}$$

so the scaling factors are also given by Eq. (3.45) but with $c_k = \sqrt{\sum_n {f_k}^2[n]}$.

Since $x[n]$ is more constrained by the condition $|x\,[n]| \leqslant 1$ than by $\|X(e^{j\omega})\|_p \leqslant 1$, the internal signals of sum-scaled structures have limited dynamic range compared to $L_p$-norm scaled structures. Then, the former scaling generates greater levels of round-off noise. Relaxing the constraints for the internal signals could cause overflows, however it can decrease the noise thus obtaining better SNRs.

Different filter structures with scaling are analyzed in terms of their round-off noise and operation at high speed. Fig. 19a shows the model of a direct-form filter with symmetric folded configuration of coefficients: $b_0, b_1, ..., b_M$ and Fig. 19b shows its cascade structure version composed of $2^{nd}-$order scaled sections with coefficients: $b_{0k}, b_{1k}, b_{2k}$, where $k$ is the number of section, $s_k$ are the scaling factors and $s_0$ is the overall gain. Also, $f_k[n]$, $g_k[n]$, $F_k(z)$ and $G_k(z)$ are the equivalent filters where the bar over them indicates they are scaled.

In the direct-form structure, the word-length increases after each quantization of a product or addition along the bottom path. These quantizations can be replaced by noise sources which are then summed, resulting in a single noise (unfiltered) at the filter output. In contrast, cascade structures control the word-length growth by means of the factors $s_k$ and, thus the noise sources in each section can be filtered by the subsequent equivalent filters. However, they could be amplified if the sections are not properly sequenced.

From Eq. (3.35), the output noise variance of the cascade structures are

$${\sigma_{oc}}^2 = \sum_{k=1}^{Ns} {\sigma_{ok}}^2 = 3{\sigma_e}^2 \sum_{k=1}^{Ns} \sum_n {g_k}^2[n] \quad : \text{non-scaled} \tag{3.52a}$$

$$\bar{\sigma}_{oc}^2 = \sum_{k=1}^{Ns} \bar{\sigma}_{ok}^2 = 3{\sigma_e}^2 \sum_{k=1}^{Ns} \sum_n \bar{g}_k^2[n] \quad : \text{scaled} \tag{3.52b}$$

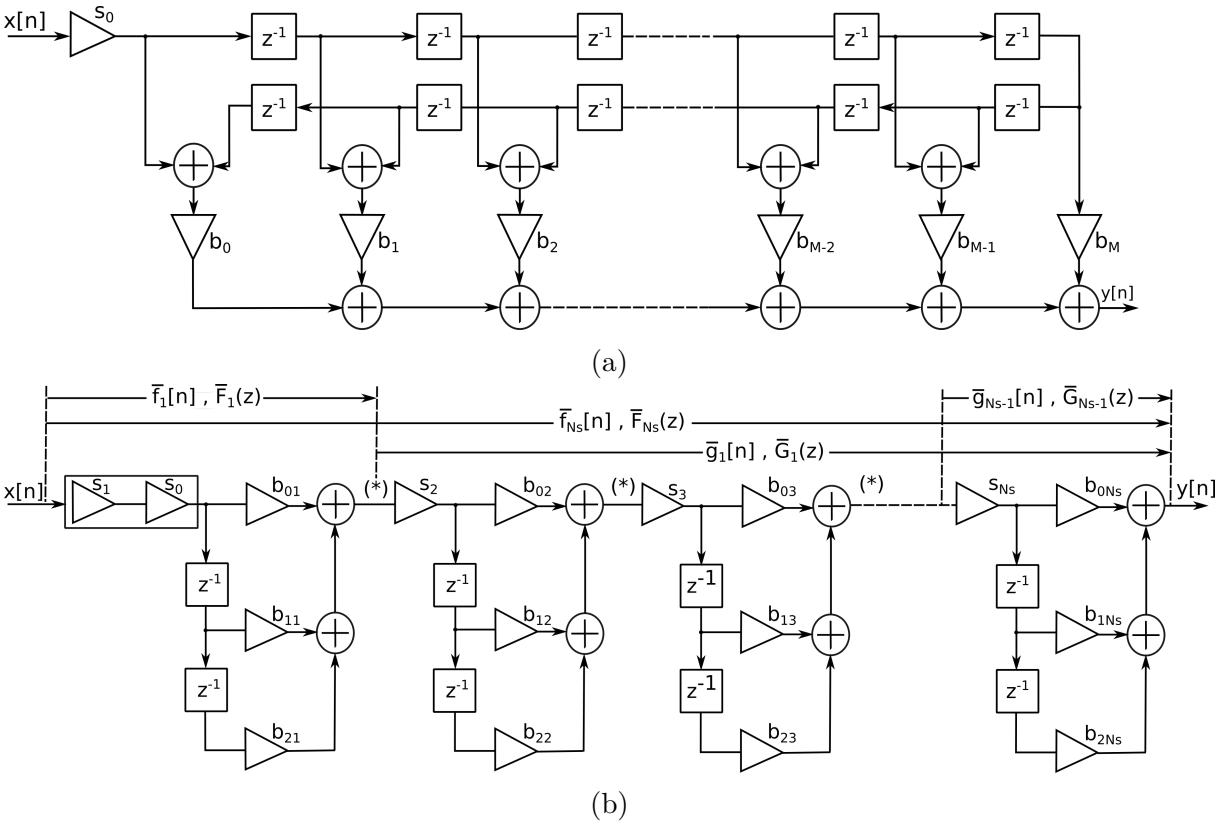


Figure 19 – Models of FIR filter structure. a) direct-form filter of order $2M$, symmetric, with $M+1$ folded coefficients. b) cascade filter with $N_s = M$ sections of $2^{nd}-$order and scaling factors $s_k$, $k = 1, 2, ..., N_s$

where ${\sigma_e}^2 = 2^{-2B}/12$, while the output noise variance of the direct-form structure is

$$ {\sigma_{od}}^2 = (M+1){\sigma_e}^2 \tag{3.53} $$

From Eq. (3.52b), it can be noted that the output noise in Fig. 19b can be reduced by reducing the noise of each section. This can be possible by using some of the two alternative structure configurations shown in Fig. 20.

The noise contributions of these configurations to the output noise are given by

$$ \bar{\sigma}^2_{oa} = 3{\sigma_e}^2 \sum_n \bar{g}^2_k[n] \quad : \text{configuration a.} \tag{3.54a} $$

$$ \bar{\sigma}^2_{ob} = 2{\sigma_e}^2 \sum_n \bar{g}^2_k[n] + {\sigma_e}^2 \sum_n \left( \frac{\bar{g}_{k-1}[n]}{s_k b_{0k}} \right)^2 \quad : \text{configuration b .} \tag{3.54b} $$

Hence, the choice of a configuration depends on which generates less noise, i.e., configuration 20a might be preferred if the following condition is satisfied:

$$ \sum_n \bar{g}^2_k[n] \leqslant \sum_n \left( \frac{\bar{g}_{k-1}[n]}{s_k b_{0k}} \right)^2. \tag{3.55} $$

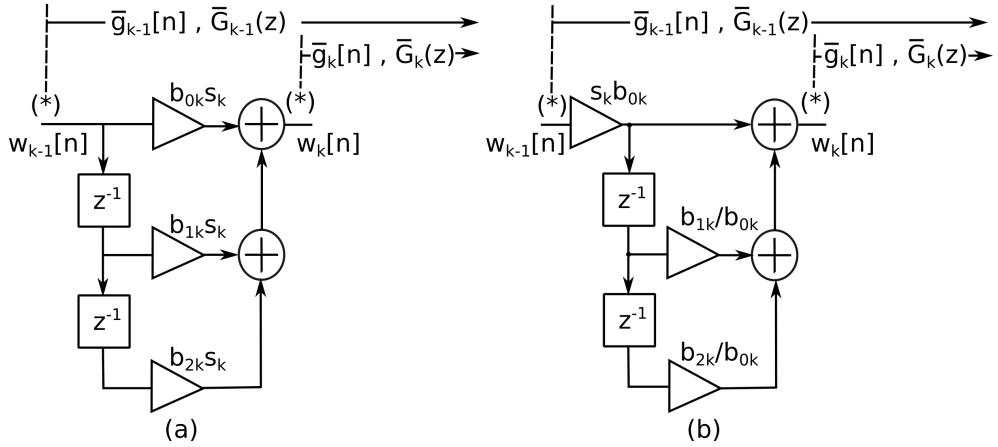


Figure 20 – Configurations of a $2^{nd}-$order section with different round-off noise levels: a) the scaling factor is included in the coefficients, b) one of the coefficients is factorized.

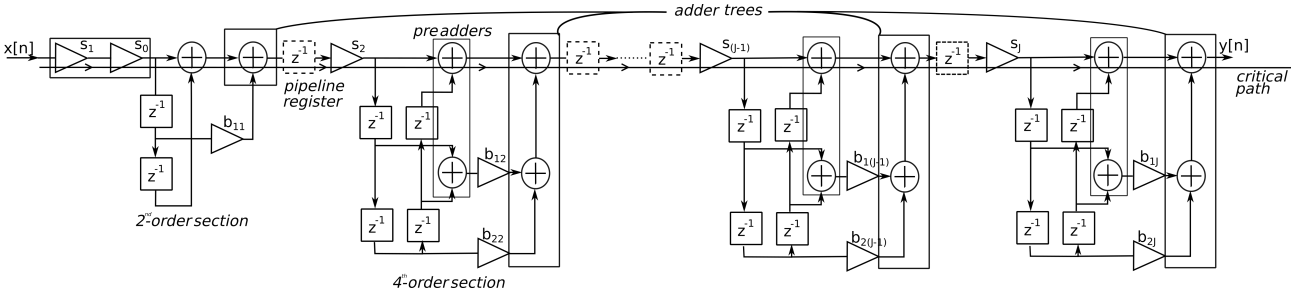


Figure 21 – Model of a cascade filter structure composed of $2^{nd}$ and $4^{th}$-order sections. Number of sections = $J$, pipelined, scaled, symmetric, direct-form sections.

In order to decrease the number of multipliers, the zeros can be realized by symmetric $4^{th}-$order sections as is shown in Fig. 21 which requires only one multiplier per section. Real zeros and complex zeros on the unit circle, can be implemented by single $2^{nd}-$order sections.

Since the $4^{th}$-order sections in Fig. 21 and the $2^{nd}$-order sections in Fig. 20, have similar structures, the condition Eq. (3.55) can be used to evaluate which factors $s_k$ can be implemented inside or outside of the sections in order to reduce the output noise.

From the point of view of speed and timing considerations, the adder trees at the top of the structure in Fig.21, form a critical path (horizontal trace) which is longer as the number of sections increases. This critical path can be shortened by inserting pipeline registers. However, since this increases the latency as well, there is a trade-off between latency and speed. Other way to reduce the time bottleneck of the adder trees is to replace each section by its transposed form as shown in Fig. 22. In this case, the additions in each section are buffered, i.e., the structure is self-pipelined, then there are not problematic critical paths and the pipeline registers are not necessary.

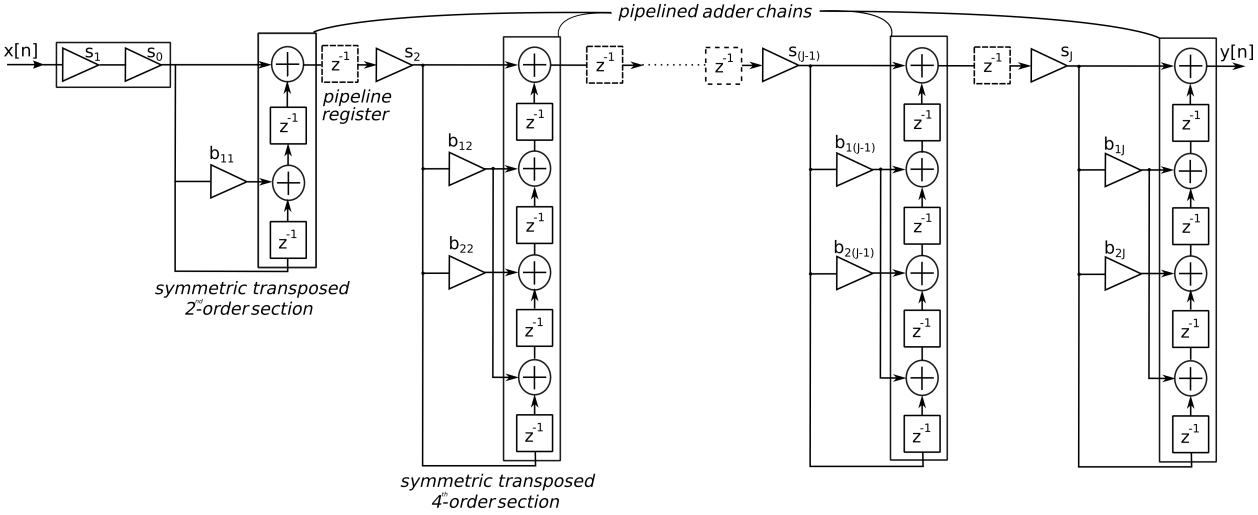


Figure 22 – Model of a self-pipelined cascade filter structure composed of scaled, symmetric, transposed direct-form sections of $2^{nd}$ and $4^{th}$-order, number of sections $= J$

### 3.4.5 Filter structures suitable for FPGA implementation

FPGA devices are widely used in tasks with high computational demands, as for example, filtering in software defined radios. This subsection is dedicated to explore a modification of the above filter structure in order to exploit the dedicated digital signal processing (DSP) units inside a FPGA.

In the structure shown in Fig. 22, the fan-out capacity of logic gates might be exceeded as the section input signals are supplied to all multipliers simultaneously. The systolic filter structure presented below aims to solve this inconvenience.

The **Systolic FIR** is a structure that inserts pipeline registers both in the input signal and the adder paths as is shown in Fig. 23. By considering an additional delay of $N = 2M$ samples, the system function of a type I FIR filter in Eq. (3.19), can be re-expressed as

$$\begin{aligned} H_D(z) &= z^{-N} \sum_{n=0}^{N} h[n] z^{-n} \\ &= \sum_{n=0}^{N} z^{-2n} h[n] z^{n-N}, \end{aligned} \tag{3.56}$$

where $N$ is the filter order, the delay blocks $z^{-2n}$ register the input samples (pipeline in the top path) and the blocks $z^{n-N}$ register the adder outputs (pipeline in the bottom path). This structure requires both delay chains for the synchronization of the input samples of the adders.

Moreover, if the symmetric coefficients are rearranged in a folded configuration, both the number of multipliers and the additional delay can be halved as shown in Fig. 24.

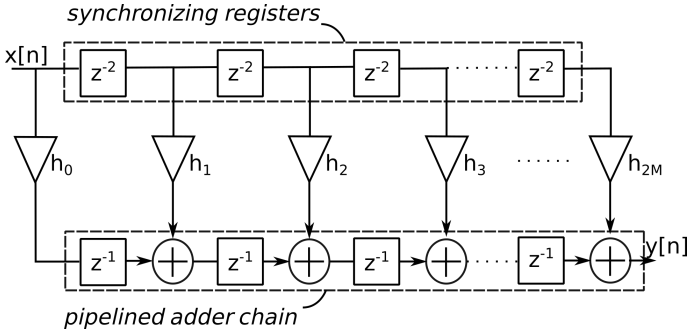


Figure 23 – Systolic FIR filter structure, filter length $= 2M + 1$, number of multipliers $= 2M$, filter delay $= (\frac{\text{filter}}{2} + 2M) = 3M$.

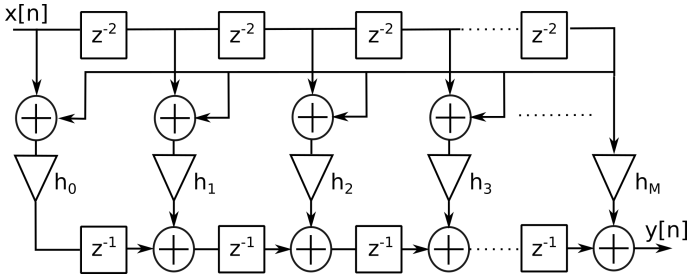


Figure 24 – Systolic FIR filter structure with folded-symmetric configuration, filter length $= 2M + 1$, number of multipliers $= M$, filter delay $= (\frac{\text{filter}}{2} + M) = 2M$.

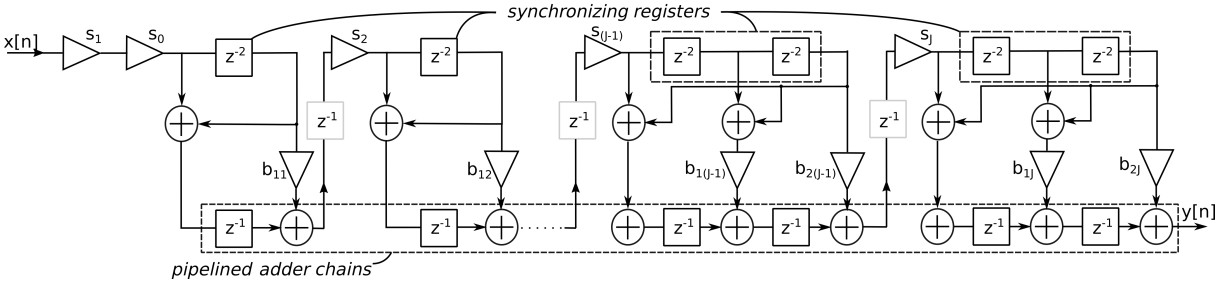


Figure 25 – Model of a cascade filter structure with systolic sections. $2^{nd}$ and $4^{th}$-order scaled sections are used as example, number of sections $= J$, inter-section delays are optional.

The fan-out related problems of the cascade filter in Fig. 21 are avoided by implementing the sections in systolic symmetric structures because each section input signal is multiplied with only a few coefficients. The proposed architecture is shown in Fig. 25.

This structure can be implemented in the DSP units (slices) of a FPGA device. For example, each DSP slice of the FPGA described in [30] is composed of one adder and one multiplier with embedded pipeline, a multi-functional ALU for arithmetic and bit-wise logic operations, internal multiplexers for reconfigurable routing and a pipeline chain at the input of the slice. Thus, several slices can be cascaded to implement the overall structure as is shown in Fig. 25. The multiplication of a sample with a filter coefficient is realized in each slice. The coefficients are inserted in the ports $A$ of the slices. When

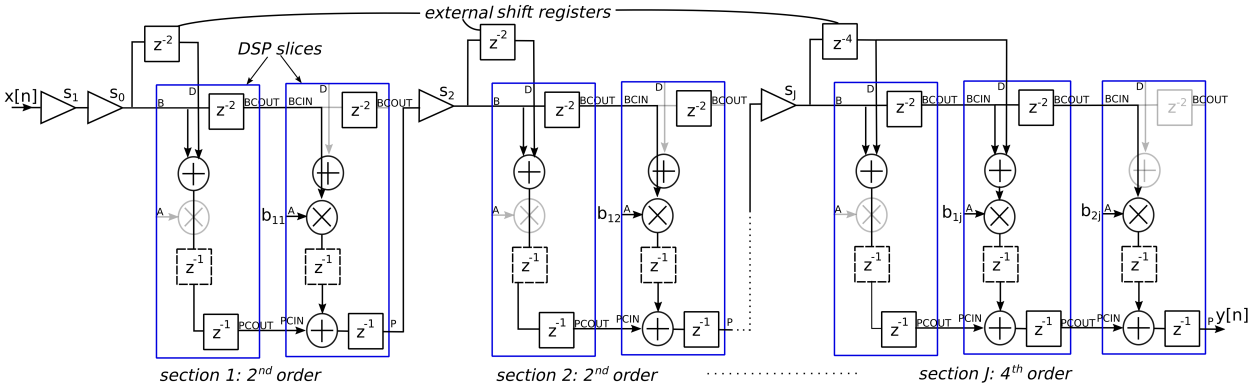


Figure 26 – Cascade filter structure with systolic sections implemented in FPGA DSP slices. $2^{nd}$ and $4^{th}$−order scaled sections are used as example, number of sections $= J$, pipeline registers (dashed) are optional, slices are marked in blue and unused elements in the slice appear shaded

a coefficient is one, the multiplier can be deactivated to save power. The DSP slices, which are marked in blue, can be cascaded using the dedicated interfaces *BCIN*, *BCOUT*, *PCIN* and *PCOUT* to implement sections of any order. Two pipeline chains are used in each section. The first is at the top of the section and is composed of synchronization registers (within the section) which pass the input samples through the ports *BCOUT* and *BCIN*. The second pipeline is at the bottom of the sections, accumulates the additions and interfaces to the next slice through the ports *PCOUT* and *PCIN*. The output of a section is passed to the next through ports $P$ and $B$. Since the number of slices per section can be variable, the folded pipeline paths at the top of the sections are implemented using shift registers outside the sections and routed to the $D$ ports.

## 3.5 Performance analysis

In the previous chapter, it has been shown by simulation that the OOBE of the transmitter and ACI of the receiver can be reduced by shaping the symbol edges with smooth functions. In this chapter, pulse shaping filters with arbitrary stopband response were designed in order to contain the OOBE and thus the ISBI. The performance of the proposed filters is evaluated in terms of: 1) the reduction of the OOBE and ability to meet tight SEM specifications. 2) The ISI caused by the echoes, which are related to the passband ripples and the outlier samples of the impulse responses. The outlier samples of windowed truncated *sinc*, equiripple and semi-equiripple filters are compared. 3) The effect of the filter delay on the SIR and EVM is evaluated by using a link-level ISDB-T transmission model. 4) The BER improvement when the filters are used in a filtered-OFDM transceiver (Fig. 1) to filter the OOBE of different services. In this last case, the transceiver is simulated with two asynchronous services running in parallel each with different parameters and using the resource grid structure of LTE.

Table 4 – Spectrum mask for ISDB-T defined in Brazil ABNT NBR 15601

| Minimum attenuation in relation to average power measured at carrier central frequency | | | |
|---|---|---|---|
| Frequency separation from the main carrier (MHz) | non-critical mask (dB) | sub-critical mask (dB) | critical mask (dB) |
| ± 2.79 | 0 | 0 | 0 |
| ± 2.86 | 20.0 | 20.0 | 20.0 |
| ± 3.00 | 27.0 | 34.0 | 34.0 |
| ± 3.15 | 36.0 | 43.0 | 50.0 |
| ± 4.5 | 53.0 | 60.0 | 67.0 |
| ± 9.0 | 83.0 | 90.0 | 97.0 |
| ± 15.0 | 83.0 | 90.0 | 97.0 |

From the point of view of a real implementation, the quantization noise of the proposed filter structure is evaluated for the scaling methods studied in section 3.4.4 and different sequencing of sections.

### Considered ISDB-T OFDM waveform for analysis (single service)

A brief description of the ISDB-T waveform used in this analysis is as follows: the bandwidth is of 6-MHz and composed of 13 segments of subcarriers organized in three subbands called layers A, B and C, which are transmitted simultaneously. The configuration of the data modulation type, convolutional inner code rate, time interleaving depth and number of segments can be different for each layer. Three operation modes are defined: 1, 2 and 3 with FFT orders: 2048, 4096 and 8192, respectively. The sampling frequency is 512/13 MHz and unlike LTE, it is the same for the three modes, thus there are defined three symbol lengths. Only the transmission modes 1 and 2 are considered in this analysis, with data modulation QPSK in layer A, 64-QAM in layer B and 16-QAM in layer C. In mode 1, the useful symbol duration $T_N$ is 252 $\mu$s, the active bandwidth is of 5.575 MHz and there are 96 data subcarriers and 12 pilots per segment while in mode 2, $T_N$ is 504 $\mu$s, the bandwidth is of 5.573 MHz and there are 192 data subcarriers and 18 pilots per segment. ISDB-T also defines four CP lengths: 1/4, 1/8, 1/16 and 1/32. These CP lengths correspond, respectively, to 512, 256, 128 and 64 samples in mode 1, and to 1024, 512, 256 and 128 samples in mode 2.

## 3.5.1 Spectral mask compliance

The **spectral emission mask** (SEM) specification for ISDB-T is shown in table 4 [23]. Three mask types, namely non-critical, sub-critical and critical, are specified to limit the interference between adjacent 6-MHz channels.

The **integrated sidelobe level** (ISL) is used to compare the reduction of OOBE obtained with the different filters. It expresses the relation between spectrum contents in the filter passband and stopband and can be expressed as

$$\mathrm{ISL_h} = 10 \cdot \log_{10} \left( \frac{\int_{\omega_s}^{\pi} |H(e^{j\omega})|\, d\omega}{\int_{0}^{\omega_p} |H(e^{j\omega})|\, d\omega} \right) \mathrm{dB}, \tag{3.57}$$

where $H(e^{j\omega})$ is the filter frequency response, $\omega_p$ is the passband edge frequency and $\omega_s$ is the stopband edge frequency.

#### Filter characteristics

Two semi-equiripple FIR filters were designed to meet the critical SEM. They employ linear and exponential weighing functions $W(e^{i\omega})$ to shape the stopband as is shown in Fig. 27. The filter with linearly decreasing stopband attenuation (Fig. 27a) has an ISL = -56.9 dB while the filter with exponential attenuation (Fig. 27b) has an ISL = -59.9 dB.

Furthermore, the locations of zeros of both filters are similar, as can be seen in the zero-pole diagram in Fig. 28. The groups of four complex conjugated zeros outside the unit circle produce the equiripple behavior of the filter passband and the zeros on the unit circle shape the stopband with severe attenuation since these zeros are very close to each other, which in turn increases the coefficient quantization sensitivity. Thus, in order to diminish this sensitivity, groups of four passband zeros can be realized independently in $4^{th}-$order sections, and the real zero pairs at $\omega = 0$ and $\omega = \pi$, in $2^{nd}-$order sections.

The reduction of OOBE of the transmit signal using the second filter (Fig. 27b) is shown in Fig. 29.

### 3.5.2 ISI analysis

#### Echo components caused by passband ripples

The replicas of the transmitted signal caused by filter passband ripples are simulated to analyse its contribution to ISI using the transmission model shown in Fig. 17. From section 3.3, a filtered signal is composed of one main component delayed by $n_d$ samples from the input and two echoes at both sides delayed by additional $\pm\varphi$ samples. For the filter $(b)$ in Fig. 27, filter delay $n_d = 73$, ripple frequency $\varphi = 70$ and the ripple peak $\delta = 0.05$. Two test signals are used to depict the ISI caused by the passband ripples of transmit filter. The first is a signal composed of two consecutive symbols given by third-band Nyquist pulses as is shown at the top of Fig. 30. The pre and post output echoes (bottom) are obtained by subtracting the input signal from the output signal. As can be seen, the echoes appear $\pm\varphi$ samples away from its respective main component and their peak samples are attenuated to $\frac{\delta}{2} = 0.025$ as obtained in Eq. (3.15). Observe also that,

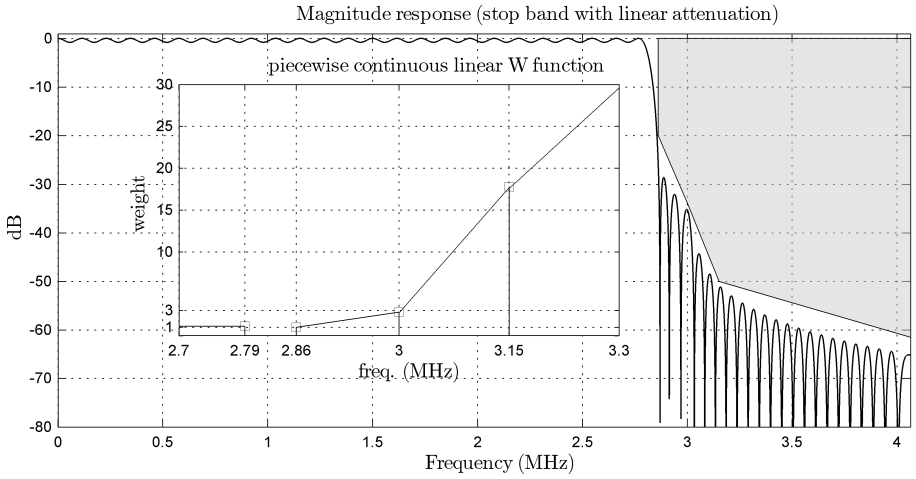


(a)

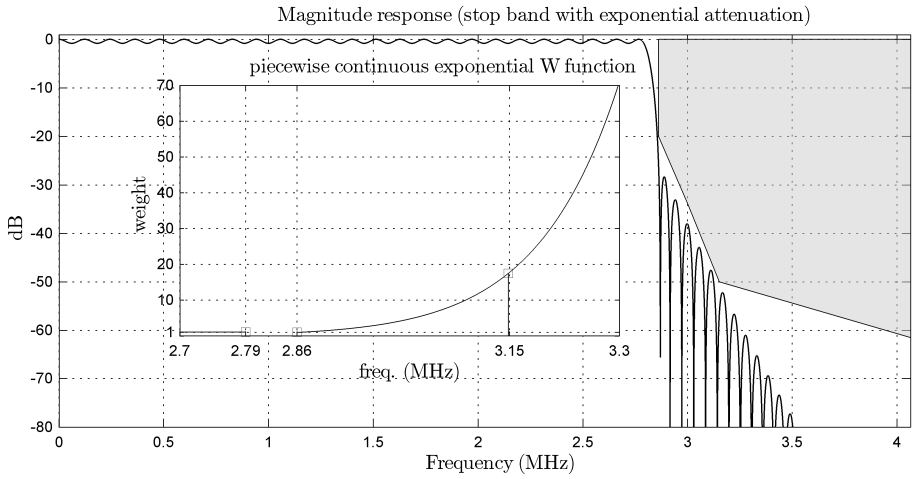


(b)

Figure 27 – Frequency response of two shaping filters meeting the ISDB-T critical SEM specification: a) filter with linearly attenuated stopband, $\delta = 5\%$ and order = 142, b) filter with exponentially attenuated stopband, $\delta = 5\%$ and order = 146. An additional attenuation of 5 dB at the stopband edge $w_s$ is added in both filters.

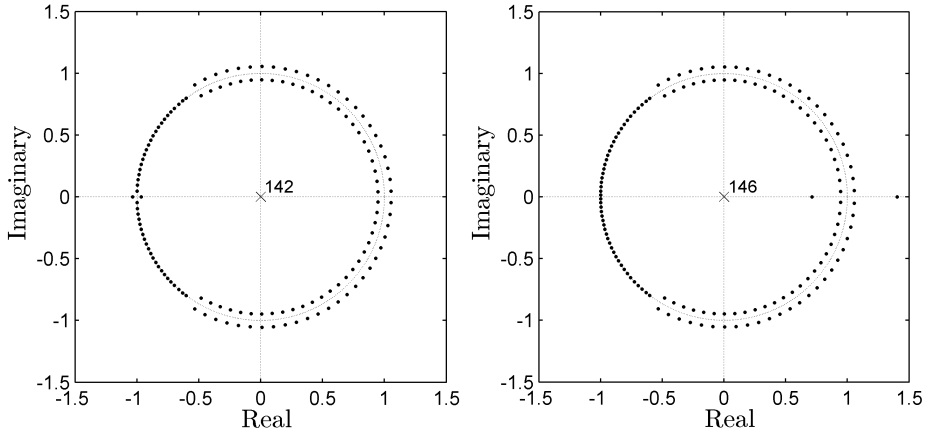


(a) lineal attenuation (b) exponential attenuation

Figure 28 – Zero-pole diagrams of the semi-equiripple pulse shaping filters

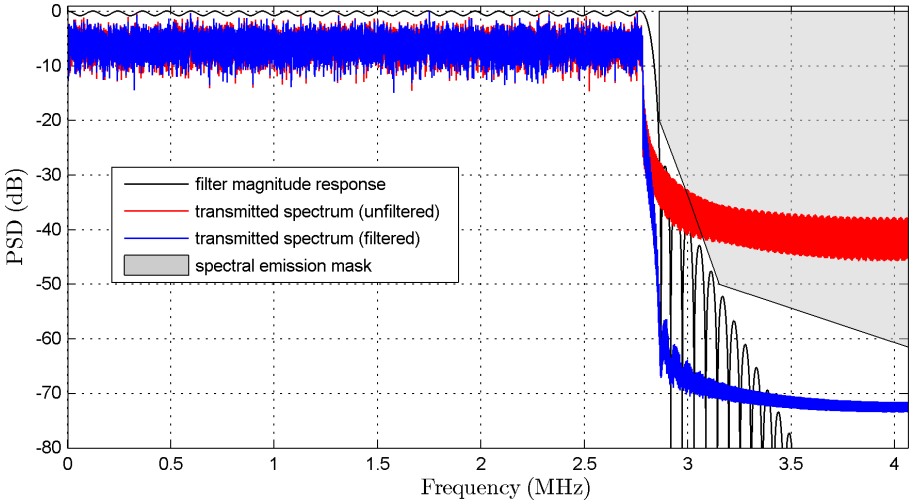


Figure 29 – Spectrum of a transmit ISDB-T waveform using a pulse shaping filter with exponentially decreasing stopband attenuation. Burst sequences of 100 symbols are transmitted in mode 1, and 1004 subcarriers out of all 2048 are active per symbol.

due to echo dispersion, the energy spreads along the adjacent symbols in both forward and backward directions creating ISI.

Another signal used for test is a composite of two conventional CP-OFDM symbols shown at the top of Fig. 31. Because the overlapped echo samples add up, they appear with amplitude peaks slightly larger than $\frac{\delta}{2}$. And also, the spike sample at $n = 2184$ points out the discontinuity at symbol boundaries. Since the CP is not long enough to absorb the filter delay spread, the dispersed samples of a symbol fall into the first $(L-1-N_{CP} = 82)$ useful samples of the following symbol and an extension of CP might be necessary to eliminate the ISI.

### Outlier samples of the filter impulse response

The attenuation rate of the Fourier transform of a function depends on the quantity of continuous derivatives $(p-1)$ has its time-domain equivalent which can be expressed as [31]

$$\text{attenuation rate} = \frac{1}{f^{(p+1)}} \tag{3.58}$$

Since a filter impulse response can be represented by a function, equiripple filters which exhibit constant level spectral sidelobes (attenuation rate $= \frac{1}{f^0}$) have $p = -1$. This means that the function (discontinuous) has a continuous double integral and therefore unit impulses thus leading to the generation of outlier samples in the tails of the impulse response. On the other hand, the semi-equiripple filters with faster attenuation addressed in section 3.2.2, for instance, the filter in Fig. 27(b) with $\gamma = 29.8$ and stopband attenuation with exponential decay, have impulse responses smoother than those of equiripple filters and thus smaller outlier samples.

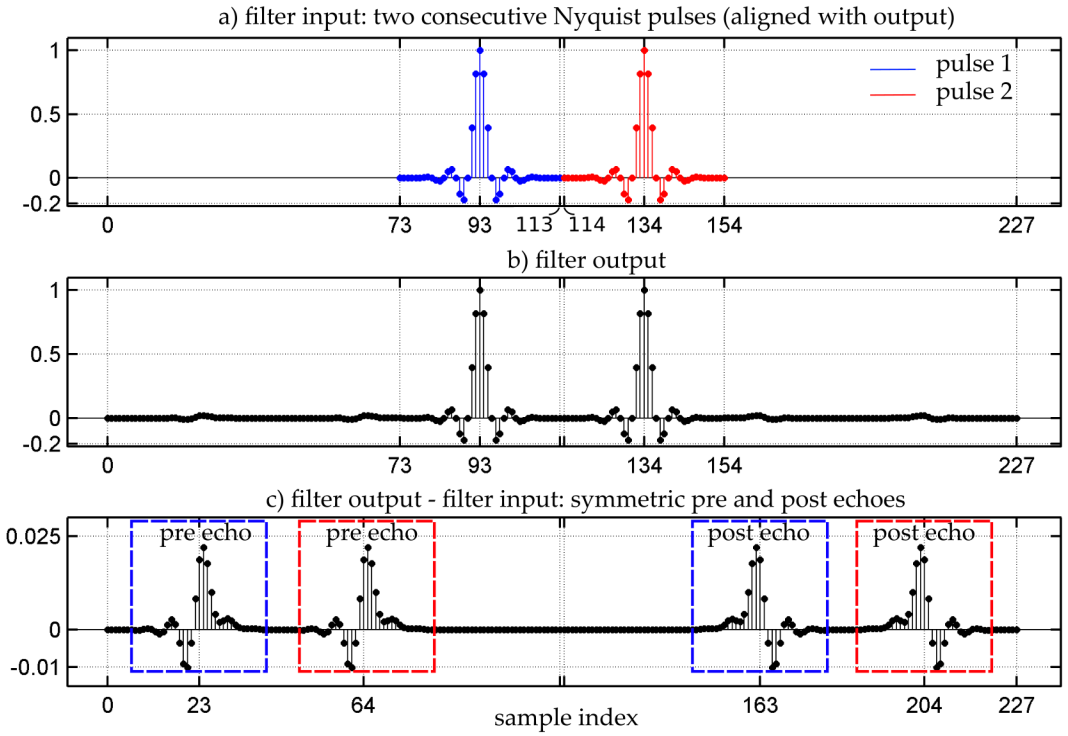


Figure 30 – ISI introduced by pulse shaping of a Nyquist signal. Filter with $n_d = 73$, $\alpha = 70$ and $\sigma = 0.05$. a) Two consecutive Nyquist pulses with roll-off factor = 0.5 and length = 41. The input samples are normalized to its peak value. b) Filter output composed of main and echo components, length = 228 samples. c) Pre and post echoes creating ISI to adjacent symbols.

The sizes of the outlier samples is particularly important because they multiply (attenuate or amplify) the ISI samples introduced by the pulse shaping in a symbol, i.e. since the ISI in the symbol *l* is result of the convolution of the last samples of the previous symbol *l-1* with the filter tail samples, the ISI can be attenuated by small filter tails thus increasing the SIR of the filtered received signal. An illustration of the impulse responses of semi-equiripple, equiripple and windowed truncated *sinc* filters with the same number of coefficients is provided in Fig. 32(a) to observe the difference between their respective tail samples. Filters are designed to meet the SEM specifications in table 4, except the equiripple filter which has constant sidelobe level starting from the stopband frequency edge. It is observed that the outlier samples in the semi-equiripple filter are smaller than in equiripple and since the Kaiser filter exhibits more attenuation decay in frequencies near to the main lobe, as seen in Fig. 32(b), their outlier samples are the smallest of the three filters.

Furthermore, as well as the stopband attenuation rate, the variation rate of the in-band spectral content also is related to the smoothness of the impulse response. For instance, Fig. 33 depicts the influence of in-band ripple $\delta$ on the size of the outlier samples at tails of four semi-equiripple filters with exponential attenuation and the same decay rate. In Fig. 33 is observed that a small $\delta$ leads to smaller outlier samples, thus enabling better rejection of ISI during pulse shaping. This seems contrary to the response result for Kaiser

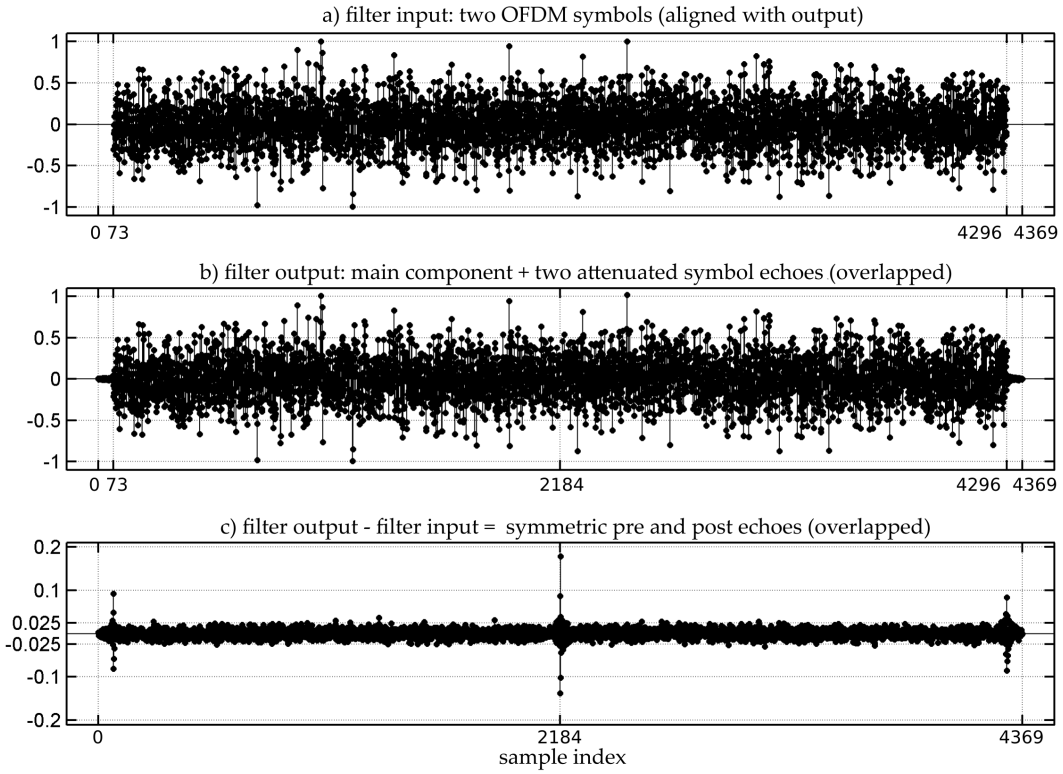


Figure 31 – ISI introduced by pulse shaping of a OFDM signal. a) Two consecutive ISDB-T OFDM symbols in mode 1 with CP 1/32 = 64 samples, total length = 4224 samples. The signal is normalized to its peak value. and only in-phase component is shown. b) Filter output composed of main and echo component with length = 4370 samples. c) Pre and post echoes creating ISI to adjacent symbols.

filter in Fig. 32(b), whose ripples are the longest of those in the other filters shown in that figure. In fact, there is not contradiction because the smoothness of the impulse response is affected not only by spectral containment in passband but also stopband. A filter with faster attenuation has smoother impulse response but in case of windowed truncated *sinc* filters also exhibits larger ripples near pass-band edge because of Gibbs effect which tend to increase the size of the tail samples. So, the fast attenuation rate effects dominate the in-band ripple effects in that example.

### 3.5.3 SIR performance

From sections 2.4 and 3.3, the CP of the symbols must be properly sized to eliminate the ISI caused by both channel delay spread and filter group delay, and thus avoid degradation of the system performance. In section 2.6, simulations for link performance have shown that the effects of self-ISI caused by symbol windowing and the channel impulse response (CIR) can be quantified using the signal to interference power ratio (SIR) metric whose results were consistent with BER results. Considering that the ISI caused by filtering can be assumed by the receiver as channel distortion, the SIR metric is proposed to evaluate

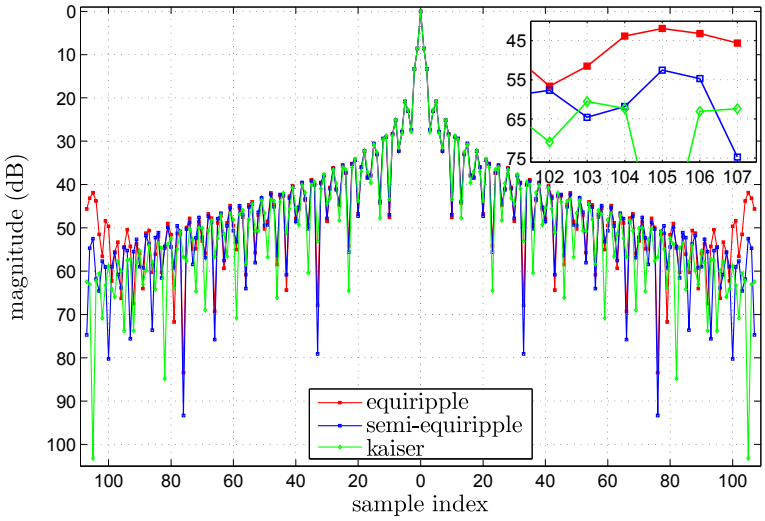


(a) Magnitude impulse response

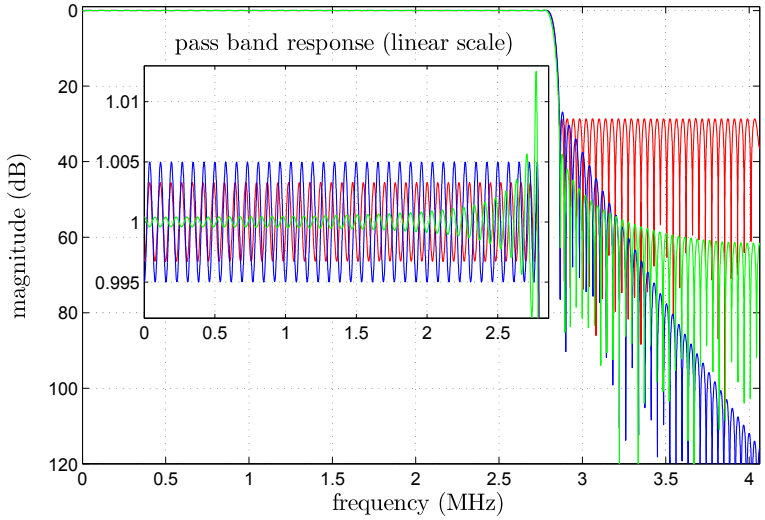


(b) Magnitude frequency response

Figure 32 – Comparison of response of equiripple, semi-equiripple and windowed *sinc* filters. Filter order = 214, semi-equiripple filter with $\delta = 0.5\%$ and exponential decay using $\gamma = 29.8$, Kaiser window factor = 3.1.

the influence of the proposed filters on the waveform. Simulations were performed with semi-equiripple filters of exponential stopband attenuation and the same decay rate under different CP length conditions.

For the particular parameters used in the simulation (Fig. 34), its observed that as longer the CP is specified, the SIR increases (e.g. for the filter 1, the increment of CP from 1/32 to 1/16 improves the SIR in 28 dB) and is also more influenced by the size of pass-band ripples $\delta$ than by the filter order. As can be seen, for CP = 1/16, the SIR is higher for smaller values of $\delta$ despite of more ISI is introduced by the filter group delay ($\frac{order}{2}$). This is a consequence of the tail samples in the impulse response, since in the case of filters with smaller $\delta$, the tails are smaller too which serves to attenuate the ISI. On the other hand, as shorter the CP is, the opposite occurs, the SIR decreases and is more influenced

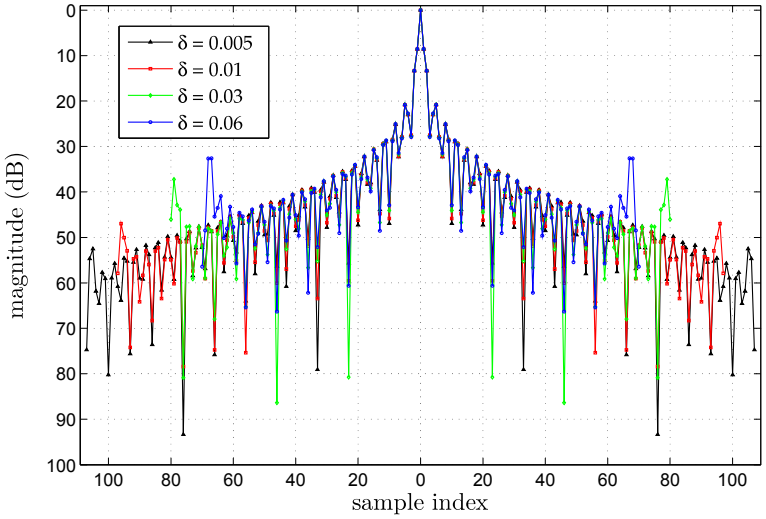


Figure 33 – Influence of passband ripples on the size of tail samples in semi-equiripple filters. Filters with exponential attenuation decay $\gamma = 29.8$.

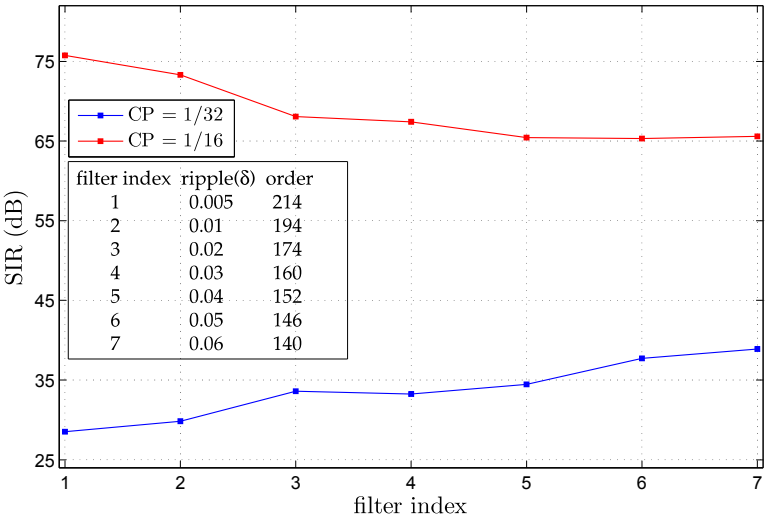


Figure 34 – Effects of CP and filter ripple size and filter group delay in the value of SIR. The SIR of all active subcarriers in each symbol is averaged and then re-averaged over all the symbols. Shaping filters with equal stopband attenuation (exponential, $\gamma = 29.8$) but different ripple sizes. Transmission of 2040 symbols in mode 1.

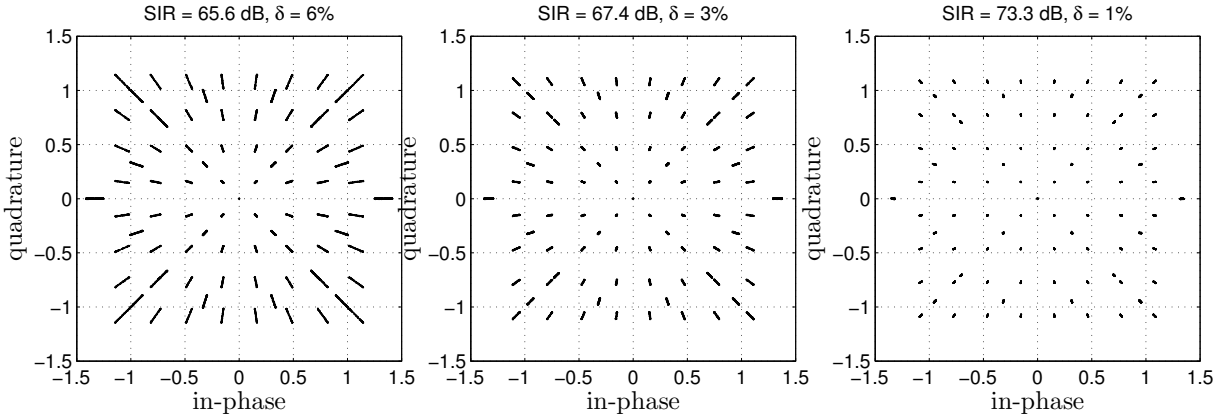


Figure 35 – Received IQ constellations for different values of SIR. Burst sequence of 10 symbols are transmitted in mode 1, with CP = 1/16 and in three layers: layer A (QPSK), layer B (64-QAM), layer C (16-QAM). Pilots AC1/TMCC/SP are BPSK and all the symbols are normalized to power constellation.

by the order than by $\delta$ because of the ISI effect predominates in this case.

A simulation performed with CP=1/16 and Kaiser filter (Fig. 32) results in a SIR 4 dB higher than the semi-equiripple case ($\delta = 0.005$ and same order of Kaiser filter) because of the smaller Kaiser tail samples (see Fig. 32). The SIR results in Fig. 34 suggest that even if higher filter orders are used (e.g. to accomplish tight SEM specifications), a higher number of ISI samples introduced does not necessarily lead to severe performance degradation.

Fig. 35 shows the received constellations for the filters in Fig. 33. It is noticeable the relation between the SIR and the accuracy of the constellation and that under better SIR conditions the distortion of the constellation is less severe. The distortion around ideal constellation points, like noise clouds, is due to the ICI which modifies the magnitude and phase of the symbol subcarriers.

Furthermore, using the same waveform configuration as in Fig. 35, in Fig. 36 is shown the influence of the CP length in the received constellation. Significant constellation distortion is observed in Fig. 36(a) with CP = 1/32 due to ICI. In this case the CP only eliminates 44% of ISI, in contrast to Fig. 36(b) with CP = 1/16 where 88% of ISI is eliminated by the CP.

### 3.5.4 Frequency domain effect of filtering

Since the SIR can be calculated on a per-subcarrier basis, it can also be used to assess the frequency domain distortions (ICI) introduced by the filter. This is equivalent to calculating the error vector magnitude (EVM) statistics, or its equivalent metric modulation error rate (MER), over the transmission bandwidth (EVM/MER spectrum). The EVM/MER is used here because it can be calculated at both transmitter and receiver sides. The EVM

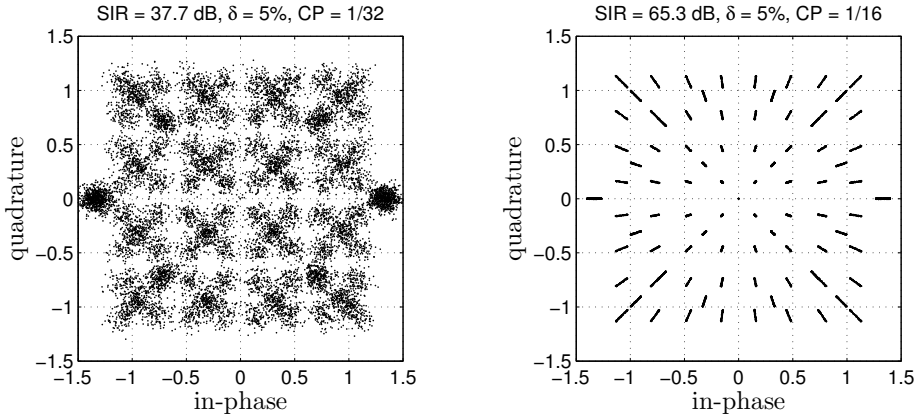


(a) (b)

Figure 36 – Effect of the CP length on received constellation.

is a figure of merit for modulation accuracy and expresses the relative deviation (error vector) between the received symbol and its estimated value (ideal reference). It can be defined as

$$EVM_{rms} = \sqrt{\frac{P_e}{P_r}}, \tag{3.59}$$

where $P_e$ is the RMS power of the error vector and $P_r$ is the RMS power of the ideal reference vector which are defined as

$$P_e = \frac{1}{N_u} \sum_{k=1}^{N_u} \left( \left(S_{ik}^* - \hat{S}_{ik}\right)^2 + \left(S_{qk}^* - \hat{S}_{qk}\right)^2 \right), \text{and} \tag{3.60a}$$

$$P_r = \frac{1}{N_u} \sum_{k=1}^{N_u} \left( {S_{ik}^*}^2 + {S_{qk}^*}^2 \right), \tag{3.60b}$$

where $S_{ik}^*$ and $S_{qk}^*$ are the in-phase component and quadrature component, respectively, of the estimated symbol ($S_k^*$) on the $k$-th subcarrier obtained after symbol demapping. $\hat{S}_{ik}$ and $\hat{S}_{qk}$ are the components of the actual received symbol $\hat{S}_k$ obtained before symbol demapping and after FFT demodulation and amplitude/phase correction. $N_u$ is the number of averaged subcarriers. The performance of a digital radio can be also expressed by the MER as

$$MER = 20 \cdot \log_{10} \left( \frac{1}{EVM_{rms}} \right) \text{dB}. \tag{3.61}$$

The transmitter MER is a metric of the quality of the modulator and $P_e$ and $P_r$ are the calculated over the transmitted symbols. The receiver MER is obtained from the received symbols and therefore it includes the distortions introduced by the channel and the receiver hardware. Simulations of transmitted MER and received MER are performed for the semi-equiripple shaping filters previously analyzed (Fig. 34) and considering only the effects of the filter and there is no other distortion. For the receiver MER, it is considered that the transmitter (TX) and receiver (RX) use the same filter. Thus, the

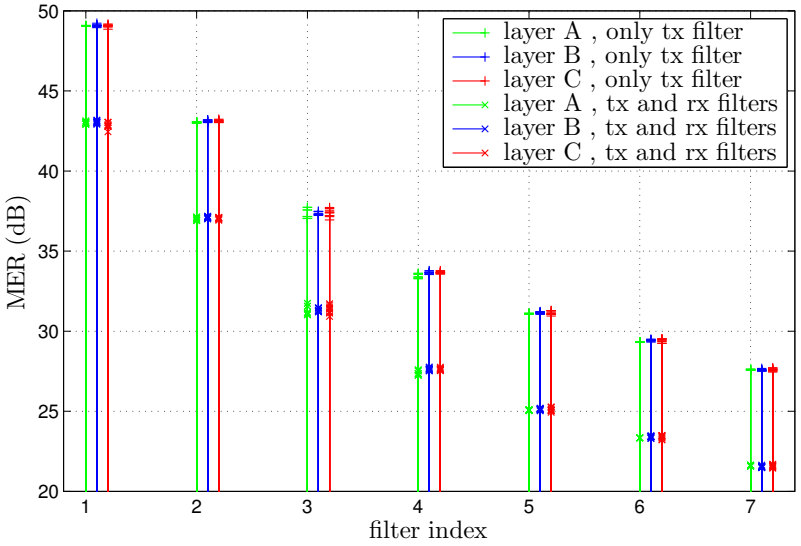


Figure 37 – Simulated MER performance by OFDM symbol time averaged over all layer subcarriers for different shaping filters. The TX MER considers only TX filters whilst RX MER considers both TX and RX filters. Filters 1,2,...,7 with different pass-band ripples but the same attenuation rate $\gamma = 29.8$. Transmission of a burst sequence of 10 symbols in mode 1 with CP = 1/8, layer a (QPSK), layer b (64-QAM) and layec c (16-QAM). Ideal synchronization is assumed

equivalent filter will exhibits approximately twice the size of the pass-band ripple so it is expected that the sizes of the outlier samples will increase, thus amplifying the ISI. The simulated MER for different layers over a sequence of symbols is shown in Fig. 37.

It is observed that the results are consistent with the SIR results in Fig. 34. The MER is more affected by the pass-band ripple $\delta$ than by the filter order when the CP is relatively long and the sensitivity of the modulation order to interference caused by filtering is almost uniform over the three layers. Also, the receiver MER is lower than the transmitter MER because the additional ISI inserted by the receiver filter.

To assess the effect of filtering in the frequency domain, Fig. 38 shows the simulation of MER on a per-subcarrier basis over multiple OFDM symbols. It is noticeable the distortion that occurs at the edges of the band which is due to the sharpness of the transition band. For the waveform and filter used in the simulation, the MER in some subcarriers of layer C are reduced to a value close to 30 dB, the minimum required by the ISDB-T standard [23]. This effect indicates that a proper trade-off among the filter characteristic must be made to meet both in-band and OOB performances.

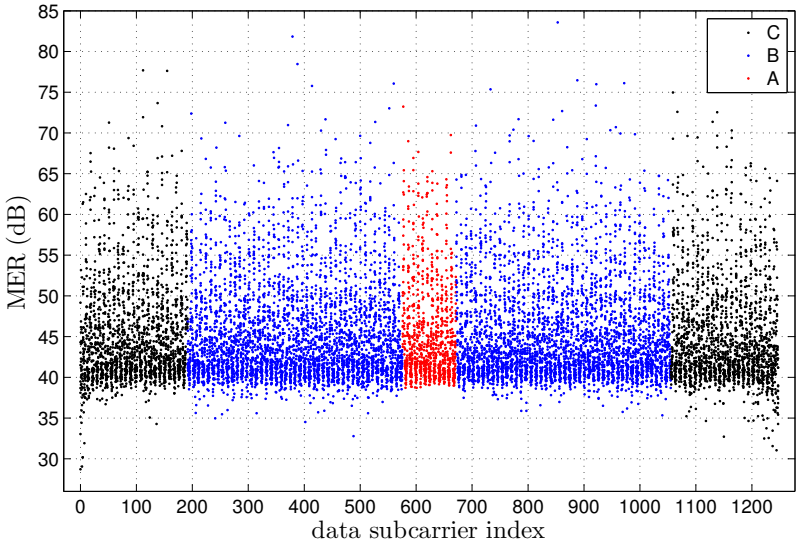


Figure 38 – Simulated receiver MER performance by subcarrier for multiple OFDM symbols. Filter 1 ($\delta = 0.005$) at the transmitter and receiver sides. Transmission of 10 symbols in mode 1 with CP = 1/8. Only MER of data subcarriers in layer a (QPSK), b (64 QAM) and c (64 QAM) are shown. A distortion is observed at the edges of the band.

### 3.5.5 BER performance of subband-based filtering OFDM

#### Description of the waveform considered for analysis (multi service)

In order to analyze the effect of filtering on the reduction of the inter-subband interference in a subband-based filtering transceiver, it is considered a single waveform composed of two parallel streams in adjacent subbands. Each subband occupies a fraction of a 5-MHz bandwidth and has independent parameters such as bandwidth, subband filter, subcarrier spacing, CP length and transmission time interval (TTI). The values of the main parameters are listed in table 5 and other unlisted values are set to follow the LTE standard.

#### BER performance

The simulation has been performed considering that the streams corresponding to independent services (service 1 and 2) are separated in frequency by 60 KHz (the subcarrier spacing of service 2), subcarrier in IFFT index 0 is null and the channel is AWGN. A time delay is inserted between the streams to simulate asynchronous transmission. For a given service, the same filter is used at both transmitter and receiver sides. However, the filters of different services are different according with the bandwidth of each service. The equiripple filters are designed to have a stopband attenuation of -20 dB, 210 taps and transition band of 45 KHz and the semi-equiripple filters have an stopband with exponential decay rate ($\gamma = 4.3$) starting at -20 dB, 236 taps and transition band of 45 KHz. All the filters have a pass-band ripple $\delta$ of 1.25% and their frequency responses are

Table 5 – waveform parameters

| Parameter | subband 1 | subband 2 |
|---|---|---|
| duplex mode | FDD | |
| sampling rate | 7.68 MHz | |
| bandwidth | 750 KHz | 780 KHz |
| FFT size | 512 | 128 |
| subcarrier spacing | 15 KHz | 60 KHz |
| number of subcarriers | 48 | 12 |
| IFFT subcarrier index | [-24,-23,...,24] (except 0) | [8,9,..,19] |
| symbol duration | 66.67 $\mu$s | 16.67 $\mu$s |
| TTI | 1 ms | 0.1 ms |
| symbol per TTI | 14 | 5 |
| CP length | 40 samples (5.2 $\mu$s) for symbol 1 36 samples (4.7 $\mu$s) for symbols 2∼7 | 28 samples (3.7 $\mu$s) for symbol 1 25 samples (3.3 $\mu$s) for symbols 2∼5 |
| modulation | 64 QAM | 64 QAM |

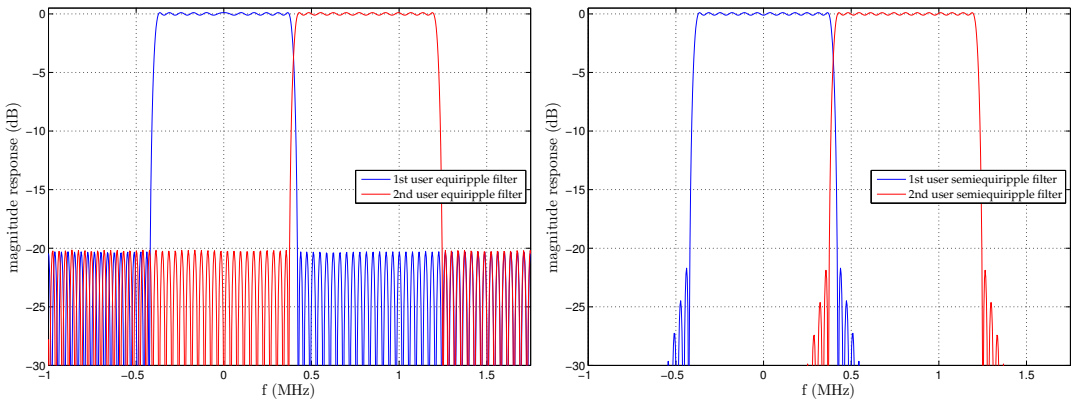


(1) (2)

Figure 39 – Magnitude frequency response of subband filters. Stopband attenuation with a) constant sidelobe level and b) exponentially sloped sidelobes.

presented in Fig.39. Fig. 40 presents the BER results for the service 1 when equiripple and semi-equiripple filters are used in each service bandwidth. There are also included for comparison the cases when no suppression of OOBE is performed (conventional OFDM, worst case) and ACI from service 2 is not present (best case).

The results show that subband filtering improves the receiver BER because it attenuates the ISBI. It is observed a BER improvement for the semi-equiripple filter in relation to the equiripple case despite it is longer and this is due to the ISI is better rejected by smaller impulse response tail samples (Fig. 41). Semi-equiripple filters do not exhibit large impulse response tails which serve to attenuate the ISI. It can be also observed in Fig. 40 an improvement in performance when the CP is extended and shifted to contain

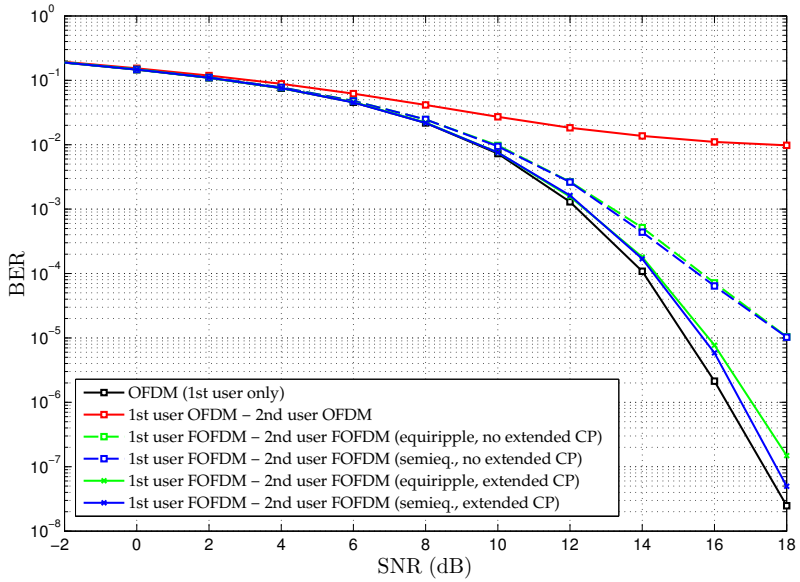


Figure 40 – BER of a subband filtered-OFDM receiver affected by ACI of other active filtered subband. Simulation using 10 frames for service 1 and 200 frames for service 2 per run and 100 runs. Difference of power between service streams = 0 dB, time offset = 150 samples, additional CP = 100.

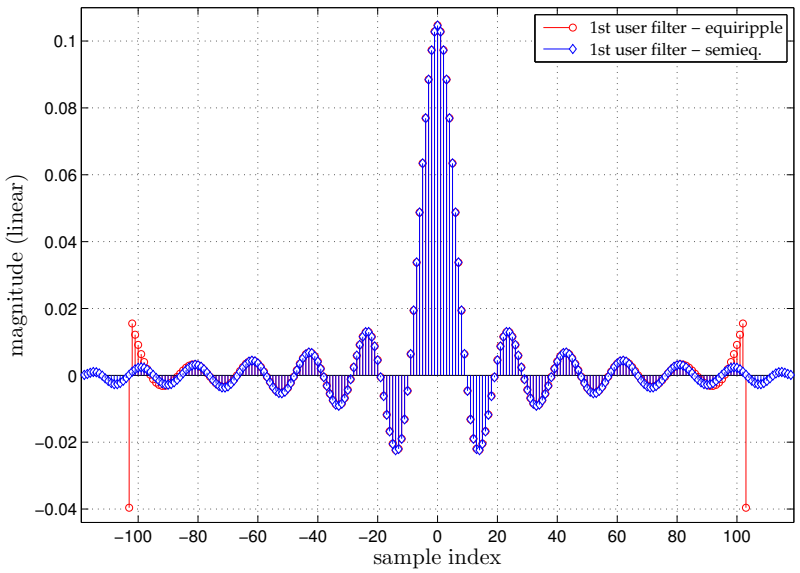


Figure 41 – Comparison of the impulse responses of equiripple and semi-equiripple filters used in the subband-based filtering transceiver.

the filter tails causing ISI back and forth between adjacent OFDM symbols [11].

### 3.5.6 Impact of section scaling and section sequencing on the round-off noise and word-length growth

The objective of this section is to analyze the effects of the section scaling methods on the probability of internal overflows and the section sequencing on the output round-off noise in a fixed-point implementation of the cascade filter structure. Filter scaling reduces the

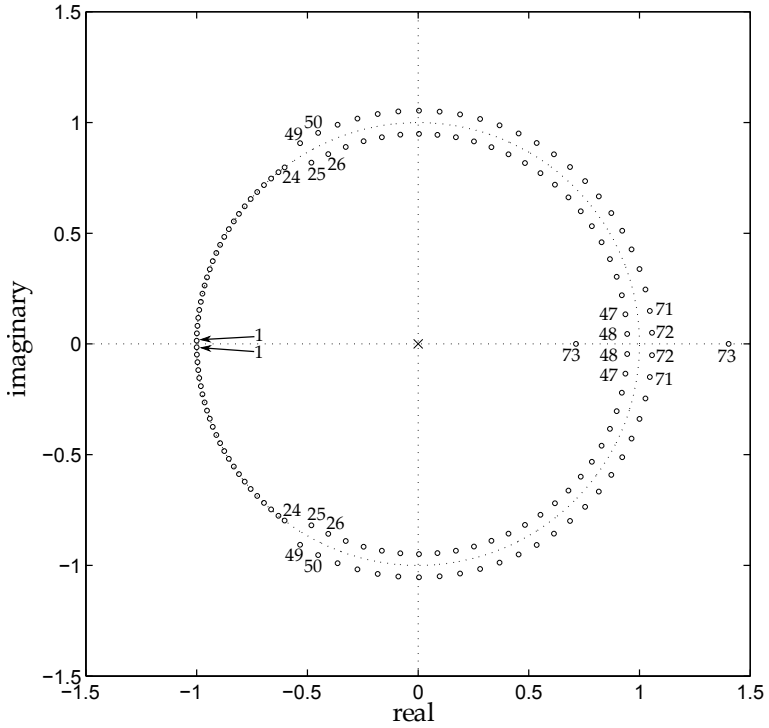


Figure 42 – Pairing of complex conjugated zeros in $2^{nd}-$order sections and initial section positioning. Zeros marked with the same number belongs to the same section. The zeros in the upper half of the unit circle are numbered clockwise and the zeros of the bottom half counter-clock wise.

probability of internal overflows, but it also reduces the maximum amplitude (or maximum average power) at each section output which can limit the use of the entire available data-path dynamic range. Thus, a trade-off between both effects should be performed by scaling the filter properly. Also, the sequence in which the sections are placed influences the output noise power (section 3.4.3). For a cascade filter with $N_s$ sections, the search of a sequence that produces the lowest output noise (optimum sequence) involves the analysis of all possible sequences, i.e. $N_s!$ calculations. Practical approaches suggest that a good section sequence may be one that leads to noise low enough to meet a required SNR.

The filter in Fig. 27(b) is taken as a reference for these analysis. This filter has 146 zeros (see Fig. 42), where 48 of them form 24 pairs of complex conjugated zeros on the unit circle realizing the $1/f^{\gamma}$ attenuation decay rate, 96 zeros are organized in groups of four complex conjugated reciprocal zeros out of the unit circle which realize the pass-band equiripple response, and two zeros are real reciprocal located at $\omega = 0$. Table 6 shows a grouping of them in $2^{nd}-$order factors.

It was used as a base reference and simulated the algorithm for section scaling in [32]. This algorithm scales cascade filters composed of $2^{nd}-$order sections and also calculates the output noise variance for an arbitrary section sequence. Considering the Fig. 18, the filter under analysis has 73 internal points where the signal is constrained to be less than

Table 6 – Coefficients of the $2^{nd}-$order sections $H_k(z)$ of the filter in Fig. 42. $H_k(z) = b_{0k} + b_{1k}z^{-1} + b_{2k}z^{-2}$.

| k | $b_{0k}$ | $b_{1k}$ | $b_{2k}$ | k | $b_{0k}$ | $b_{1k}$ | $b_{2k}$ |
|---|---|---|---|---|---|---|---|
| 1 | 1.0 | 1.999786259333517 | 1.0 | 37 | 1.0 | -0.964781141652287 | 0.900611871892813 |
| 2 | 1.0 | 1.997732824845230 | 1.0 | 38 | 1.0 | -1.104904594916918 | 0.900558076549617 |
| 3 | 1.0 | 1.993241038711731 | 1.0 | 39 | 1.0 | -1.236508431712190 | 0.900464034292094 |
| 4 | 1.0 | 1.986133983203591 | 1.0 | 40 | 1.0 | -1.358584582749976 | 0.900301087707120 |
| 5 | 1.0 | 1.976249309565191 | 1.0 | 41 | 1.0 | -1.470203634293726 | 0.900064145916822 |
| 6 | 1.0 | 1.963506766275278 | 1.0 | 42 | 1.0 | -1.570476385949251 | 0.899739212075105 |
| 7 | 1.0 | 1.947799138625880 | 1.0 | 43 | 1.0 | -1.658537569860689 | 0.899241063066372 |
| 8 | 1.0 | 1.929113415939884 | 1.0 | 44 | 1.0 | -1.733579923499450 | 0.898541193218635 |
| 9 | 1.0 | 1.907349792900964 | 1.0 | 45 | 1.0 | -1.794835034171043 | 0.897576884824526 |
| 10 | 1.0 | 1.882479020864099 | 1.0 | 46 | 1.0 | -1.841498330236457 | 0.896281587731416 |
| 11 | 1.0 | 1.854412697339047 | 1.0 | 47 | 1.0 | -1.872809868941358 | 0.894742426214481 |
| 12 | 1.0 | 1.823127014978403 | 1.0 | 48 | 1.0 | -1.888399718835444 | 0.893529071952462 |
| 13 | 1.0 | 1.788618597876675 | 1.0 | 49 | 1.0 | 1.066737089059890 | 1.107144372640704 |
| 14 | 1.0 | 1.750881261815759 | 1.0 | 50 | 1.0 | 0.902187543578339 | 1.112023630405334 |
| 15 | 1.0 | 1.709853531172283 | 1.0 | 51 | 1.0 | 0.727828022265568 | 1.112269272811463 |
| 16 | 1.0 | 1.665457704264032 | 1.0 | 52 | 1.0 | 0.547965431433156 | 1.111914131300770 |
| 17 | 1.0 | 1.617703476160164 | 1.0 | 53 | 1.0 | 0.364398717850532 | 1.111491742561203 |
| 18 | 1.0 | 1.566591689942999 | 1.0 | 54 | 1.0 | 0.178607818896288 | 1.111175459759429 |
| 19 | 1.0 | 1.512054881898694 | 1.0 | 55 | 1.0 | -0.008050542047539 | 1.110893709985645 |
| 20 | 1.0 | 1.454001163906983 | 1.0 | 56 | 1.0 | -0.194224020367507 | 1.110692562129048 |
| 21 | 1.0 | 1.392619003581766 | 1.0 | 57 | 1.0 | -0.378579344995924 | 1.110538669605909 |
| 22 | 1.0 | 1.328106283500480 | 1.0 | 58 | 1.0 | -0.559757010213032 | 1.110426707129799 |
| 23 | 1.0 | 1.262313084569545 | 1.0 | 59 | 1.0 | -0.736447761049778 | 1.110351488067225 |
| 24 | 1.0 | 1.205662301423766 | 1.0 | 60 | 1.0 | -0.907366109027030 | 1.110337273800086 |
| 25 | 1.0 | 0.963503148659435 | 0.903224570084626 | 61 | 1.0 | -1.071250748254758 | 1.110356226926380 |
| 26 | 1.0 | 0.811302492960063 | 0.899261465905637 | 62 | 1.0 | -1.226910982965397 | 1.110422554680080 |
| 27 | 1.0 | 0.654363147536968 | 0.899062865840316 | 63 | 1.0 | -1.373190249274407 | 1.110538524491060 |
| 28 | 1.0 | 0.492812723579758 | 0.899350023396283 | 64 | 1.0 | -1.509033590318118 | 1.110739522204506 |
| 29 | 1.0 | 0.327846536233238 | 0.899691794106997 | 65 | 1.0 | -1.633443172870915 | 1.111031924265104 |
| 30 | 1.0 | 0.160737728076676 | 0.899947880613299 | 66 | 1.0 | -1.745479539929352 | 1.111433164831910 |
| 31 | 1.0 | -0.007246905779708 | 0.900176129373284 | 67 | 1.0 | -1.844374815586333 | 1.112048861058519 |
| 32 | 1.0 | -0.174867489879651 | 0.900339152432187 | 68 | 1.0 | -1.929327154484312 | 1.112915031104951 |
| 33 | 1.0 | -0.340897039749431 | 0.900463916627834 | 69 | 1.0 | -1.999644893397554 | 1.114110687237119 |
| 34 | 1.0 | -0.504091811390125 | 0.900554708905352 | 70 | 1.0 | -2.054597969481312 | 1.115720788743527 |
| 35 | 1.0 | -0.663256427324391 | 0.900615715606153 | 71 | 1.0 | -2.093127378417639 | 1.117640083561082 |
| 36 | 1.0 | -0.817198639041996 | 0.900627245068998 | 72 | 1.0 | -2.113417210599649 | 1.119157765974988 |
| | | | | 73 | 1.0 | -2.115439885893518 | 1.0 |

one. The signal attenuation by scaling at those internal points is shown in Fig. 43.

Since the test input signal is energy scaled, $L_2-$norm scaling is adequate to ensure that overflows do not occur. Although sum scaling and $L_\infty-$norm scaling prevent overflows as well, they limit the internal signals more than $L_2$-norm scaling as observed in Fig. 43. Then, for the case of sum scaling, internal signals are the most attenuated because this scaling method is the most conservative to limit the use of available dynamic range.

The relation given in Eq. (3.33) shows that the contribution of the noise of a section $k$ to the total output noise is proportional to $\sum_n {g_k}^2[n]$, for $k = 1, 2, ..., N_s$ where $g_k[n]$ is the equivalent filter from section $(k+1)$ to the filter output. Thus, a method for sequencing can be devised as one that allows to find the sections of equivalent filters $g_k[n]$ that minimize the section noises individually.

In order to observe the dependence of the overall output noise to the section sequence, the noise distribution is obtained by simulation using a number of different random sequences. The noise distribution histogram for the filter after the sum-scaling is presented in Fig. 44. It is observed that the histogram is concentrated around the sequences yielding output

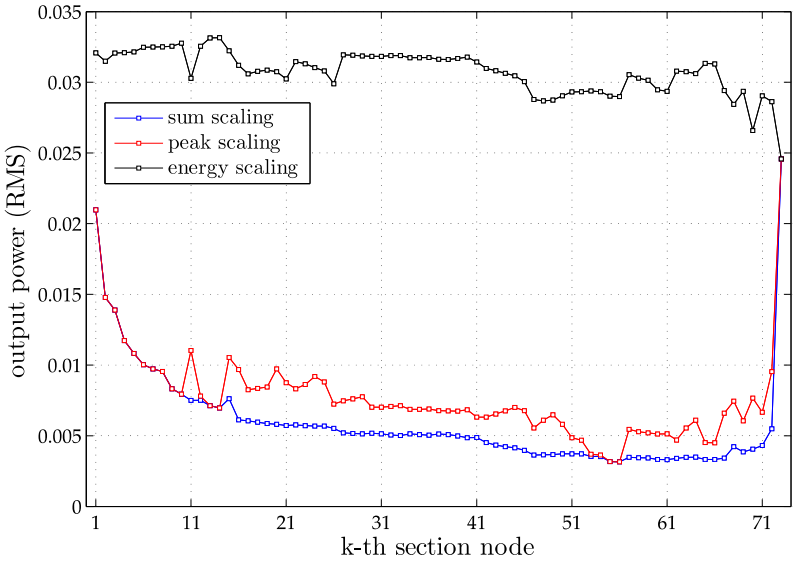


Figure 43 – Simulated RMS values of signals at the section outputs for different scaling methods. Cascade filter with 73 sections. The input signal is white Gaussian noise with zero mean and is scaled such that its total energy is 1. The section sequence of the sections is generated randomly (non-optimal sequencing) and both the sequence and input signal are the same for the three scaling methods.

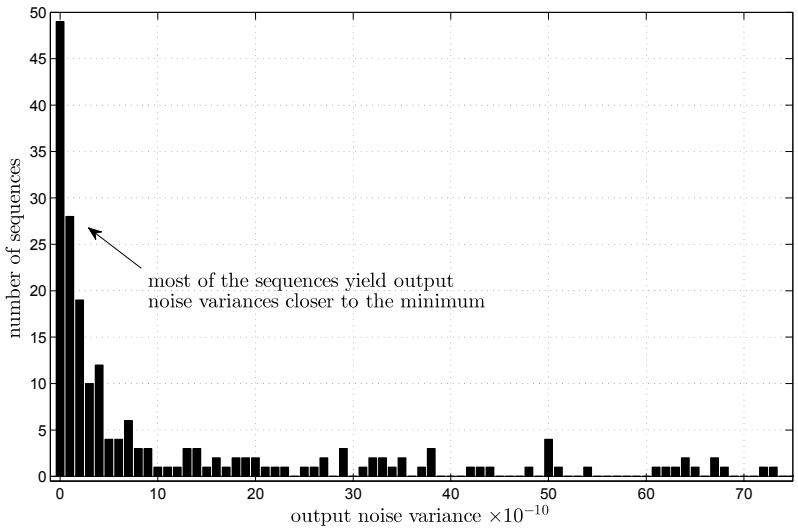


Figure 44 – Noise distribution histogram of the sum-scaled cascade filter over different section sequencing. The histogram is built with the 200 lowest values of noise, which correspond to 200 sequences, from the analysis of a total of 1000 random sequences. The histogram looks concentrated around the lowest noise levels.

noise variances closer to the minimum. The values of noise of the total number of sequences are in the range of $10^6$ to $10^{35}$ and it is expected that low noise sequences will be found by using the above idea.

Since Fig. 44 shows that a random sequence has relatively low noise, it could be a good initial sequence to be used by the sequencing method. So, in Table 7 are presented the output noise levels for the cases in which the section sequencing method is or is not used.

Table 7 – Values of round-off noise of the filter in Fig. 42 for different section sequences. Values are in units of $\Delta^2$, where $\Delta$ is the quantization step size. Section coefficients and initial positioning $sequence(k)$ of sections in the filter are given in table 6, $k = 1, 2, 3, ..., N_s$.

| | no sequencing method is used | | sequencing method is used | |
|---|---|---|---|---|
| | $sequence$(k) = k | $sequence$ = random | $sequence$(k) = k | $sequence$ = random |
| | filter composed of $2^{nd}-$order sections | | | |
| sum scaling | $4.349 \times 10^{32}$ | $4.685 \times 10^{17}$ | 1374.5 | 241.4 |
| $L_2-$norm (energy) scaling | $5.341 \times 10^{32}$ | $1.354 \times 10^{17}$ | 324.0 | 241.2 |
| $L_\infty-$norm (peak) scaling | $1.160 \times 10^{65}$ | $1.874 \times 10^{18}$ | 604.9 | 594.0 |
| | filter composed of $2^{nd}$ and $4^{th}-$order sections | | | |
| sum scaling | $2.808 \times 10^{31}$ | $20.236 \times 10^{20}$ | $14.5 \times 10^4$ | $8.382 \times 10^4$ |
| $L_2-$norm (energy) scaling | $2.763 \times 10^{31}$ | $5.136 \times 10^{20}$ | $25.832 \times 10^4$ | $7.424 \times 10^4$ |
| $L_\infty-$norm (peak) scaling | $2.012 \times 10^{68}$ | $101.132 \times 10^{20}$ | $183.404 \times 10^4$ | $183.404 \times 10^4$ |

The section sequence is initialized in two ways: as the same sequence of Table 6 or as a random sequence obtained from a random permutation of integer numbers from 1 to $N_s$. The filter decomposition in $2^{nd}-$order sections (stopband zeros) or $4^{th}-$order sections (passband zeros) are simulated. Moreover, for the sum and $L_2-$norm scaling, the values of $\sum_n |f_k[n]|$ and $\sum_n {g_k}^2[n]$ were calculated in time domain using convolution whereas for the $L_\infty-$norm scaling, the values of $\max_{-\pi \leqslant \omega \leqslant \pi} |F_k(e^{j\omega})|$ were calculated in frequency domain expressing $F_k(e^{j\omega})$ as a product of section frequency responses, i.e. $F_k(e^{j\omega}) = \prod_{i=1}^{k} H_i(e^{j\omega})$, as is given by Eq. (3.38). It is observed that the noise levels are lower when the sections are properly sequenced using random initial sequences. For an implementation in a programmable device with fixed hardware DSP blocks, the choice of a certain low-noise sequence can be done based on the required SNR. The searching of low-noise sequences with high levels of coefficient quantization can be of interest for efficient digital designs.

## 3.6 Summary

In this chapter, the design and analysis of semi-equiripple filters for spectral containment in subband-based filtering waveforms were presented.

The filter design uses the Parks-McClellan method with a configurable weighting function to obtain arbitrary stopband decay rates, as for instance, linearly and exponentially decaying stopbands.

The effects of the passband ripple and impulse response characteristics on the integrity of the signal were analyzed mathematically and by simulation. The distortion due to the filter passband ripples was modeled as symbol echoes, responsible for back and forth ISI. It is found that impulse responses longer than the CP size can be used for low OOBE with slight BER distortion.

It was observed that the stopband attenuation rate depends on the quantity of continuous derivatives of the impulse response. Equiripple filters have outlier samples in the tails of

the impulse response which can increase the ISI. On the other hand, semi-equiripple filters have faster attenuation, therefore they have smoother impulse responses and thus smaller outlier samples which is useful for ISI rejection. It was also observed that as smaller the passband ripples, smaller the outlier samples.

Since the filter frequency response can be tailored to meet tight spectrum masks, different services can be accommodated within a single waveform without significant wastage of spectrum for guard bands. BER simulations for a scenario with asynchronous and non-orthogonal transmission showed that the ISBI can be contained by the subband filters.

Some filter structures and scaling methods to reduce fixed-point effects that result from implementing the filter in hardware were presented. Numerical simulations showed that section scaling reduces the round-off noise and the occurrence of internal overflows.

# Conclusions

In this work pulse shaping methods have been presented for orthogonal frequency division multiplexing (OFDM). Per-subcarrier and per-subband filtering have been studied as a possibility for improving the spectral containment of OFDM waveforms and therefore allow OFDM to be used for in-band multiplexing of services and users of different sets of parameters, as well as in asynchronous fragmented spectrum scenarios.

Details can be summarized as follows. In Chapter 2, the characteristics of cyclic prefixed OFDM (CP-OFDM) in both time and frequency domains have been discussed as well as the spectral leakage due to the function used to filter each subcarrier. With the consideration of using the same function for all subcarriers, filtering has been performed as an element-wise multiplication between the samples of the OFDM waveform and a chosen window. The window is used to smooth symbol transitions, thus reducing the *sinc* spectral sidelobes. The power spectral density of a 5-MHz LTE transmit windowed waveform has been assessed numerically and with a window roll-off factor of 0.2, a reduction of -20 dB is achieved at the subcarriers out of the 4.5-MHz active bandwidth.

In case of extension of symbol duration (prefix and postfix samples) for longer roll-off regions, the windowed symbols are allowed to overlap in order to reduce the loss in throughput. However if the remaining non-windowed CP is not able to absorb the time dispersion due to multipath propagation, the symbol overlapping causes self intersymbol interference (ISI). This effect has been evaluated in the frequency domain using the signal-to-interference power ratio (SIR). Simulations show that although longer values of roll-off reduce more the out-of-band emission (OOBE), the SIR is significantly degraded, thus the bit error rate (BER) at the receiver.

The improvement in performance by windowing the symbols has been observed in the receiver for a fragmented spectrum being accessed by a primary user (PU) and a secondary user (SU) misaligned in time and frequency, i.e. a non-orthogonal and asynchronous scenario. The spectral sidelobes are reduced, thus the interference from adjacent subbands. Simulations show that by windowing received symbols the BER improves to almost the same performance as in the case when there is no interference. However, as the roll-off region increases, more self-ISI is introduced within the useful symbol period, therefore there is a tradeoff between adjacent channel interference (ACI) and ISI to preserve adequate in-band performance.

In Chapter 3, the design of semi-equiripple filters with custom stopband decay rate has been discussed. The frequency response of a FIR filter designed with the Parks-McClellan method can be tailored to meet an arbitrary spectral mask specification (SEM) by config-

uring the frequency-domain weighting function. The contribution to ISI has been analyzed in terms of the pre- and post-echoes of the signal due to the filter passband ripples. The amplitude of the echoes is proportional to the amplitude of the ripples, and the dispersion of the echoes, to the frequency of the ripples and the length of the filter.

Also, the effect of the filter impulse response on the ISI has been analyzed. Equiripple filters exhibit larger outlier samples in the tails of the impulse response which is due to the constant level spectral sidelobes. However, semi-equiripple filters with faster stopband attenuation (e.g. with exponential decay rate) have smaller outlier samples which is useful to reject ISI and thus improving the accuracy of the received symbol constellation. Simulations show that impulse responses longer than the CP size can be used for low OOBE without causing penalty in modulation error rate (MER) performance.

The performance of subband filtering has been analyzed in a subband-based filtering waveform in which each subband has been configured with a set of transmission parameters for an arbitrary service in a non-orthogonal and asynchronous scenario. Simulations show that by filtering each subband independently, the BER is improved because the inter-subband interference (ISBI) and the ISI are reduced. Also, if the filter order is extended beyond the size of the CP for better spectral containment, more ISI samples are inserted into the useful symbol period but, in spite of that, the BER decreases. Thus, the improvement in performance by subband filtering dominates the penalty due to the ISI and several services can be multiplexed in a single waveform without significant wastage of spectrum in guard bands.

# References


[1] K. Panta and J. Armstrong. Spectral analysis of ofdm signals and its improvement by polynomial cancellation coding. *IEEE Transactions on Consumer Electronics*, 49(4):939–943, Nov 2003.

[2] S. Brandes, I. Cosovic, and M. Schnell. Sidelobe suppression in ofdm systems by insertion of cancellation carriers. In *VTC-2005-Fall. 2005 IEEE 62nd Vehicular Technology Conference, 2005.*, volume 1, pages 152–156, Sept 2005.

[3] I. Cosovic, S. Brandes, and M. Schnell. Subcarrier weighting: a method for sidelobe suppression in ofdm systems. *IEEE Communications Letters*, 10(6):444–446, June 2006.

[4] T. Weiss, J. Hillenbrand, A. Krohn, and F. K. Jondral. Mutual interference in ofdm-based spectrum pooling systems. In *Vehicular Technology Conference, 2004. VTC 2004-Spring. 2004 IEEE 59th*, volume 4, pages 1873–1877 Vol.4, May 2004.

[5] P. Sutton, B. Ozgul, I. Macaluso, and L. Doyle. Ofdm pulse-shaped waveforms for dynamic spectrum access networks. In *New Frontiers in Dynamic Spectrum, 2010 IEEE Symposium on*, pages 1–2, April 2010.

[6] E. Bala, J. Li, and R. Yang. Shaping spectral leakage: A novel low-complexity transceiver architecture for cognitive radio. *IEEE Vehicular Technology Magazine*, 8(3):38–46, Sept 2013.

[7] G. Fettweis, M. Krondorf, and S. Bittner. Gfdm - generalized frequency division multiplexing. In *Vehicular Technology Conference, 2009. VTC Spring 2009. IEEE 69th*, pages 1–4, April 2009.

[8] B. Farhang-Boroujeny. Ofdm versus filter bank multicarrier. *IEEE Signal Processing Magazine*, 28(3):92–112, May 2011.

[9] M. Bellanger. Physical layer for future broadband radio systems. In *2010 IEEE Radio and Wireless Symposium (RWS)*, pages 436–439, Jan 2010.

[10] V. Vakilian, T. Wild, F. Schaich, S. ten Brink, and J. F. Frigon. Universal-filtered multi-carrier technique for wireless systems beyond lte. In *2013 IEEE Globecom Workshops (GC Wkshps)*, pages 223–228, Dec 2013.

[11] J. Abdoli, M. Jia, and J. Ma. Filtered ofdm: A new waveform for future wireless systems. In *2015 IEEE 16th International Workshop on Signal Processing Advances in Wireless Communications (SPAWC)*, pages 66–70, June 2015.

[12] X. Zhang, M. Jia, L. Chen, J. Ma, and J. Qiu. Filtered-ofdm - enabler for flexible waveform in the 5th generation cellular networks. In *2015 IEEE Global Communications Conference (GLOBECOM)*, pages 1–6, Dec 2015.

[13] P. Banelli, S. Buzzi, G. Colavolpe, A. Modenini, F. Rusek, and A. Ugolini. Modulation formats and waveforms for 5g networks: Who will be the heir of ofdm?: An overview of alternative modulation schemes for improved spectral efficiency. *IEEE Signal Processing Magazine*, 31(6):80–93, Nov 2014.

[14] F. Schaich and T. Wild. Waveform contenders for 5g - ofdm vs. fbmc vs. ufmc. In *Communications, Control and Signal Processing (ISCCSP), 2014 6th International Symposium on*, pages 457–460, May 2014.

[15] F. Schaich, T. Wild, and Y. Chen. Waveform contenders for 5g - suitability for short packet and low latency transmissions. In *2014 IEEE 79th Vehicular Technology Conference (VTC Spring)*, pages 1–5, May 2014.

[16] J. Luque and L. Meloni. Ofdm pulse shaping for use in 5g systems. *XXIII Brazilian Symposium of Telecommunications*, 2015.

[17] S. Talwar, D. Choudhury, K. Dimou, E. Aryafar, B. Bangerter, and K. Stewart. Enabling technologies and architectures for 5g wireless. In *2014 IEEE MTT-S International Microwave Symposium (IMS2014)*, pages 1–4, June 2014.

[18] G. Wunder, P. Jung, M. Kasparick, T. Wild, F. Schaich, Y. Chen, S. T. Brink, I. Gaspar, N. Michailow, A. Festag, L. Mendes, N. Cassiau, D. Ktenas, M. Dryjanski, S. Pietrzyk, B. Eged, P. Vago, and F. Wiedmann. 5gnow: non-orthogonal, asynchronous waveforms for future mobile applications. *IEEE Communications Magazine*, 52(2):97–105, February 2014.

[19] N. C. Beaulieu and P. Tan. On the effects of receiver windowing on ofdm performance in the presence of carrier frequency offset. *IEEE Transactions on Wireless Communications*, 6(1):202–209, Jan 2007.

[20] A. E. Loulou, S. Afrasiabi Gorgani, and M. Renfors. Enhanced ofdm techniques for fragmented spectrum use. In *Future Network and Mobile Summit (FutureNetworkSummit), 2013*, pages 1–10, July 2013.

[21] 3GPP-LTE. 3GPP TS 36.104 V14.0.0, Evolved Universal Terrestrial Radio Access (E-UTRA); Base Station (BS) radio transmission and reception, 2016.

[22] A.V. Oppenheim and R.W. Schafer. *Discrete-Time Signal Processing*. Pearson Education, 2011.

[23] ABNT-ISDBT. Digital terrestrial television – Transmission system; ABNT NBR 15601, 2007.

[24] H. Tarn, K. Neilson, R. Uribe, and D. Hawke. *Designing Efficient Wireless Digital Up and Down Converters Leveraging CORE Generator and System Generator, XAPP1018 (v1.0).* Xilinx Application Note, 2007.

[25] S. Creaney and I. Kostarnov. *Designing Efficient Digital Up and Down Converters for Narrowband Systems, XAPP1113 (v1.0).* Xilinx Application Note, 2008.

[26] 3GPP-UMTS. 3GPP TS 25.104 v6.13.0, Base Station Radio Transmission and Reception (FDD), 2012.

[27] S. R. Powell, G. Temes, and P. M. Chau. A ripple reduction technique for digital filters. In *Circuits and Systems, 1991., IEEE International Sympoisum on*, pages 268–271 vol.1, Jun 1991.

[28] D. S. K. Chan and L. R. Rabiner. Theory of roundoff noise in cascade realizations of finite impulse response digital filters. *The Bell System Technical Journal*, 52(3):329–345, March 1973.

[29] L. Jackson. Roundoff-noise analysis for fixed-point digital filters realized in cascade or parallel form. *IEEE Transactions on Audio and Electroacoustics*, 18(2):107–122, Jun 1970.

[30] Xilinx. *Xilinx User Guide, UltraScale Architecture DSP Slice UG579 (v1.3).* 2015.

[31] Lloyd N. Trefethen. *Spectral Methods in Matlab.* SIAM: Society for Industrial and Applied Mathematics, 2001.

[32] D. S. K. Chan and L. R. Rabiner. An algorithm for minimizing roundoff noise in cascade realizations of finite impulse response digital filters. *The Bell System Technical Journal*, 52(3):347–385, March 1973.